Experimental Study of Particle-Induced Turbulence Modification in the Presence of a Rough Wall

by

Godwin Fabiola Kwaku Tay

A Thesis submitted to the Faculty of Graduate Studies of
The University of Manitoba
in Partial Fulfillment of the Requirements for the Degree of

DOCTOR OF PHILOSOPHY

Department of Mechanical Engineering
University of Manitoba
Winnipeg

ABSTRACT

This thesis reports an experimental investigation of low Reynolds number particle-laden turbulent flows in a horizontal plane channel. Experiments were conducted over a smooth wall and over two rough surfaces made from sand grain and gravel of relative roughness $k/h \approx 0.08$ and 0.25, respectively, where k is the roughness height and h is the channel half-height. The flow was loaded with small solid particles with diameters less than 1/10 of the length scale of the energy-containing eddies, and whose concentrations decreased with time due to sedimentation. A novel particle image velocimetry (PIV) method that employed colour filtering for phase discrimination was used to measure the velocities of the fluid and solid particles.

Over the smooth wall, the particles mean velocity, turbulence intensities and Reynolds shear stress matched those of the unladen flow very well. There were substantial differences between particle and fluid profiles over the rough wall, which include more rapid reduction in the particle mean velocity and significantly larger turbulence intensities and Reynolds shear stress compared to the unladen flow values.

Stratification of the particle concentration led to attenuation of the fluid wall-normal turbulence intensity. This effect was nullified by the roughness perturbation leading to collapse of the wall-normal turbulence intensities over the rough wall. The streamwise turbulence intensity also collapsed over the rough wall but it was found that particles augmented the fluid Reynolds shear stress due to enhanced correlation between the rough wall streamwise and wall-normal velocity fluctuations. A quadrant decomposition of the fluid Reynolds shear stress also revealed corresponding

enhancements in ejections and sweeps, the dominant contributors to the Reynolds shear stress, over the rough wall.

Based on two-point correlations between the velocity fluctuations and between the velocity fluctuations and swirling strength, it was concluded that both wall roughness and particles modified the turbulence structure by increasing the size of the larger-scale structures. The idea of eddies growing from the wall, thereby enhancing communication between the inner layer and outer parts of the flow, has implications for wall-layer models that assume that the outer layer is detached from the turbulence in the inner region.

ACKNOWLEDGEMENTS

I should like to sincerely thank all those individuals who contributed in diverse ways to make this thesis a reality. Foremost, I gratefully acknowledge the help and tutelage provided by my thesis advisors, Professor David C.S. Kuhn and Professor Mark F. Tachie, over the course of not only this project, but throughout the years that I had worked with them. Their kindness and magnanimity, particularly in those times that a few tragedies of circumstance conspired to forestall the early completion of this project, will always be appreciated. It is also true that no part of the work reported herein could have been possible without the able craftsmanship and ingenuity of Mr. Paul Krueger, who assisted both in the fabrication of the camera-laser traverse system and maintenance work on the tunnel facility. To him, I owe a debt of gratitude.

My gratitude also goes to the other members of my Ph.D. committee, Professor Shawn Clark and Professor Bing-Chen Wang for their patience and useful suggestions during this investigation. Their insightful comments were a considerable source of help in shedding light on many aspects of this work.

I must express my indebtedness to my friends and colleagues, Dr. Richard Buckson, Mr. Kwadjo Owusu-Poku, and Mr. Lincoln Baffour, whose moral support and presence through it all will be ever cherished. To Dr. Jonathan Tsikata, I owe many thanks for those e-mail correspondences always asking about my progress on the thesis. Your words have served as a constant reminder to accomplishing this goal.

Dedicated to she, who is not of this world,

for her inspiration. To you be the glory.

TABLE OF CONTENTS

LIST OF TABLES

LIST OF FIGURES

NOMENCLATURE

Roman Symbols

a	proper orthogonal decomposition temporal coefficient
a_1	Townsend's structure parameter
AR	channel aspect ratio
B	additive constant in the logarithmic law
C	particle concentration (kg/m^3)
c	fluctuating component of particle concentration (kg/m^3)
C_b	bulk or depth averaged particle concentration (kg/m^3)
C_D	drag coefficient
C_f	skin friction coefficient
d_{image}	particle image diameter (μm)
d_p	particle diameter (μm)
d_{pitch}	CCD pixel pitch diameter (μm)
F	force acting on a particle per unit volume (N)
F_u	flatness factor of the streamwise fluctuating velocity
F_v	flatness factor of the wall-normal fluctuating velocity
$f\#$	f-number of the CCD camera lens
Ga	particle Galileo number
g	acceleration due to gravity (m/s^2)
H	hyperbolic hole size
h	channel half-height (mm)

h^* wall-normal location where the Reynolds shear stress changes sign from positive to negative (mm)

I particle image intensity

k roughness height (mm)

k_s equivalent sand grain roughness height (mm)

L_e characteristic length of the large-scale fluid eddies (mm)

Lx_{uu} streamwise extent of the streamwise fluctuating velocity auto-correlation contour

Ly_{uu} wall-normal extent of the streamwise fluctuating velocity auto-correlation contour

Lx_{vv} streamwise extent of the wall-normal fluctuating velocity auto-correlation contour

Ly_{vv} wall-normal extent of the wall-normal fluctuating velocity auto-correlation contour

Q contribution to the Reynolds shear stress from a given quadrant (m^2/s^2)

q^2 turbulent kinetic energy (m^2/s^2)

Re_h Reynolds number based on maximum velocity, U_{max} and channel half-height, h

Re_p particle Reynolds number

R_{uu} two-point correlation function of the streamwise fluctuating velocity

R_{vv} two-point correlation function of the wall-normal fluctuating velocity

$R_{\lambda u}$ two-point correlation function of the swirling strength and streamwise fluctuating velocity

$R_{\lambda v}$ two-point correlation function of the swirling strength and wall-normal fluctuating velocity

Re_τ Reynolds number based on the friction velocity U_τ and channel half-height, h

St particle Stokes number

S_u skewness factor of the streamwise fluctuating velocity

S_v skewness factor of the wall-normal fluctuating velocity

T averaging period (s)

U instantaneous streamwise velocity (m/s)

$\overline{U}$ ensemble averaged streamwise mean velocity (m/s)

$\langle U \rangle$ volume fraction weighted streamwise mean velocity (m/s)

U_τ friction velocity (m/s)

$\left(\overline{u'^2}\right)^{0.5}$ streamwise turbulence intensity (m/s) based on Reynolds averaging

$\left(\overline{u''^2}\right)^{0.5}$ streamwise turbulence intensity (m/s) based on volume fraction weighted averaging

$-\overline{u'v'}$ ensemble averaged Reynolds shear stress (m^2/s^2) based on Reynolds averaging

$-\overline{u''v''}$ ensemble averaged Reynolds shear stress (m^2/s^2) based on volume fraction weighted averaging

$\left(\overline{v'^2}\right)^{0.5}$ streamwise turbulence intensity (m/s) based on Reynolds averaging

$\left(\overline{v''^2}\right)^{0.5}$ streamwise turbulence intensity (m/s) based on volume fraction weighted averaging

V instantaneous wall-normal velocity (m/s)

V_s settling velocity (m/s)

x, y streamwise and wall-normal coordinates (mm)

y_o the shift in origin of the streamwise mean velocity due to wall roughness (mm)

Greek Symbols

ε dissipation of turbulent kinetic energy (m^2/s^3)

ϕ_v particle volume fraction. Also used without the subscript *v* to denote the scaling approximation or father wavelet of an orthogonal wavelet function

ϕ_m particle mass loading fraction

ψ mother wavelet function

κ von Kármán constant

ν kinematic viscosity (m^2/s)

ρ density (kg/m^3)

ρ_{-uv} Reynolds shear stress correlation coefficient

ΔB roughness shift

η fluid Kolmogorov length scale (m)

λ_{ci} unsigned swirling strength (s^{-1})

Λ_{ci} signed swirling strength (s^{-1})

λ_T Taylor microscale (m)

τ_f fluid characteristic time scale (s)

τ_p particle relaxation time (s)

τ_w wall shear stress (N/m^2)

ω vorticity (s^{-1})

Mathematical Symbols

$\langle \cdot \rangle$ volume fraction-weighted averaged quantity

$\{\cdot\}_v$ volume-averaged quantity

$(\cdot)_{max}$ maximum or peak value

$(\cdot)_{rms}$ root-mean-square quantity

$(\cdot)_i$ component in the *i*th direction

$(\cdot)_f$ a fluid property

$(\cdot)_p$ a particle property

$(\cdot)^+$ normalization by wall coordinates

$(\cdot)'$ instantaneous fluctuating quantity based on Reynolds averaging

$(\cdot)''$ instantaneous fluctuating quantity based on volume fraction-weighted averaging

$(\cdot)_z$ quantity with a spanwise sense of rotation

Acronyms

CFD	computational fluid dynamics
DNS	direct numerical simulation
FFT	fast Fourier transform
GV	gravel roughness
LES	large eddy simulation
LSE	linear stochastic estimation
IA	PIV interrogation area
LDA	laser Doppler anemometry
Nd:YAG	Neodymium: Yttrium Aluminum Garnet
PDA	phase Doppler anemometry
PIV	particle image velocimetry
POD	proper orthogonal decomposition

PTV	particle tracking velocimetry
RANS	Reynolds averaged Navier-Stokes equation
SG	sand grain roughness
TKE	turbulent kinetic energy
VITA	variable interval time averaging
ZPG	zero pressure gradient

CHAPTER 1

INTRODUCTION AND OBJECTIVES

1.1 Introduction

Turbulent flows laden with small particles are encountered frequently in nature and in engineering. Examples can be found in such natural processes as sediment transport, aerosol dispersion, sand storms, cloud formation, and in varied engineering applications such as fuel combustion, spray drying, fluidization, pneumatic transport, and particle classification. In these types of applications, the flow is generally classified as a multiphase system because of the simultaneous presence of a continuous phase or carrier fluid and one or more dispersed phases such as solid particles, bubbles or drops. From the perspective of fluid dynamics, the presence of an additional phase may lead not only to local perturbations in the flow, but a number of flow properties can be significantly modified. Therefore, a fundamental understanding of multiphase flows such as particle-laden turbulent flows is crucial for formulating realistic model representations and developing better predictive schemes, with the ultimate goal of optimizing the design and process efficiencies of corresponding engineering systems.

The particular case of small solid particles loaded into a carrier fluid has received significant research attention in recent times due to the unavailability of in-depth information concerning the interaction between particles and turbulence. In particle-laden turbulent flows, particles in general, move with different velocities in comparison to the fluid due to their inertia. The result is that the relative motion between particles and the fluid leads to momentum and energy exchange between the two phases, where particles

either serve as a source or sink of momentum and energy in relation to the fluid. In practical flows, other mechanisms including effects such as particle added mass, changes in the apparent viscosity of the fluid, buoyancy, diffusion of fluid vorticity around particles, lift generated by particle rotation and shear layers, to varying degrees, also affect the hydrodynamic interactions between particles and the fluid. The immediate result then is that the presence of particles makes both the numerical modelling and experimental characterization of particle-laden flows very challenging due to the large number of factors to be accounted for. In numerical computations, the influence of particles is usually studied by introducing additional source terms into the turbulence closure equations. However, because in many RANS and LES codes the particles are inherently approximated as point (or sub-grid) forces, calculated results do not compare well with their experimental counterparts. To accurately resolve the flow around particles, DNS is sometimes employed; but because of the tremendous increase in computational effort, results are limited to only very dilute flows.

Another aspect of particle-laden turbulent flows that is not well understood and which poses further modelling challenges is when a wall roughness is present. This brings to memory the often-made remark that however undesirable roughness may be, turbulence in practice occurs typically near rough surfaces not as the exception but the rule. Examples include sediment transport over river beds, dispersion of contaminants around buildings, and lime calcination in the production of cement. In these cases the flow dynamics can become extremely complex due to wall roughness effects. In single-phase turbulent flows wall roughness has been identified to lead to enhanced wall shear stress and modifications in turbulence that may be felt over a significantly large portion

of the flow. On the other hand, particles moving adjacent to a wall are known to exhibit a variety of behaviours. For instance, they may be deposited to make the surface more rough, cause flow blockage, or because of near-wall shear, they may be lifted away from the wall, leading to enhanced mass and heat transfer rates away from the wall. Understanding these complicated interactions would definitely help to provide enhanced physical insight into wall-bounded particle-laden turbulent flows, which is a necessary step in the development of physically based models for near-wall flows.

Results of previous research on smooth-wall turbulent flows suggest that the presence of particles in turbulence can cause substantial modifications to the mean flow and turbulence characteristics even in the case of very dilute flows. The degree to which turbulence is altered is usually characterized using certain non-dimensional parameters. These include the particle volume fraction (ϕ_v), a measure of the volume occupied by particles per unit volume of the carrier fluid, particle relative diameter (d_p/L), where L represents a fluid characteristic length scale, particle Reynolds number ($Re_p = d_p|U_{rel}|/\nu$), where U_{rel} is the particle relative velocity and ν is the fluid kinematic viscosity, particle Stokes number ($St = \tau_p/\tau_f$), where τ_p and τ_f denote the particle response time and fluid time scale, respectively, particle-to-fluid density ratio (ρ_p/ρ_f), and particle mass loading [$\phi_v(\rho_p/\rho_f)$]. In flow configurations where particle settling is important, additional parameters such as the particle settling velocity ratio and the Galileo number, $Ga = [(\rho_p/\rho_f - 1)gd_p^3]^{1/2}/\nu$ (a measure of the relative importance of gravitational and viscous forces), where g is the acceleration of gravity, are used to characterize particle settling effects on turbulence. A consistent trend found in the literature has been that most investigations have been conducted under conditions in which the dispersed phase loading ratio was

maintained constant. While the obtained results may provide a fair representation of the flow in systems where the dispersed phase concentration is monitored and replenished to maintain a constant flux of particles, the same may not hold for situations where transients occur in the particle concentration. The latter phenomenon is common in systems such as fluidized beds, stirred vessels, air filters and cyclone separators where particles may not necessarily be reloaded into the flow. Variations in the particle concentration can lead to unsteady turbulence which may generate system instabilities.

In the present research a particle image velocimetry (PIV) method was used to investigate the effects of small settling particles on the turbulent flow characteristics in a horizontal water channel. Detailed measurements of particle and fluid instantaneous velocities were made for flow fields in which the particle concentration was exponentially declining. The concentration decline was initiated by adding at the commencement of each experimental run a pre-determined quantity of particles to the flow and allowing some of the particles to settle out without replenishment. Using an optical counting method the particle number densities were measured and the information was used to assess the extent of particle concentration decay over the course of the experiments. To account for the non-stationarity of the turbulence in the particle-laden turbulent flows due to the concentration decay, novel data processing techniques were applied to analyze the data.

1.2 Governing Equations

The governing equations of particle-laden turbulent flows are the continuum equations of mass, momentum and energy conservation. There are two alternative ways of prescribing

the conservation equations for a generic multiphase turbulent flow, depending on the number density of the dispersed phase. When the dispersed phase loading fraction is sufficiently high so that the fluid length scale is significantly larger than the average inter-particle spacing, both the fluid and dispersed phases are considered as interpenetrating continua. This leads to an Eulerian-Eulerian or a two-fluid description of the constitutive relations given by (Elghobashi 1994; Crowe et al. 1996):

$$\frac{\partial}{\partial t}\left(\rho_n \phi_n\right) + \frac{\partial}{\partial x_i}\left(\rho_n \phi_n U_{n,i}\right) = 0 \tag{1.1}$$

$$\frac{\partial}{\partial t}\left(\rho_n \phi_n U_{n,i}\right) + \frac{\partial}{\partial x_j}\left(\rho_n \phi_n U_{n,i} U_{n,j}\right) = \phi_n \rho_n g_i + F_{n,i} - \delta_n \left(\frac{\partial P}{\partial x_i} - \frac{\partial \sigma_{ij}}{\partial x_j}\right) \tag{1.2}$$

where equations 1.1 and 1.2 are, respectively, the individual phase mass and momentum conservation equations, ρ is the individual phase density, ϕ is the volume fraction, U is the velocity, subscript n denotes the dispersed or continuous phase, and $i, j = 1, 2, 3$ refer to the Cartesian directions x, y and z. In equation 1.2, g is the acceleration of gravity, F is the force per unit volume exerted on the component n by the other component, $\delta = 0$ and 1 for dispersed and continuous phases, respectively, P is the pressure and σ_{ij} is the deviatoric stress tensor.

In the above two-fluid formulations, it is inherently assumed that all physical properties are local averages in a control volume whose dimensions are large enough to contain a sufficient amount of the dispersed phase, but much smaller than the characteristic length scales of the flow system. Two types of such averaging techniques include volume averaging (Crowe et al. 1996) and phase-weighted averaging (Elghobashi 1994). The volume average of a property q is defined as (Crowe et al. 1996):

$$\{q\}_v = \frac{1}{V_o}\int_V q dV \tag{1.3}$$

where V is the volume of the individual phase within the control volume, V_o, and the integral is over the volume occupied by the phase. If no significant variations occur in the flow properties within the averaging volume, the volume average can provide both locally stationary values and continuous spatial derivatives for the flow properties. Nevertheless, if these criteria are satisfied but for one reason or another the averaging volume size is larger than the smallest length scale of the continuous phase turbulence, for example, as may be necessitated when large particles are involved, then the volume-averaged equations cannot be expected to accurately resolve the continuous phase turbulence. In phase-weighted averaging, each flow property is decomposed into a phase-weighted mean, $<q>$ and a fluctuating component q'' as

$$q_n = \langle q \rangle_n + q_n'' \tag{1.4}$$

where the phase-weighted mean is given by

$$\langle q \rangle_n = \frac{\overline{\phi_n q_n}}{\overline{\phi_n}} \tag{1.5}$$

and the overbar is used to denote time or ensemble averaging.

For dilute flows, the continuum assumption holds only for the continuous phase so that the Eulerian-Eulerian formulation no longer applies. The work-around is to treat the carrier phase as a continuum and the dispersed phase as discrete particles. This is called the Eulerian-Lagrangian representation.

Thus, for an individual particle of the dispersed phase, the momentum equation, after expanding the expression on the left hand side of equation 1.2, and using the continuity equation becomes

$$\rho V \frac{\partial}{\partial t}\left(U_i{}^p\right) + \rho V U_j{}^p \frac{\partial}{\partial x_j}\left(U_i{}^p\right) = \rho V g_i + F_i \tag{1.6}$$

which simplifies to

$$m^p \frac{dU_i{}^p}{dt} = F_i + m^p g_i \tag{1.7}$$

where m^p is the mass of the particle and d/dt (= $\partial/\partial t + U_j^p \partial/\partial x_j$) is the Lagrangian or material derivative following the particle. The external force term F_i which represents the influence of the continuous phase on the particle may originate from many contributions such as viscous drag on the particle, lift due to shear (Saffman forces) and particle rotation (Magnus forces), buoyancy, pressure gradient in the surrounding fluid in the direction of motion, as well as contributions from impulsive effects such as inter-particle collisions and particle-wall collisions. For a spherical particle of size smaller than the fluid length scale, density much larger than the surrounding fluid and Reynolds number $Re_p < 1$, Maxey and Riley (1983) derived expressions for most of the contributions to F_i based on an earlier work by Tchen (1947) as

$$\begin{aligned} m^p \frac{dU_i{}^p}{dt} &= 3\pi\mu d_p\left(U_i{}^f - U_i{}^p + \tfrac{1}{24} d_p{}^2 \nabla^2 U_i{}^p\right) \\ &+ \tfrac{3}{2}\pi d_p{}^2 \mu \int_0^t \left(\pi\nu(t-\tau)\right)^{-1/2} \frac{d}{d\tau}\left(U_i{}^f - U_i{}^p + \tfrac{1}{24} d_p{}^2 \nabla^2 U_i{}^f\right) d\tau \\ &+ \tfrac{1}{2} m^f \frac{d}{dt}\left(U_i{}^f - U_i{}^p + \tfrac{1}{40} d_p{}^2 \nabla^2 U_i{}^f\right) \\ &+ m^f \frac{DU_i{}^f}{Dt} \\ &+ \left(m^p - m^f\right) g_i \end{aligned} \tag{1.8}$$

where m^f is the mass of the fluid displaced by the particle, d_p is the particle diameter, $U_i{}^f$ is the ith component of the fluid velocity and DU_i^f/Dt is the corresponding fluid material derivative. The first term on the right hand side of equation 1.8 is called the Stokes drag

term, representing the steady viscous Stokes drag. The second term is called the Basset history force, and is important for high frequency oscillatory flows. The third term represents the force required to accelerate the fluid displaced by the particle in the frame of reference of the moving particle. This force, also known as the added mass force, is important only for unsteady flows, and can be neglected when the particle-fluid density ratio is much larger than 1. The fourth term is the fluid acceleration force due to pressure gradient effects and viscous shear stresses of the fluid. The last term is the buoyancy force. For motion in a uniform, quiescent fluid, the only forces acting on the particle are buoyancy and viscous drag.

For a particle with $Re_p << 1$ (creeping flow), Stokes (1851) gave the drag force experienced by the particle as:

$$F_D = -3\pi d_p \mu \left(U_p - U_f\right) \tag{1.9}$$

where μ is dynamic viscosity of the fluid. The drag force can be used to define a drag coefficient, C_D, given by

$$C_D = \frac{\left|F_D\right|}{\frac{\pi}{8} d_p{}^2 \rho_f \left(U_p - U_f\right)^2} \tag{1.10}$$

and which after substitution of equation 1.9 gives

$$C_D = \frac{24}{Re_p} \tag{1.11}$$

where $Re_p = d_p|U_p\text{-}U_f|/\nu$. Equation 1.11 represents the drag coefficient for Stokesian flow. With larger particle Reynolds numbers, this equation underpredicts the drag coefficient. To account for the effects of finite Reynolds number, Torobin and Gauvin (1959) suggested an empirical drag correlation of the form

$$C_D = \frac{24}{Re_p}\left(1 + 0.15 Re_p^{\,0.687}\right) \tag{1.12}$$

which is found to remain valid for values of Re_p up to 700.

The particle equation of motion is sometimes written in a simpler form that neglects the second derivatives (also known as the Faxen corrections due to velocity curvature). Thus, by dropping the Faxen corrections and substituting $m^p = \rho_p \pi d_p^{\,3}/6$, $m^f = \rho_f \pi d_p^{\,3}/6$, and rearranging the terms, equation 1.8 becomes

$$\frac{\pi}{6} d_p^{\,3} \rho_p \frac{dU_i^{\,p}}{dt} + \frac{1}{2}\frac{\pi}{6} d_p^{\,3} \rho_f \frac{d}{dt}\left(U_i^{\,p} - U_i^{\,f}\right) = 3\pi\mu d_p \left(U_i^{\,f} - U_i^{\,p}\right) + \frac{\pi}{6} d_p^{\,3} \rho_f \frac{DU_i^{\,f}}{Dt}$$

$$+ \tfrac{3}{2} d_p^{\,2} \sqrt{(\pi \rho_f \mu)} \int_0^t \frac{\dfrac{d}{d\tau}\left(U_i^{\,f} - U_i^{\,p}\right)}{\sqrt{(t-\tau)}} d\tau + \frac{\pi}{6} d_p^{\,3} \left(\rho_p - \rho_f\right) g_i \tag{1.13}$$

For a particle whose diameter and relative displacement are much smaller than the fluid Kolmogorov length scale, $\eta = (\nu^3/\varepsilon)^{1/4}$ the material derivatives d/dt and D/Dt are nearly indistinguishable (Hinze 1972), so that equation 1.13 can be expressed in the form (Hinze 1972):

$$\frac{dU_i^{\,p}}{dt} + c_1 U_i^{\,p} = c_1 U_i^{\,f} + c_2 \frac{dU_i^{\,f}}{dt} + c_3 \int_0^t \frac{dU_i^{\,f}/dt - dU_i^{\,p}/dt}{\sqrt{(t-\tau)}} d\tau + \left(1 - \frac{\rho_f}{\rho_p}\right) g_i \tag{1.14}$$

where $c_1 = \dfrac{18\nu}{\left(\dfrac{\rho_p}{\rho_f} + \dfrac{1}{2}\right) dp^2}$; $c_2 = \dfrac{3/2}{\left(\dfrac{\rho_p}{\rho_f} + \dfrac{1}{2}\right)}$; $c_3 = \dfrac{9}{\left(\dfrac{\rho_p}{\rho_f} + \dfrac{1}{2}\right) dp} \sqrt{(\nu/\pi)}$. (1.15)

The constant c_1 has a dimension of s^{-1}, which when inverted gives the Stokesian particle relaxation time

$$\tau_p = \frac{\left(2\rho_p + \rho_f\right) d_p^{\,2}}{36\mu} \tag{1.16}$$

For systems with $\rho_p >> \rho_f$ such as gas-solid flows, equation 1.16 reduces to

$$\tau_p = \frac{1}{18}\left(\frac{\rho_p}{\rho_f}\right)\frac{d_p^{\,2}}{\nu} \tag{1.17}$$

For $Re_p > 1$, the corrected particle relaxation time is given by (Fessler and Eaton 1999):

$$\tau_p = \frac{\tau_{p,Stokes}}{\left(1 + 0.15 Re_p^{\,0.687}\right)} \tag{1.18}$$

where $\tau_{p,Stokes}$ is the Stokesian relaxation time given by equation 1.16 or 1.17.

The ratio of the particle response time to the fluid characteristic time scale, τ_f, or Stokes number, $St = \tau_p/\tau_f$, is a useful dimensionless parameter for measuring the responsiveness of the particle to the fluid motion. For turbulent flows, the fluid time scale is generally given by the ratio of any suitable length scale of the flow to a corresponding velocity scale. For instance, when it is important to measure the response of the particle to the smallest scales of the flow, the relevant time scale is the fluid Kolmogorov time scale given by $\tau_f = \eta/v_k$, where $v_k = (\nu\varepsilon)^{1/4}$ is the Kolmogorov velocity scale. Other formulations of τ_f employed in the literature include the ratio of the Taylor microscale to the streamwise turbulent intensity, λ_T/u_{rms} (Best et al. 1997), the ratio of the size of the large eddies to the friction velocity, L_e/U_τ (Kaftori et al. 1995b; Righetti and Romano 2004), or of the flow height to the velocity of the bulk flow, h/U_{max} (Vreman 2007). Thus, knowing the Stokes number, it is possible to determine how readily a particle will respond to fluctuations in the fluid velocity. For example, if the fluid velocity fluctuations occur over a time scale much shorter than the particle relaxation time ($St >> 1$), the particle will be unaffected by the fluid fluctuations. If, on the other hand, the fluid velocity fluctuations occur over a time scale much longer than the particle relaxation time ($St << 1$), the particle will follow the fluid motion exactly.

1.3 Research Motivation and Objectives

A large part of the available data on particle-laden wall-bounded turbulent flows is due to research conducted over smooth walls for the generic case where the particulate phase is fed at a relatively steady rate. Even in these cases many fundamental questions such as how particles impact turbulence still remain unresolved due partly to the complex nature of the interactions between particles and the flow. This lack of answers makes the characterization of corresponding rough-wall flows an even more challenging task. Thus, despite the many practical applications in fluids engineering, roughness effects on particle-laden turbulent flows have been studied far less. Compounded with this is the observation that the available research is focused mainly on the investigation of only single-point quantities such as the mean velocity and relative turbulence intensities. In order to gain a deeper understanding of particles effect on the structure of turbulence, multipoint statistics such as two-point correlations are necessary. For the special case of time-dependent particle loading ratios, possible unsteadiness in the continuous phase turbulence renders statistical results obtained from operations such as ensemble averaging unreliable.

In response to the immediate need to fill these knowledge gaps, a comprehensive experimental investigation was undertaken using a novel dual-phase PIV to study the effects of unsteady particle concentration and surface roughness on low Reynolds number particle-laden turbulent flows in a two-dimensional channel. Two types of particles were used: solid glass of density 2500kg/m^3 and nominal mean diameter 50 μm, and polymethyl methacrylate (PMMA) particles of density 1190 kg/m^3 and nominal mean diameter 150 μm. In order to provide a more accurate description of the results, non-

stationary averaging techniques were employed in analyzing the data. It is also sought to take full advantage of the whole-field capability of PIV to examine the impact of particles and wall roughness on the structural properties of the flow. In this regard, flow visualizations and various coherent structure identification techniques are employed to deepen insight into turbulence modification by the particles. Finally, it is aimed that the results reported here will help to improve our understanding of particle-laden rough-wall turbulent flows, and draw attention to the more interesting, non-uniform loading type of particle-laden turbulent flows.

1.4 Organization of the Thesis

The thesis is organized as follows. In Chapter 2, a survey of the literature on particle-laden turbulent flows, specifically, those in channels and zero pressure gradient (ZPG) turbulent boundary layers is presented. Highlights of the test conditions and main findings of the references are presented and the experimental or numerical methods employed are pointed out. The chapter concludes with a description of the coherent structure identification techniques used in the present investigation. Chapter 3 describes the experimental details and the test conditions considered. Details are given of the PIV measurement system and its implementation, as well as the image processing approach used for calculating the particles number densities. Chapter 4 presents the main results of the experiments. Data analysis techniques include variable interval time averaging (VITA), proper orthogonal decomposition and wavelet decomposition. Finally, Chapter 5 provides a summary of the results and the main findings reported in the thesis, along with some recommendations for future work.

CHAPTER 2

LITERATURE REVIEW

2.1 Overview

Wall-bounded particle-laden flows have been studied in the past using a variety of techniques, including analytical calculations, computational fluid dynamics (CFD) and experimental methods. Most theoretical calculations consider the motion of only a single particle under creeping flow conditions, using a number of simplifying assumptions to reduce the governing equations to ordinary linear differential equations (e.g., Stokes 1851; Basset 1888; Hinze 1972). CFD methods such as Reynolds-averaged Navier-Stokes (RANS) modeling, direct numerical simulation (DNS) and large-eddy simulation (LES) rely on the processing power of the computer to solve the discretized differential equations for more practical flows. However, the failure of most numerical solutions to accurately predict particle-fluid interactions makes it more attractive to use experimental methods. Some previous experimental investigations, for instance, employed hotwires and Pitot tubes to measure the velocity of the fluid phase and image processing techniques to determine the velocity of particles. Nevertheless, the invasive nature of the hotwire and Pitot tube serves as a major drawback due to local disturbances they cause to the flow by producing wakes. With the recent advancements in laser technology and digital photography these classical methodologies have been replaced by such non-invasive techniques as laser Doppler anemometry (LDA), phase Doppler anemometry (PDA) and full-field techniques such as particle image velocimetry (PIV) and particle tracking velocimetry (PTV). A vivid review of these optical techniques for the

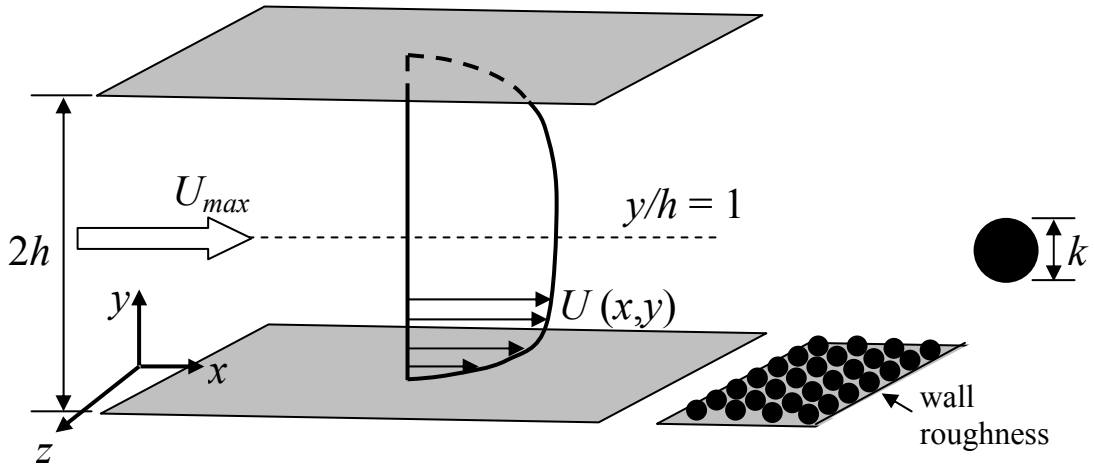

Figure 2.1: Schematic of a fully developed channel flow.

experimental study of two-phase flows is given in Boyer et al. (2002).

Previous wall-bounded turbulent flows relevant to this study include flows in turbulent channels and ZPG turbulent boundary layers. Since the understanding of wall-bounded particle-laden turbulent flows is predicated on a firm background in corresponding single-phase turbulent flows, a brief overview of the latter is in order. Unladen wall-bounded turbulent flows such as those in channels and boundary layers are considered fundamentally important because they provide the framework for testing classical wall turbulence scaling laws and models. It is well recognized that the boundary layer in wall turbulence is a composite fluid layer consisting of both inner and outer regions (Prandtl 1932). For a fully developed channel flow as shown schematically in figure 2.1, the inner layer corresponds to the region extending from the wall ($y/h = 0$) to $y/h \approx 0.2$ (Jiménez 2004), where h is the channel half-height. In this figure, U is the streamwise mean velocity, U_{max} is the centre-line or maximum streamwise mean velocity, and the flow direction is from left to right. In the inner region, because of the presence of

the wall, the turbulence dynamics depend on the friction velocity, U_τ, the fluid kinematic viscosity, ν, and the distance from the wall (y). This leads to two types of scaling parameters for the inner region, namely, the viscous length scale, ν/U_τ, and the viscous time scale, ν/U_τ^2. In the outer layer ($0.2 \leq y/h \leq 1.0$), the wall acts to retard the fluid velocity in a manner that is independent of viscosity, but depends on the distance from the wall, and the outer variables h and U_{max}. At sufficiently high Reynolds numbers, an overlap region exists between the outer and inner layers. For smooth wall flows, the overlap region is described by a logarithmic mean velocity profile of the form $U^+ = (1/\kappa)$ $ln(y^+) + B$ (Milikan 1938), where κ is the von Kármán constant and B is an additive constant. Typical values of the logarithmic law constants are ($\kappa = 0.41$, $B = 5.0$) or ($\kappa = 0.40$, $B = 5.5$). Knowing the friction velocity enables the determination of the surface drag characteristics such as the wall shear stress, $\tau_w = \rho U_\tau^2$, and the skin friction coefficient, $C_f = 2(U_\tau/U_{max})^2$. Based on the friction velocity and maximum streamwise mean velocity, respectively, two Reynolds numbers can be defined, namely, the friction Reynolds number (or Kármán number), $Re_\tau = hU_\tau/\nu$, which compares the outer scale (size of the larger eddies) to the viscous length scale, and the channel half-height Reynolds number, $Re_h = hU_{max}/\nu$, which can be used to assess the relative importance of inertial and viscous forces.

When the flow passes over a rough wall, the effect of roughness is to disrupt the flow leading to modification of the inner layer structure. When the roughness height k is large enough, the modifications can extend well into the outer layer. Generally speaking, the effect of the roughness is to enhance the drag characteristics and produce a shift in the logarithmic streamwise mean velocity profile of the form $U^+ = (1/\kappa)ln(y+y_o)^+ + B - \Delta B^+$,

where ΔB^+ is the amount by which roughness changes the mean velocity, y is the distance measured from the roughness crest and y_o is the virtual origin, which depends on the size and distribution of the roughness elements. The presence of the rough wall leads to an additional Reynolds number, $k^+ = kU_\tau/\nu$, called the roughness Reynolds number, which compares the roughness height to the viscous length scale. Because of the latter attribute, the k^+ values are used to encode information as to how deep roughness effects penetrate the flow. When k^+ is small, the flow is hydraulically smooth, in which case the turbulent eddies shed by the roughness elements are completely damped by fluid viscosity, and the skin friction is due entirely to viscous forces. As k^+ increases, the flow becomes transitionally rough so that viscosity is no longer able to damp the eddies produced by the roughness elements. The net effect is that both form drag by the roughness elements and viscous drag contribute to the overall skin friction. With further increase in k^+, the flow becomes fully rough and form drag is the pre-dominant contributor to skin friction. To compare roughness effects among different flows, irrespective of the specific type of roughness used, Nikuradse (1933) suggested the equivalent sand grain roughness height, k_s, which represents the size of monodisperse sand grains to provide the same skin friction coefficient as the roughness in question. Using the dimensionless equivalent sand grain roughness height, k_s^+, Schlichting (1979) suggested that the flow may be considered hydraulically smooth for $0 < k_s^+ \leq 5$, transitionally rough for $5 < k_s^+ < 70$, and fully rough for $k_s^+ \geq 70$.

Roughness effects on wall turbulence have been studied in the past using various types of materials such as sand grains (Nikuradse 1933), wire mesh (Krogstad et al. 1992, Tachie et al. 2000), pyramids (Hong et al. 2011) and two-dimensional transverse

elements (Leonardi et al. 2004). In addition to enhanced drag, the presence of roughness is documented to lead to a reduction in the streamwise mean velocity (Krogstad et al. 1992; Tachie et al. 2000), and an increase in the values of the turbulence intensities and Reynolds stresses (Krogstad et al. 1992; Tachie et al. 2000).

2.2 The Near-Wall Turbulence Structure

Instantaneous visualization and statistical results from many wall-bounded turbulent flows indicate that turbulence close to a wall is composed of certain structural elements called coherent structures that provide the generation and self-sustaining mechanism for the turbulence. In the literature, coherent structures have been defined in different ways by different authors, including the following: that, they are regions of space and time within which the flow field has a characteristically coherent or regular pattern (Pope 2000); or they are connected regions of large-scale turbulent fluid motions having phase-correlated vorticity over their spatial extents (Hussain 1983), or three-dimensional regions of the flow field over which at least one fundamental flow variable (e.g., velocity, density or temperature) exhibits significant correlation with itself or with another variable with length and time scales larger than the smallest scales of the flow (Robinson 1991). In simple terms, therefore, in the case of velocity fields, coherent structures are regions in the flow marked by significant auto- and cross-correlation between the velocity fluctuations. Their presence in turbulence is evidenced, for instance, in the non-zero Reynolds shear stress and the two-point spatial correlations. Coherent structures identified in wall-bounded turbulent flows have been extensively reviewed for both the inner layer (Kline et al. 1967; Cantwell 1981; Robinson 1991) and the outer layer (Head

and Bandyopadhyay 1981; Adrian et al. 2000a). Some of the commonly observed structures in the near-wall region include low-speed streaks with spanwise spacing of about 100 wall units (Kline et al. 1967), bursts (Grass 1971), sweeps and ejections (Corino and Brodkey 1969); quasi-streamwise vortices (Blackwelder and Eckelmann 1979), Q2/Q4 events (Wallace et al. 1972; Lu and Wilmarth 1973), where Q2 and Q4 are the second and fourth quadrants of the plane of streamwise and wall-normal velocity fluctuations, and inclined shear layers (Brown and Thomas 1977; Kim 1987; Schoppa and Hussain 2000). The outer layer is envisaged to be occupied by loop-like vortices (Head and Bandyopadhyay 1981; Smith et al. 1991), large-scale three-dimensional bulges (Blackwelder and Kaplan 1976; Falco 1977) and often times very large scale motions (Jimenez 1998; Kim and Adrian 1999). Despite the extensive study of these structures for near-wall flows, there is still no general consensus as to which one of them is the most dominant in the production and sustenance of turbulence. Also causing controversy among researchers is the issue of identifying the exact mechanisms responsible for the generation of the coherent wall structures. To explain the origin of coherent structures in wall turbulence various mechanisms have been proposed. Schoppa and Hussain (2002), for instance, used a linear perturbation method to show that strong quasi-streamwise vortices are due to induction by the transient growth of low-speed streaks. Smith et al. (1991) and Zhou et al. (1999) applied the hairpin vortex model of Theodorsen (1952) to suggest a parent-offspring mechanism where a single hairpin vortex of sufficient strength can spawn an offspring hairpin vortex. This may occur either through the process of unsteady separation of a single hairpin vortex from the wall to produce localized ejections that subsequently roll up to produce new vortices (Smith et al. 1991), or by a parent

hairpin generating strong shear layers that roll up into arch vortices that subsequently merge with existing streamwise oriented legs to form a new hairpin vortex (Zhou et al. 1999).

A number of studies have emphasized the hairpin vortex as a simple coherent structure that explains many of the features observed in wall-bounded flows. Theodorsen (1952) described the hairpin vortex as either a symmetric or asymmetric hairpin-like structure, and its modified versions, that produce regions of intense negative streamwise and positive wall-normal velocity fluctuations under a clearly defined spanwise rotating vortex head. Figure 2.2 shows a schematic of a hairpin vortex (proposed by Adrian et al. 2000a). Using this structural model makes it possible to explain many of the other types of coherent structures observed in near-wall turbulent flows. The vortex consists of a spanwise rotating head that is connected to the neck inclined at an angle of approximately 45° to the streamwise (x) direction. The neck is connected to the two quasi-streamwise legs which correspond to previously documented counter-rotating quasi-streamwise vortices near the wall. Also, due to their rotation, the quasi-streamwise vortices induce regions of negative streamwise velocity fluctuations corresponding to the low-speed streaks near the wall. The vortex head when viewed in the streamwise wall-normal plane corresponds to spanwise vortex cores whose vorticity are of the same sign as the mean shear. Such spanwise vortices are called prograde vortices, while those with vorticity opposite to that of the mean shear are called retrograde vortices (Wu and Christensen 2006). The spanwise rotation of the vortex head induces Q2 motions or ejections underneath the vortex, accompanied by opposite Q4 or sweep-type motions outboard of the vortex. The opposing Q2 and Q4 motions form an inclined shear layer, and where

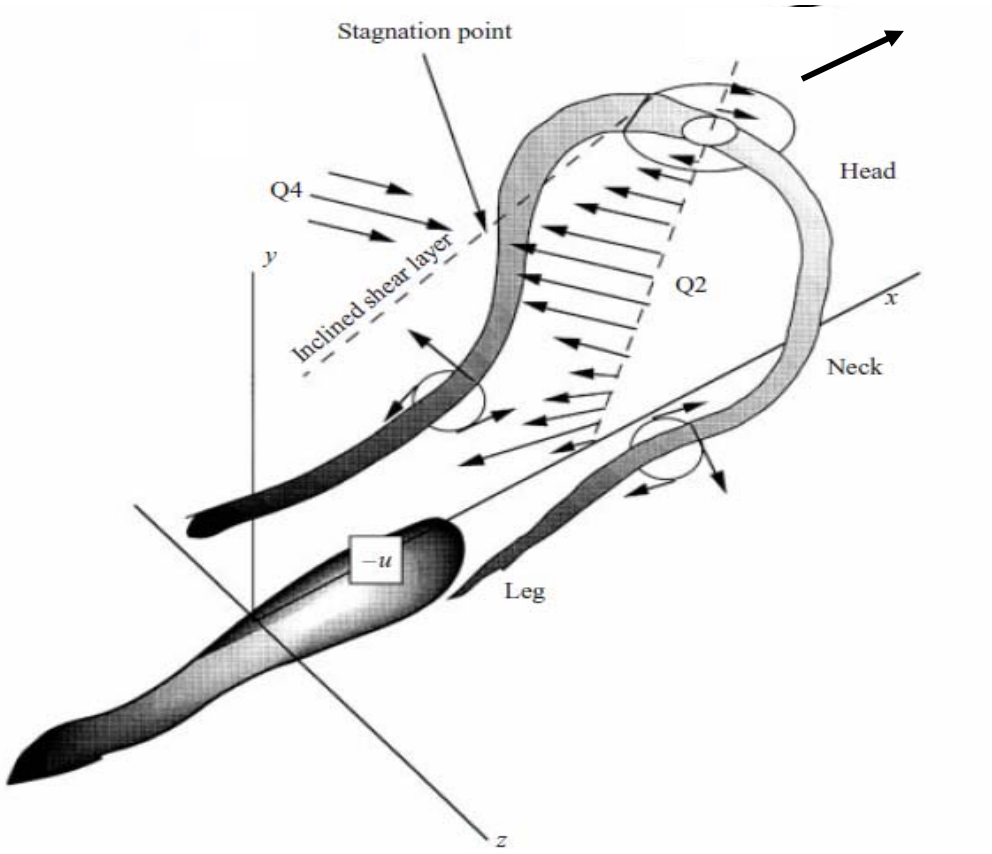

Figure 2.2: Schematic of a hairpin vortex attached to the wall and the induced motion. Figure is taken from Adrian et al. (2000a).

their velocity fluctuation magnitudes cancel out creates a region of stagnation flow along the edge of the shear layer.

Even though the hairpin vortex model has been well received within the near-wall turbulence community, it is still not clear how the vortices are organized when they occur in groups. The study reported by Adrian et al. (2000a), for instance, suggests that the hairpin vortices sometimes occur in groups of two or more vortices convecting at a common velocity. They called this a hairpin packet. A common convection velocity of the hairpin vortices in a packet leads to a coherent alignment of the vortices in the streamwise direction at relatively shallow angles of approximately 10° - 20° to the wall.

It was found that as the vortices pass over the wall they grow into the outer layer at a rate that is proportional to their distance from the wall. The viewpoint of a coherently aligned hairpin vortices growing into the outer layer has been found to be in conflict with studies such as DNS computations of channel flow (del Alamo et al. 2006) and theoretical calculations (Perry and Chong 1982) that show a random distribution of the hairpin vortices. Thus, the question is still open for a unifying theory of the structural organization of wall-bounded turbulent flows.

2.2.1 Some Techniques for Educing Coherent Structures

Several methodologies have been developed in the literature for extracting coherent structures from turbulent flows. Most of these are comprehensively discussed in a number of previous articles, including Adrian et al. (2000b) and Alfonsi (2006). Those explored in the present study are quadrant decomposition, swirling strength, linear stochastic estimation (LSE), proper orthogonal decomposition (POD), and wavelet decomposition. The details of how these are implemented are now presented.

2.2.1.1 Quadrant Decomposition

Quadrant decomposition is used to investigate the intensity of the Reynolds shear stress produced by the coherent structures. The method consists of sorting the instantaneous Reynolds shear stress, uv, into the four quadrants of the u-v plane depending on the signs of u and v. The first quadrant (Q1: $u>0$ and $v>0$) referred to as the outward interaction term contains outward motion of high-speed fluid; the second quadrant (Q2: $u<0$, $v>0$)

contains the motions associated with ejection of low-speed fluid away from the wall; the third quadrant (Q3: $u<0$ and $v<0$), also called the inward interaction term, contains the inward motion of low-speed fluid; and the fourth quadrant (Q4: $u>0$ and $v<0$) contains an inrush of high-speed fluid (or sweeps). Thus, Q2 and Q4 events contribute to negative Reynolds shear stress, while Q1 and Q3 events contribute to the positive Reynolds shear stress. Following Lu and Willmarth (1973), the mean Reynolds shear stress at a given wall-normal location is decomposed into contributions from the quadrants excluding a hyperbolic hole of size H (see figure 2.3) as

$$\overline{uv}_Q(x,y,H) = \frac{1}{N}\sum_{i=1}^{N} u_i(x,y)v_i(x,y)S_Q(x,y,H) \tag{2.1}$$

where N is the total number of instantaneous velocity vectors (= total number of PIV snapshots) at a given wall-normal location and S_Q is a detector function given by

$$S_Q(x,y,H) = \begin{cases} 1, \text{ when } \left|u_i(x,y)v_i(x,y)\right|_Q \geq Hu_{rms}(x,y)v_{rms}(x,y) \\ 0, \text{ otherwise} \end{cases} \tag{2.2}$$

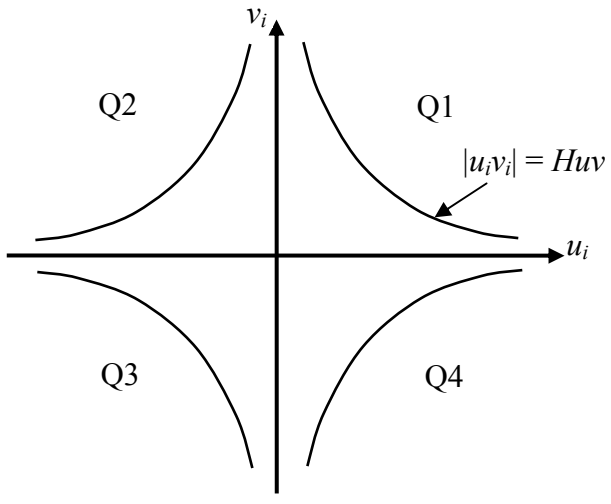

Figure 2.3: Sketch of the four quadrants and hole region of the u-v plane.

The hole size H represents a threshold on the strength of the Reynolds shear stress producing events, with $H = 0$ allowing all uv events to be included in the decomposition, and higher values of H allowing the inclusion of only increasingly intense Reynolds shear stress producing events. The contribution to the Reynolds shear stress from the hole region is given by

$$\overline{uv}_Q(x,y,H) = \frac{1}{N}\sum_{i=1}^{N} u_i(x,y)v_i(x,y)S_h(x,y,H) \tag{2.3}$$

where

$$S_h(x,y,H) = \begin{cases} 1, \text{ if } |u_i(x,y)v_i(x,y)| < Hu_{rms}(x,y)v_{rms}(x,y) \\ 0, \text{ otherwise} \end{cases} \tag{2.4}$$

By accumulating the values of S_Q, the space fraction N_Q can be calculated as

$$N_Q(x,y,H) = \frac{\sum S_Q(x,y,H)}{N} \tag{2.5}$$

2.2.1.2 Swirling Strength

Swirling strength is a term used to describe the imaginary part of the complex eigenvalues of the velocity gradient tensor and provides a means for identifying vortex cores in a flow field. In three dimensions, the local velocity gradient tensor will have one real eigenvalue λ_r, and a pair of complex conjugate eigenvalues ($\lambda_{cr} \pm i\lambda_{ci}$) when the discriminant of its characteristic equation is positive (Zhou et al. 1999). Chong et al. (1990) observed that when complex eigenvalues occur, fluid particle trajectories about the eigenvector corresponding to λ_r exhibit a spiralling motion with a period of magnitude λ_{ci}^{-1}. For a planar PIV velocity field, the complete local velocity gradient tensor is unavailable. Thus, only a two-dimensional swirling strength can be calculated using the

in-plane velocity gradients (Adrian et al. 2000b; Hutchins et al. 2005), and which in the *x-y* plane is formulated as

$$\begin{vmatrix} \frac{\partial U}{\partial x} - \lambda & \frac{\partial U}{\partial y} \\ \frac{\partial V}{\partial x} & \frac{\partial V}{\partial y} - \lambda \end{vmatrix} = 0 \tag{2.6}$$

This is a quadratic equation with solution given by

$$\lambda = \frac{1}{2}\left(\frac{\partial U}{\partial x} + \frac{\partial V}{\partial y}\right) \pm \frac{1}{2}\sqrt{\underbrace{\left(\frac{\partial U}{\partial x} + \frac{\partial V}{\partial y}\right)^2}_{b^2} - \underbrace{4\left(\frac{\partial U}{\partial x}\frac{\partial V}{\partial y} - \frac{\partial V}{\partial x}\frac{\partial U}{\partial y}\right)}_{4ac}} \tag{2.7}$$

Since the swirling strength, λ_{ci}, is defined at a location where the solution is complex, the magnitude of swirling strength associated with the spanwise vortex core at that location becomes

$$\lambda_{ci,z} = \frac{1}{2}\sqrt{\left|b^2 - 4ac\right|} \quad \text{where } 4ac > b^2. \tag{2.8}$$

In this form, the swirl has no sign information. Sign is however recovered by multiplying $\lambda_{ci,z}$ by the sign of the local in-plane instantaneous fluctuating vorticity. Using notation from previous studies (e.g., Wu and Christensen 2006), the instantaneous signed swirling strength is given by

$$\Lambda_{ci,z} = \lambda_{ci,z}\left(\frac{\omega_z'}{|\omega_z'|}\right) \tag{2.9}$$

where ω_z' is the instantaneous fluctuating vorticity.

The advantage of swirling strength, $\lambda_{ci,z}$ over the vorticity, ω_z, is that $\lambda_{ci,z}$ can be used to unambiguously differentiate between regions with vorticity arising from pure

rotation and those with vorticity originating from shear. The swirling strength criterion will also be beneficial for two-phase flows in identifying regions of low vorticity (or high strain rate), where inertial particles have been reported to segregate.

2.2.1.3 Linear Stochastic Estimation

Stochastic estimation is a least-square method for approximating conditional averages based on a set of prescribed events. The technique was first applied by Adrian (1977) to estimate the conditionally averaged flow structures associated with turbulent boundary layers.

In general, the conditional average of a function U denoted $\overline{U \mid E}$ where E is a set of event data is defined as (Adrian et al. 1989)

$$\overline{U \mid E} = \int \frac{f(U,E)}{f(E)} U dU \qquad (2.10)$$

where $f(U, E)$ is the joint probability density function of U and E, and $f(E)$ is the probability density function of E. While equation 2.10 is the best estimate of the conditional average, its direct computation is impractical due to the large number of events that must be included for the results to converge. The stochastic estimate of the conditional average $\overline{U \mid E}$ where U_i is the ith component of velocity is obtained by expanding the conditional average in a Taylor series about $E = 0$, and truncating the series at some level (Adrian et al. 1989). Thus, assuming $E = (E_1, E_2, E_3, ..., E_N)$, where the E_i's are fluctuations with respect to the mean, $\overline{U \mid E}$ is expanded as follows (Adrian et al. 1989):

$$\overline{U_i \mid E} = L_{ij} E_j + M_{ijk} E_j E_k + N_{ijkl} E_j E_k E_l + ... \tag{2.11}$$

The unknown coefficients L, M, N, ... are determined by requiring that the mean-square error between the approximation and the conditional average be minimized,

$$\overline{[\overline{U_i \mid E} - L_{ij} E_j - M_{ijk} E_j E_k - N_{ijkl} E_j E_k E_l - ...]^2} = \text{minimum.} \tag{2.12}$$

In the case of linear stochastic estimation, only the first term in equation 2.11 is retained. The minimization leads to the orthogonality principle which states that the error must be statistically uncorrelated with each of the data. That is,

$$\overline{\left[\langle U_i \mid E \rangle - L_{ij} E_j\right] E_k} = 0\,, \quad i = 1, 2, 3 \quad j, k = 1, 2, 3, ..., N. \tag{2.13}$$

which on simplification yields

$$\overline{E_j E_k} L_{ij} = \overline{U_i E_k}\,, \qquad j, k = 1, 2, 3, ..., N. \tag{2.14}$$

Expanding equation 2.14 for indices j and k leads to a linear system of equations (or the Yule-Walker equations) which can be solved for the estimation coefficients L_{ij}.

$$\begin{aligned}
&\overline{U_i E_1} = L_{i1}\overline{E_1 E_1} + L_{i2}\overline{E_1 E_2} + ... + L_{iN}\overline{E_1 E_N} \\
&\overline{U_i E_2} = L_{i1}\overline{E_2 E_1} + L_{i2}\overline{E_1 E_2} + ... + L_{iN}\overline{E_2 E_N} \\
&..... \\
&..... \\
&\overline{U_i E_N} = L_{i1}\overline{E_N E_1} + L_{i2}\overline{E_N E_2} + ... + L_{iN}\overline{E_N E_N}
\end{aligned} \tag{2.15}$$

For a scalar event E at the reference location (x_{ref}, y_{ref}), equation 2.15 reduces to

$$\overline{U_i(x_{ref} + \Delta x, y) \cdot E(x_{ref}, y_{ref})} = L_i \overline{E(x_{ref}, y_{ref}) \cdot E(x_{ref}, y_{ref})} \tag{2.16}$$

from where the corresponding LSE coefficient is obtained as

$$L_i = \frac{\overline{U_i(x_{ref} + \Delta x, y) \cdot E(x_{ref}, y_{ref})}}{\overline{E(x_{ref}, y_{ref})^2}} \tag{2.17}$$

Then, using equations 2.16 and 2.17, the LSE of the conditional average of the *i*th component of velocity (*u* or *v*) is given by

$$\overline{U_i(x_{ref}+\Delta x, y) \mid E(x_{ref}, y_{ref})} = \frac{\overline{U_i(x_{ref}+\Delta x, y)\cdot E(x_{ref}, y_{ref})}}{\overline{E(x_{ref}, y_{ref})^2}} E(x_{ref}, y_{ref}) \quad (2.18)$$

Equation 2.18 allows the reconstruction of the average velocity field associated with a given value of *E* (Christensen and Adrian 2001). The event *E* can be set as *u* or *v*, a single component of vorticity vector (e.g. ω_z) or swirling strength $\Lambda_{ci,z}$.

2.2.1.4 Proper Orthogonal Decomposition

Proper orthogonal decomposition (POD) is used to extract coherent structures from an ensemble of data by decomposing the data into an infinite series of spatial eigenfunctions. The POD eigenfunctions provide an optimal basis for expansion of the flow in the sense that their energy convergence is more rapid than any other representation. The POD method was first introduced by Lumley (1967) for analysis of turbulent flows. Its advantage is that it is a more objective method of educing the coherent structures in comparison to conditional averaging techniques such as LSE which require *a priori* knowledge of the presence of a coherent structure in the flow.

Mathematically speaking, the goal of POD is to seek orthogonal spatial eigenfunctions, $\Phi(x)$ so that each member $U(x, t)$ of an ensemble of instantaneous realizations can be expressed as

$$U(x,t) = a_0\Phi_0(x) + \sum_{n=1}^{\infty} a_n(t)\Phi_n(x) \quad (2.19)$$

where $a_n(t)$ are time coefficients. The zeroth eigenfunction, or Mode 0, Φ_0, represents the mean flow field while subsequent modes contain the fluctuations. Following Berkooz et

al. (1993), the values of the eigenfunctions are chosen so as to maximize a functional of the form

$$\frac{\overline{\left|(U,\Phi)\right|^2}}{(\Phi,\Phi)} \tag{2.20}$$

where (g, h) denotes the inner product

$$(g,h) = \int_{\Omega_x} g(x)\, h^*(x)\, dx \tag{2.22}$$

In equation 2.22, the function $h^*(x)$ is the complex conjugate of $h(x)$. Applying a calculus of variations procedure on equation 2.20 with the restriction that $(\Phi,\Phi) = 1$ leads to a Fredholm integral equation of the form

$$\int_{\Omega_x} \langle u(x)u(x')\rangle \Phi(x')dx' = \lambda\Phi(x) \tag{2.22}$$

where the kernel $\langle u(x)u(x')\rangle$ is the two-point autocovariance function. Solving equation 2.22 for $\Phi(x)$ and eigenvalues λ requires the autocovariance function to be calculated at all spatial points in the domain Ω_x. In practical applications such as PIV, where high spatial resolution is required, the number of grid points is usually very large leading to an extremely large eigenvector problem.

In the present study, the POD analysis is carried out using the Sirovich's (1987) method of snapshots. The snapshot method facilitates the computation of the two-point autocovariance from a relatively small number ($N < M$) of instantaneous realizations or snapshots where M is the number of grid points. The methodology consists of the following steps. First, all the fluctuating velocity components from the N realizations are arranged in a matrix U as

$$U = \left[U^1\ U^2 \cdots U^N\right] = \begin{bmatrix} u_1^1 & u_1^2 & \cdots & u_1^N \\ \vdots & \vdots & \vdots & \vdots \\ u_M^1 & u_M^2 & \cdots & u_M^N \\ v_1^1 & v_1^2 & \cdots & v_1^N \\ \vdots & \vdots & \vdots & \vdots \\ v_M^1 & v_M^2 & \cdots & v_M^N \end{bmatrix} \tag{2.23}$$

The cross-covariance matrix is then calculated as (Sirovich 1987):

$$C = \tfrac{1}{N}(U^T U) \tag{2.24}$$

which is symmetric and positive definite. The corresponding eigenvalue problem is

$$CV^n = \lambda^n V^n \tag{2.25}$$

The eigenvectors V^n are arranged according to the size of the eigenvalues

$$\lambda^1 > \lambda^2 > \cdots > \lambda^N \geq 0 \tag{2.26}$$

where each eigenvalue represents the amount of the total variance explained by a given POD mode. From the eigenvectors, the eigenfunctions or modes, Φ^n, are constructed as

$$\Phi^n = \frac{\sum_{i=1}^{N} V_i^n U^i}{\left\| \sum_{i=1}^{N} V_i^n U^i \right\|}, \qquad n = 1, 2, ..., N \tag{2.27}$$

where V_i^n is the ith component of the eigenvector corresponding to eigenvalue λ^n, and the L_2-norm for a vector **x** is given by

$$\|\mathbf{x}\| = \sqrt{x_1^2 + x_2^2 + \cdots + x_M^2} \tag{2.28}$$

Writing the matrix of POD eigenmodes as $M = \left[\Phi^1\ \Phi^2 \cdots \Phi^N\right]$, the temporal coefficients $a_n(t)$ are determined by projecting the fluctuating field onto the eigenmodes as

$$a^n = M^T U^n \tag{2.29}$$

which because of the orthogonality of the eigenfunctions are uncorrelated in time with mean square values equal to the eigenvalues λ^n,

$$\overline{a_n(t)a_m(t)} = \delta_{nm}\lambda^n \tag{2.30}$$

Using equation 2.19, the fluctuating part of the *n*th snapshot can be reconstructed as (Sirovich 1991):

$$U^n = \sum_{n=1}^{N} a_n(t)\Phi^n \tag{2.31}$$

Since the POD is performed on the fluctuating velocity fields, the *n*th eigenvalue, λ^n, represents the turbulent kinetic energy (tke) contribution of the *n*th POD mode, Φ^n, with Mode 1 contributing the most energy, followed by Mode 2, and so on. The fractional contribution of mode Φ^n to the total tke is given by (Sen et al. 2007):

$$e_n = \frac{\lambda^n}{\sum_{i=1}^{N}\lambda^i} \tag{2.32}$$

Lower-order modes are representative of the large-scale coherent structures of the flow while higher-order modes correspond to the small-scale and less energetic turbulent structures. The cumulative energy contained in modes 1 to *m* is given by

$$E_m = \sum_{i=1}^{m} e_i \tag{2.33}$$

It must be noted that because the lower-order modes contribute much more energy than the higher-order ones, only the first few modes may be necessary to reconstruct the essential features of the flow. Using equation 2.31, a low-order representation of an instantaneous flow field based on the first *m* (< *N*) leading modes can be reconstructed as

$$U_L^n = \sum_{n=1}^{m} a_n \Phi^n \tag{2.34}$$

The accompanying residual field composed of the motions from the discarded higher-order modes is then calculated as

$$U_R^n = U^n - \sum_{n=1}^{m} a_n \Phi^n \tag{2.35}$$

2.2.1.5 Discrete Wavelet Transform (DWT) Analysis of the Velocity Fields

The wavelet transform is a mathematical tool that is used to decompose a spatial signal into contributions from both space and scale. The wavelet transform is formed as an inner product of the signal with a scaled and translated analyzing wavelet that satisfies both the admissibility and regularity conditions. Admissibility implies that the wavelet is a square integrable function with zero mean, while regularity implies that it is compactly supported (non-zero valued over a finite interval) and has a sufficient number of vanishing moments. The technique is well suited for detecting and revealing the presence of singularities in signals. For example, if the signal is locally smooth, the transform will result in small wavelet coefficients, and if the signal contains a singularity at a given point such as a sudden spike, then in the vicinity of the singularity the amplitude of the wavelet coefficients will be large. A detailed review of wavelet transforms and their applications in turbulence can be found in Farge (1992), while the mathematical theory of discrete wavelet transforms can be found in Daubechies (1988) and Mallat (1989).

To reveal the coherent structures, each instantaneous velocity fluctuation field was decomposed into an orthogonal wavelet series as follows. First, an orthogonal

wavelet basis function $\psi(x) \in L^2(R)$, called the "mother wavelet" is selected, which is used to generate the required translates and dilates given by

$$\psi_{mn}(x) = 2^{-m/2}\psi\left(2^{-m}x - n\right), \tag{2.36}$$

where *m* and *n* are integers, representing scale and position (space), respectively. Using the multiresolution approach (Daubechies 1988; Mallat 1989), a second function $\phi(x) \in L^2(R)$, called the scaling function or "father wavelet" is selected, which is used to provide successive approximations to the signal at different scales:

$$\phi_{mn}(x) = 2^{-m/2}\phi\left(2^{-m}x - n\right), \tag{2.37}$$

To ensure orthogonality, the functions are sampled over a dyadic grid, whereby the scale (*m*) axis is discretized by octaves, while the space (*n*) axis is discretized by integer translations whose size varies with the scale. Thus, for a function of support, *L*, sampled at $N = 2^M$ points, the total number of octaves is *M* and the number of wavelet coefficients at each scale, *m*, is 2^{M-m}. Since the PIV velocity fields were sampled over a two-dimensional grid, 2D versions of scaling function $\phi(x)$ and wavelets $\psi(x)$ are required. Following Farge (1992), the 2D scaling and wavelet functions are formed from a tensor product of the one-dimensional functions as

$$\phi(x, y) = \phi(x)\phi(y)$$

$$\psi^{(1)}(x, y) = \phi(x)\psi(y)$$

$$\psi^{(2)}(x, y) = \psi(x)\phi(y)$$

$$\psi^{(3)}(x, y) = \psi(x)\psi(y)$$

The 2D velocity field $f(x, y)$, where $f = u$ or v is projected onto the wavelet basis as (Rupert-Felsot et al. 2009)

$$f(x,y) = \phi_{M,M,M}\,\overline{f}_{M,M,M} + \sum_{m=1}^{M}\sum_{p=1}^{3}\sum_{n_x,n_y=1}^{2^{M-m}} \widetilde{f}^{(p)}_{m,n_x,n_y}\psi^{(p)}_{m,n_x,n_y}\,, \qquad (2.38)$$

where $\overline{f}_{M,M,M}$ is the scaling coefficient at the largest scale, $\widetilde{f}^{(p)}_{m,n_x,n_y}$ represents the wavelet coefficients given by

$$\widetilde{f}^{(p)}_{m,n_x,n_y} = \left(f(x,y),\psi^{(p)}_{m,n_x,n_y}\right), \qquad (2.39)$$

and $(.,.)$ is the L^2 inner product. The wavelet coefficients are often calculated using the Mallat's (1989) pyramidal algorithm.

Thus, by identifying the wavelet coefficients contributing to the coherent motions, usually done by comparing coefficient magnitudes to a selected threshold (Rupert-Felsot et al. 2009), it is possible to reconstruct the coherent part of the flow field.

2.3 Summary of Previous Wall-Bounded Particle-Laden Flows

2.3.1 Introductory Remarks

As of today, there exists a large number of experimental and numerical studies devoted to the subject of uniformly loaded particle-laden turbulent flows. The special case of single particles moving in a fluid is usually examined in order to develop correlations for the drag coefficient. Empirical correlations for calculating the drag coefficient for a spherical particle immersed in a fluid are summarized by Clift et al. (1978) for a wide range of particle Reynolds numbers, and the relative importance of the various force terms in the particle momentum equation is detailed clearly in the works of (Maxey and Riley 1983; Elghobashi and Truesdell 1992; Armenio and Fiorotto 2001).

For the majority of investigations, the main area of attention is the characterization of the interactions between particles and turbulence in order to address questions concerning how particles respond to turbulence and the effects of feedback between the interacting phases. Studies conducted by Elghobashi (1994) suggest that both particles behaviour and their influence on turbulence can be predicted from a knowledge of the particle Stokes number (St) and the volume fraction (ϕ_v). Based on these two parameters, Elghobashi (1994) suggested that there are three main ways in which particles and turbulence can interact, namely, one-way, two-way or four-way coupling, corresponding roughly to dilute, moderate and densely loaded suspensions, respectively. In one-way coupling, which corresponds to volume fractions $\phi_v < 10^{-6}$, particle motion is governed entirely by fluid turbulence but the particles themselves do not exert any perceptible influence on turbulence, irrespective of the Stokes number. The interaction is described as two-way coupling when both particles and the carrier fluid mutually modify the turbulence field of one another. This corresponds to volume fractions of $10^{-6} < \phi_v < 10^{-3}$, where the particle number density is large enough to generate appreciable feedback force to alter the carrier-phase turbulence. In this case, particles will enhance turbulence when the Stokes number (St_e), based on the time scale of the large eddies is greater than 1 and attenuate turbulence when the Stokes number is less than 1. In four-way coupling ($\phi_v > 10^{-3}$), however, interparticle distances are so short that particle-particle interactions such as inter-particle collisions become the dominant interaction mechanism, introducing additional effects alongside particle-fluid feedback, that must be accounted for. Table 2.1 summarizes some of the previous investigations conducted in wall-bounded particle-laden turbulent flows for a wide range of flow parameters.

Table 2.1: Summary of previous wall-bounded particle-laden turbulent flows.

Reference	Flow Configuration	Technique	Carrier Phase	Particles			Fluid Velocity (m/s)	Reynolds Number (Re)	Surface Condition	Particle Loading (ϕ_m or ϕ_v)
				Type	Density (kg/m^3)	Diameter (μm)				
Rashidi et al. (1990)	Open Channel	Flow Visualization	Water	Polystyrene Glass Lycopodium	1030 2505 700	120 – 1100 88 28	0.0077-0.24	$2500 \leq Re_h \leq 7500$	Smooth	$0.009\% \leq \phi_v \leq 0.036\%$
Pedinotti et al. (1992)	Open Channel	DNS	Water	Solid Particles	1030	120 - 1100		$Re_\tau = 106$	Smooth	$0.009\% \leq \phi_v \leq 0.036\%$
Brooke et al. (1992)	Fully Developed Channel[V]	DNS	Air	Aerosol	$\rho_p/\rho_f = 1000$	13.8 – 23.8		$Re_D = 9040$	Smooth	
Tsuji et al. (1984)	Vertical Pipe (upward flow)	LDV	Air	Polyethylene Polystyrene	970 1030	3430 243 - 2780	8 - 20	$16000 \leq Re_D \leq 33000$	Smooth	$\phi_m \leq 500\%$
Kulick et al. (1994)	Wind Tunnel[V] (downflow)	LDA	Air	Glass Copper	2500 8800	50, 90 70	10.5	$Re_h = 13800$	Smooth	$2\% \leq \phi_m \leq 80\%$
Rogers & Eaton (1991)	Wind Tunnel[V] (upward flow)	LDA	Air	Copper	8800	70	8.0 8.2	$Re_\theta = 1090$ 1410	Smooth	$\phi_m = 20\%$
Elghobashie & Truesdell (1993)	Fully Developed Channel[H]	DNS	Air	Solid Particles	$455 \leq \rho_p/\rho_f \leq 3636$	500, 750 1000		$0.18 \leq Re_p \leq 0.45$	Smooth	$0\% \leq \phi_m \leq 0.05\%$
Wu et al. (2006)	Fully Developed Channel[H]	PIV	Air	Polythene beads	1030	60, 110	8.86	$Re_h = 6826$	Smooth	$0\% \leq \phi_m \leq 2.6\%$
Kaftori et al. 1995 & 1998	Open Channel[H]	2D LDA & Flow Visualization	Water (0.65μm TiO_2)	Polystyrene	1050	100 – 900	0.125 – 0.322	$3660 \leq Re_h \leq 14340$	Smooth	$0.006\% \leq \phi_v \leq 0.023\%$
Fessler et al. (1994)	Fully Developed Channel[V]	Visualization with digital photography	Air	Lycopodium Glass Copper	700 2500 8800	28 25, 50, 90 70	10.5	$Re_h = 13800$	Smooth	$3\% \leq \phi_m \leq 100\%$

Table 2.1 continued: Summary of previous wall-bounded particle-laden turbulent flows.

Reference	Flow Configuration	Technique	Carrier Phase	Particles			Fluid Velocity (m/s)	Reynolds Number (Re)	Surface Condition	Particle Loading (φ_m or φ_v)
				Type	Density (kg/m^3)	Diameter (μm)				
Wang and Squires (1996)	Fully Developed Channel[V]	LES	Air	Lycopodium Glass Copper	700 2500 8800	7, 14, 28 25, 50, 90 70	10.5	Re_τ = 180 & 644	Smooth	2% ≤ ϕ_m ≤ 80%
Best et al. (1997)	Open Channel	PDA	Water	Glass	2600	220	0.58	39190 ≤ Re_h ≤ 39970	Smooth	ϕ_v ≤ 0.025 %
Kiger and Pan (2002)	Fully Developed Channel[H]	PIV	Water	Glass	2600	200	0.595	Re_τ = 570	Smooth	ϕ_v = 0.02 %
Kussin & Sommerfeld (2002)	Fully Developed Channel[H]	PDA	Air	Glass	2500	60 – 1000	10 – 25	30805 ≤ Re_h ≤ 57284	Smooth & Rough (Steel plates)	ϕ_m ≤ 200%
Nezu & Azuma (2004)	Open Channel	PTV	Water	Polystyrene	1050 1150	300 – 1300	0.246 – 0.281	12300 ≤ Re_h ≤ 25000	Smooth	0.03% ≤ ϕ_v ≤ 0.32 %
Righetti & Romano (2004)	Open Channel	PDA	Water	Glass	2500	100, 200	0.63	Re_h = 15000	Smooth	ϕ_v = 0.3 %
Benson et al. (2005)	Fully Developed Channel[V]	LDA	Air	Glass	2500	150	10.5	Re_h = 13800	Smooth & Rough (Wire mesh)	ϕ_m = 15%
Vreman (2007)	Fully Developed Pipe[V]	DNS	Air	Glass	2470	60, 90	4.0	Re_τ = 140	Smooth	0.0053% ≤ ϕ_v ≤ 1.48%
Yamamoto & Okawa (2010)	Fully Developed Pipe[V]	LES	Air	Water droplets	400	50, 100		Re_τ = 500 & 1000	Smooth	

[H]Horizontal channel
[V]Vertical channel

2.3.2 Studies over Smooth Walls

Gore and Crowe (1989) reviewed some of the early experimental literature on turbulent shear flows with volume fractions ranging from 2.5×10^{-6} to 2.0×10^{-1} and density ratios ranging from 0.001 to 7500 and found that whether particles increase or decrease turbulence is dependent on the value of the ratio of the particle diameter to the length scale of the energy containing eddies (d_p/L_e). The authors found that in general, when the value of d_p/L_e is less than 0.1, particles attenuate turbulence, and when the value of d_p/L_e is greater than 0.1, they augment turbulence. It was argued that when the particles are small compared to the turbulent length scale, they tend to follow the turbulent fluid motions and in doing so absorb energy from them thus reducing the turbulent energy. On the other hand, large particles will tend to create turbulence in their wakes at the scale of the energy containing eddies, which will lead to turbulence augmentation. Other early efforts that attempted to correlate turbulence modification with particle characteristics include Hinze (1972), Hetsroni (1989), Yuan and Michaelides (1992), and Kenning and Crowe (1997). Hinze (1972) remarked that particles always act as a sink to the surrounding fluid and suggested that the presence of particles lead to fractional reduction in the carrier fluid turbulence kinetic energy of the form $k/k_o = (1 + \phi_v \rho_p/\rho_f)^{-1}$, where k and k_o are the turbulence kinetic energies of the laden and unladen flows, respectively. Hetsroni (1989) reported that particles with Reynolds number $Re_p > 400$ exhibit considerable vortex shedding and therefore increase the carrier fluid turbulence. Yuan and Michaelides (1992) and Kenning and Crowe (1997) analyzed the interaction between a single rigid sphere and the carrier fluid eddies and suggested that the overall change in the fluid turbulence kinetic energy is a non-linear function of the particle relative

velocity, Reynolds number, Stokes number and density ratio. In the remainder of this section, the main results from a number of previous boundary layer and fully developed channel investigations over smooth walls are highlighted.

Rashidi et al. (1990) used flow visualization and image processing techniques to study particle turbulence interactions in a low Reynolds number open channel boundary layer. Two types of particles were used, namely, glass spheres of mean diameter 88 μm and polystyrene particles of mean diameter $120 \leq d_p \leq 1100$ μm. It was found that large particles increased the carrier fluid turbulence by increasing the number of wall ejections, while smaller particles reduced the carrier fluid turbulence by decreasing the number of wall ejections. The results also indicated that the degree of turbulence enhancement or augmentation is an increasing function of particle loading. Rogers and Eaton (1991) employed LDA to investigate turbulence modification by 70 μm copper particles in a vertically oriented wind tunnel and found that the solid particles reduced the peak value of the streamwise turbulence intensity in the inner layer but increased the turbulence intensity values in the outer layer. A comparison of the power spectra of the streamwise velocity fluctuation showed that particles dampened the fluid turbulence at large scales but enhanced the fluid turbulence at small scales. Kaftori et al. (1998) also used LDA to explore the effects of neutrally buoyant polystyrene particles on turbulence in a horizontal water channel and observed that particles sedimented at the wall at a rate that increased with decreasing bulk flow Reynolds number. The presence of particles at the wall led to a decrease in the carrier-fluid streamwise mean velocity and an increase in the wall shear stress. Particles did not affect the turbulent intensities and Reynolds shear stress substantially in the outer layer except near the wall where significantly enhanced

values were observed for all particle sizes. Best et al. (1997) used PDA to measure the flow statistics for the turbulent boundary layer in a horizontal water channel laden with 220 μm glass particles. It was found that a substantial fraction of the particles was transported over the wall as bed load producing a roughness effect which reduced the mean velocity and increased the skin friction. The authors also found that particles increased the turbulent intensities near the wall and reduced them in the outer layer but the effect was more dramatic on the wall-normal turbulent intensity than the streamwise turbulent intensity. Hagiwara et al. (2002) reported a horizontal water channel flow laden with 50 μm copper particles ($\rho_p/\rho_f = 8.3$). A PTV technique was used to measure the fluid velocity while PIV was used to measure the velocity of the copper particles. The results showed an increase in the fluid mean velocity in the near wall region but a reduction in the core region. It was also found that the particles attenuated the streamwise and wall-normal turbulent intensity levels near the wall but caused no significant modifications in the outer layer. The particle effects on the mean velocity and turbulent intensities were attributed to the gravitational settling of particle clusters towards the lower wall. Righetti and Romano (2004) used PDA to investigate the effects of 100 μm and 200 μm glass particles on the turbulent boundary layer in a horizontal water channel. The authors reported an increase in the laden fluid streamwise mean velocity near the wall but no significant modification in the outer layer. It was noticed that particles enhanced the values of the turbulent intensities and Reynolds shear stress near the wall but attenuated them in the outer layer with greater effects in the presence of the 200 μm particles compared to the 100 μm particles. In agreement with previous studies, the particles were found to also modify the wall-normal turbulent intensity more strongly than the

streamwise turbulent intensity. It was argued that turbulence augmentation near the wall is attributable to more energetic bursting events in the inner layer, while turbulence attenuation in the outer layer is attributable to the vertical momentum expended by ejections in overcoming gravity and lift up of particles. The results also suggest a strong connection between turbulence modulation and variation of the particle Stokes number across the boundary layer. For instance, it was found that particles increase the carrier fluid turbulence near the wall where their Stokes number is larger but decrease the carrier fluid turbulence in the outer layer where their Stokes number is smaller. Noguchi and Nezu (2009) presented boundary layer data acquired using PIV for the fluid phase (water) and PTV for polymer particles (ρ_p/ρ_f = 1.2 and 1.5) with diameter ranging from 250 μm to 1000 μm. The results show that turbulence augmentation and suppression do not only increase with increasing particle concentration but also increase with increasing particle-to-fluid density ratio. More recently, Kidanemariam et al. (2013) conducted a DNS investigation of a horizontal open channel flow laden with spherical particles. The particle relative diameter and density ratio were, respectively, $d_p/L_e \approx 0.18$ and $\rho_p/\rho_f \approx 1.7$, and the volume fraction was set to about $\phi_v = 0.05\%$. Because of gravitational settling effects, particles were found to form a strong wall-normal concentration gradient near the wall. No significant modifications were found in the fluid mean velocities, turbulence intensities, and Reynolds shear stress when compared to the unladen flow, but the particles were found to increase the extents of the fluid two-point correlations. The increase in size of the two-point correlations was attributed to the stabilizing effect of particles on the near-wall structures.

Studies in fully developed channels are comprised of measurements in both

horizontally and vertically (upward or downward) oriented channels. Tsuji and Morikawa (1982) applied LDA and Pitot tube to characterize particle-turbulence interactions for air laden with 200 μm and 3.4 mm plastic pellets ($\rho_p/\rho_f \approx 1$) in a horizontal pipe. The results showed a reduction of the fluid streamwise mean velocity near the wall and an increase in the outer layer for both particle sizes with more dramatic effects at larger mass loadings. The 200 μm particles caused a reduction in the turbulence level throughout the entire pipe cross section, while the large particles enhanced the turbulence level in comparison with the particle-free flow. These effects occurred more rapidly with increasing mass loading ratio. Additional experiments conducted by Tsuji et al. (1984) in a vertical pipe with plastic particles of diameter 0.2 mm $\leq d_p \leq$ 3 mm indicated that while large particles increased the air turbulence and smaller particles decreased the air turbulence, particles of intermediate size caused turbulence promotion at the pipe centre and a reduction at the wall. Frequency spectral measurements showed that large particles have no impact on the carrier fluid turbulence spectra, whereas small particles attenuated energy at the large scales and enhanced the spectral density of the dissipative scales. Kulick et al. (1994) conducted an LDA investigation of a downward fully developed channel flow of air laden with 50 μm and 90 μm glass particles and 70 μm copper particles. The streamwise mean velocity of the laden fluid was unchanged by the particles, but the fluid turbulence was attenuated in the presence of particles with stronger effects in the wall-normal turbulent intensity than the streamwise turbulent intensity. The level of turbulence attenuation was observed to increase with particle Stokes number, mass loading and distance from the wall. Kiger and Pan (2002) reported experimental data that examined turbulence modification in a horizontal water channel flow laden with 195 μm glass particles. A PIV

was used to measure both the carrier fluid and particulate phase velocities. Particles reduced the fluid streamwise mean velocity and increased the friction velocity. These effects were found to be accompanied by a decrease in the peak value of the laden fluid streamwise turbulent intensity, an increase in the streamwise turbulent intensity values over the rest of the flow region, and enhanced levels of the wall-normal turbulent intensity and Reynolds shear stress in the outer region. Shao et al (2012) employed DNS to perform a fully resolved simulation of horizontal channel flow laden with large particles ($d_p/L_e \approx 0.23$ and 0.45). The influence of the particles on the turbulence statistics and structures were investigated for different volume fractions ($0.79\% \leq \phi_v \leq 7.08\%$) and settling velocity ratios ($0.05 \leq V_s/U_{max} \leq 0.5$). At negligible settling velocity ratios, particles attenuated the streamwise turbulence intensity but enhanced the transverse turbulence intensities. At substantially high settling velocity ratios, most particles deposited at the wall to form a sediment layer whose roughness acted to increase all the turbulence intensities.

Some of the above studies also presented results on particles velocity response to turbulence. Some studies (e.g., Tsuji and Morikawa 1982; Rashidi et al. 1990; Best et al. 1997; Kiger and Pan 2002, Shao et al. 2012; Kidanemariam et al. 2013), for instance, found that the particle streamwise mean velocity lags the fluid streamwise mean velocity, while others (Kulick et al. 1994; Righetti and Romano 2004; Vreman 2007) found the particles to travel faster than the fluid in the near-wall region and slower than the fluid in the outer region. The results in the literature regarding particle velocity fluctuation intensities are relatively more inconsistent. Particles have been reported to have larger streamwise velocity fluctuation but smaller wall-normal velocity fluctuation intensity

compared to the corresponding unladen fluid turbulent intensities (Kulick et al. 1994), both larger streamwise and wall-normal velocity fluctuation intensities compared to corresponding fluid turbulent intensities (Wu et al. 2006; Vreman 2007), or streamwise velocity fluctuation intensity of the same order as the fluid turbulent intensity but larger values of the particle wall-normal fluctuation intensity compared to the fluid (Kaftori et al. 1995b; Best et al. 1997).

Where large particle volume fractions are involved (four-way coupling), the literature reports that inter-particle collisions can significantly alter the particle turbulence field which can in turn modify the carrier fluid turbulence intensities. Inter-particle collisions have also been implicated in the re-isotropization of the particles velocity fluctuation field. Tanaka and Tsuji (1991) observed this effect in their study and attributed it to the redistribution of particle momentum from the streamwise velocity fluctuation component to the transverse components. The return-to-isotropy effect has also been found to lead to the enhancement of particle dispersion in the transverse directions (e.g., Tsuji et al. 1987; Sommerfeld 1995). Yamamoto et al (2001) computed downward gas-solid flow in a vertical channel and found that inter-particle collisions made the particle concentration profile much flatter. A similar observation was made by Saffar-Avval (2007) who noted in addition that inter-particle collisions suppressed the fluid turbulence intensities in the outer layer in a manner that increased with increasing mass loading ratio.

2.3.3 Studies over Rough Walls

In spite of the large volume of information available on smooth-wall particle-laden

turbulent flows, roughness effects on particle-turbulence interactions have been studied far less. Results presented by Abbott and Francis (1977) suggest that particles motion close to a rough wall is quite similar in character to that over a smooth wall. Sumner and Deigaard (1981) reported similar findings for a gravel roughness ($k_s^+ = 81$), noting that even though particle lift-up by bursting processes could be more intense over a rough wall than a smooth wall, there is no significant variation in the flow statistics between the two surface conditions. Nino and Garcia (1996) presented results of detailed experiments over a transitionally rough sand-grain surface ($k_s^+ \approx 17$) and found that roughness elements disrupt the structure of the viscous sublayer and produce wall streaks which are less coherent, persistent and with shorter spatial extent. By measuring the instantaneous particle velocities during ejections in both smooth and rough-wall flows, it was observed that the streamwise component tends to be much lower than the local mean flow velocity, while the wall-normal component tends to be very intense indicating that such particles are responding to rather extreme quadrant 2 events.

In the case of densely loaded flows, roughness effects have been noticed to lead to an increase in particle-wall collisions. Tsuji et al. (1987), for example, found that wall roughness considerably increased the wall collision frequency for large particles. Sommerfeld and Huber (1999) reported an increase in particle rebound behaviour due to roughness effects in a horizontal channel flow. Kussin and Sommerfeld (2002) obtained measurements of gas-solid flow in a channel with various wall roughness conditions and found that wall roughness enhanced the particle turbulence intensities due to the irregular bouncing of particles with the wall. Sommerfeld (2003) investigated roughness effects on inter-particle collisions in a horizontal channel flow and found that wall roughness

reduces the wall collision frequency for small particles and increases it for larger particles. For each particle size, the effects were found to increase with mass loading. However, even though the redistribution of the particle streamwise turbulence intensities to the wall-normal turbulence intensity by inter-particle collisions was observed for the rough wall, the effect was found to be less dramatic compared to that over the smooth surface. Benson et al. (2005) conducted measurements over a wire mesh roughness ($k_s^+ \approx$ 118) and found that mesh roughness decreased the particle mean velocity across the entire boundary layer in comparison to values over a smooth wall. Over the rough wall, particle velocities were much lower than the fluid velocity in the outer layer but slightly larger close to the wall. It was also found that the mesh roughness increased the particle turbulence intensities more significantly than it increased the fluid turbulence intensities. The larger particle turbulence intensities were attributed to particle-wall collisions. Breuer et al. (2012) proposed a sand grain roughness model for the numerical computation of roughness effects on particles. Alletto and Breuer (2013) applied an LES method incorporating the sandgrain roughness model of Breuer et al. (2012) to investigate the interaction between 50 μm polydisperse particles and 134 μm monodisperse particles in the presence of a rough wall ($k_s^+ \approx 1.84$). The particle-to-fluid density ratio of both types of particles was 2083 and the volume fraction was varied from 0.014% to 0.048%. The results indicated that more frequent particle-wall collisions over the rough wall and subsequent rebound from the rough wall induced secondary flow of the second kind (i.e., secondary flow due to anisotropy of the Reynolds stresses) whose intensity decreased with increasing particle size.

2.3.4 Particle Deposition Studies

The deposition of particles over surfaces has also received significant research attention within the multiphase flow community due to its numerous practical applications. In some applications, it is used to an intended advantage such as drug delivery by inhalation, dust collection, and air pollution control using electrostatic precipitators. In other applications, nonetheless, its occurrence can lead to undesirable effects such as scouring of pipe walls, particle losses in aerosol sampling lines, and settling of particles over the surfaces of sensitive electronic appliances.

All particle deposition studies considered in the past can be classified into two main categories. In one group of studies, particles were allowed to be deposited out of the flow but the particle loading ratio was continuously adjusted to keep the particle concentration constant (e.g., Mito and Hanratty 2005; Yang and Shy 2005; Yamamoto and Okawa 2010). This made it possible to examine not only particle deposition characteristics (deposition velocity and deposition coefficient), but also calculate statistical properties by ensemble averaging. In the second group of studies, particles were allowed to be deposited but no adjustments were made to keep the particle concentration constant (e.g., Brooke et al. 1992; Li and Ahmadi 1993; Lai et al. 2001; Dritselis 2009). Because of the particle concentration variation in these cases, only instantaneous quantities were presented.

For particle deposition over smooth walls, studies indicate that the deposition velocity is a monotonic function of the particle Stokes number and the particle relative diameter. Thus, both heavy and large particles will deposit more rapidly than light and small particles, respectively. Brooke et al. (1992) in their DNS obtained results that

showed that for a given particle Stokes number, the probability density function of the Eulerian fluid velocity when integrated at the location of free flight, can be used to approximate the flux of depositing particles at the wall. Yamamoto and Okawa (2010) investigated the effects of particle concentration and carrier fluid turbulence on the particle deposition coefficient and found that the deposition coefficient is enhanced when the particle concentration is increased but is decreased when the fluid turbulence intensity is increased.

In the presence of wall roughness, particles have been found both to deposit more rapidly (e.g., El-Shobokshy 1983; Li and Ahmadi 1993; Lai et al. 2001), and more slowly (e.g., Sommerfeld and Huber 1999; Alletto and Breuer 2013) compared to a smooth wall. El-Shobokshy (1983) who employed flow rate and pressure measurements in vertically oriented smooth and rough pipes ($k_s^+ \approx 0.56$ and 1.65) considered the effects of roughness on the deposition rate of aerosol particles ($\rho_p/\rho_f \approx 1250$) with mean diameters ranging from 1 μm to 6.2 μm. Roughness was found to cause about an order of magnitude increase in the deposition velocity compared to corresponding values over the smooth wall. Li and Ahmadi (1993) performed a computer simulation of aerosol particles ($\rho_p/\rho_f \approx$ 2000) in vertical and horizontal channels with rough walls ($k_s^+ \approx 0.2$, 0.82, 2.12). The simulations, which were based on experimentally determined velocity distributions, considered particles of mean diameter 0.01 μm $\leq d_p \leq$ 10 μm. The results showed that the particles deposition velocity was enhanced by about two orders of magnitude relative to the smooth wall. Additionally, the effects were observed to be more dramatic in the horizontal channel than the vertical channel, due to the influence of gravitational settling. Lai et al. (2001) suggested that the increase in deposition rate with roughness can be

attributed to the absence of a viscous sublayer on the rough surface, which for a smooth surface can generate lift to inhibit particle deposition at the wall.

2.3.5 Influence of Coherent Structures on Particles

In particle-laden turbulent flows, coherent structures are regarded to play a key role in the transport of particles. In near-wall turbulent flows, particles have been observed to accumulate in wall ejections to form clusters called particle streaks. It has been found that depending on their inertia (Stokes number), particles can be entrained by the quasi-streamwise vortices or flung out of the vortices to low-vorticity regions in the flow (Kaftori et al. 1995a). It has been observed, for instance, that lighter particles tend to follow the motion of vortices and thus remain in suspension, whereas heavier particles tend to follow different paths because of their higher inertia. Particle deposition on surfaces is attributed to the presence of coherent structures. It has been suggested, for instance, that particles are deposited when they are brought to the wall by sweep-like motions (Cleaver and Yates 1975). Brooke et al. (1992) also proposed a particle deposition mechanism in which particles undergo a prolonged lateral wandering motion in the wall-normal direction until they are trapped in the quasi-streamwise vortex and brought directly to the wall. Other near-wall studies that reported the effects of coherent structures on particles include Squires and Eaton (1990), Pedinnoti et al. (1992), Fessler et al. 1994, and Marchioli and Soldati (2007). Squires and Eaton (1990) used DNS to study the effects of forced isotropic turbulence on the spatial distribution of light and heavy particles ($0.075 \leq St_e \leq 1.50$). It was found that both light and heavy particles collect preferentially in regions of low vorticity and high strain rate, leading to substantial

modifications of the fluid turbulence characteristics. Increasing the particle mass loading ratio ($0.1 \leq \phi_m \leq 1.0$) was found to inhibit and magnify, respectively, the preferential concentration effect for the light and heavy particles. Pedinnoti et al. (1992) found that the particles collect in low-speed streaks after having been ejected from the wall by the quasi-streamwise vortices, and that, small particles increased the average time between wall ejections while large particles decreased it. Fessler et al. (1994) found the spatial distributions of heavy particles in turbulent channel flow to be non-uniform due to their segregation in low vorticity regions. It was suggested that particle preferential concentration is predominantly controlled by the particle Stokes number, with maximum preferential concentration occurring around $St \approx 1$. Marchioli and Soldati (2007), who conducted a DNS study of ZPG turbulent boundary layers, found that particle preferential concentration is largest for particles with wall Stokes number of about $\tau_p^+ = 25$. Outside this value, a decrease in preferential concentration was observed. Ferry and Balachandar (2001) demonstrated that particles collect in regions of low swirling strength and high compressional strain rate, and posited that statistics such as the swirling strength and maximum compressional strain rate are better indicators of particle preferential concentration than vorticity magnitude.

2.4 Summary

From the literature survey, it can be concluded that turbulence in channels and boundary layers can be divided into two main regions, the inner and outer regions, each of which has distinct scaling properties. When the flow is subjected to wall roughness, the effect of roughness is to reduce the mean velocity, enhance the turbulence intensities and Reynolds

stresses, and disrupt the turbulence structure. The turbulence structure is envisaged as a conglomeration of certain coherent eddies that are primarily responsible for the generation and sustenance of turbulence. Previous single-phase studies have applied a number of structure identification techniques to extract the coherent structures in turbulence. These include both single-point techniques such as quadrant decomposition, wavelet decomposition, use of the vorticity and swirling strength, and multi-point techniques such as two-point correlations, linear stochastic estimation and proper orthogonal decomposition.

Previous particle-laden turbulence investigations have been conducted predominantly over smooth walls, and under conditions where the particle loading ratio was kept relatively constant. These include both experimental and computational studies in ZPG turbulent boundary layers, and in either vertically or horizontally oriented fully developed channels. From these works, it can be concluded that large particles cause turbulence augmentation (due to vortex shedding), while small particles cause turbulence attenuation by acting as additional sources of fluid turbulent kinetic energy dissipation. These modification effects were found to be more dramatic with increasing particle loading ratio. Some investigations reported particles to move slower than the fluid while others reported particles to move faster than the fluid in the wall region but slower in the outer region. At dense loading ratios, four-way coupling is observed where inter-particle collisions become the dominant particle-turbulence interaction mechanism responsible for turbulence modification. Inter-particle collisions have been found to cause a redistribution of the particle momentum between the particle velocity fluctuations accompanied by flattening of the particle concentration profile. Despite the large volume

of investigations over smooth walls, however, the available number of rough wall particle-laden turbulent flows is limited. Wall roughness has been identified to increase the frequency of particle-wall collisions, and enhance the particle turbulence intensities by altering the particles rebound behaviour. For particles depositing over rough walls, no general consensus exists regarding the influence of roughness on the deposition rate. Some studies, for instance, observed particles to deposit more slowly over rough walls compared to smooth walls, while others found to the contrary, particles depositing more rapidly in the presence of a rough wall.

Although the interaction between particles and the coherent structures (known to be responsible for particle transport) was considered in some studies, the observations were limited only to the particles' response to these structures. The particles, for instance, were found to be transported towards the wall by high-speed inward moving sweeps, or lifted up towards the outer layer by wall ejections. Depending on their Stokes number, particles were also noticed to accumulate preferentially in low-vorticity regions of the flow to form particle streaks (or clusters). This preferential accumulation has been identified to be responsible for additional modification effects on the carrier-fluid turbulence. Nevertheless, there are still many open questions concerning the exact impact of particles on turbulence. The effects of gravitational settling of particles on the vortical structures in wall turbulence have not been thoroughly examined, and to-date, only relatively few investigations have considered the impact of particles on multi-point statistics such as two-point correlations, known to share a statistical correspondence with the coherent structures. Another area where knowledge is incomplete is the impact of particles on the coherent structures over a rough wall. Understanding the spatial

characteristics of particle-laden turbulent flows subjected to wall roughness will be invariably beneficial to development of corresponding turbulence models.

CHAPTER 3

EXPERIMENTAL SETUP AND MEASUREMENT TECHNIQUE

This chapter presents details of the experimental setup used. These include a description of the test section, a summary of the solid phase characteristics and the measurement conditions investigated. An outline of the principles of particle image velocimetry (PIV) for single-phase flow measurements is given. This is intended to provide the preambles to the adaptation of the approach to two-phase flows.

3.1 Description of the Test Section

The experiments were conducted in horizontal rectangular channels as shown schematically in figure 3.1. The channels were fabricated from 6 mm thick acrylic test plates and have interior dimensions of approximately 2500 mm × 186 mm × 40 mm. Three different channels were fabricated for the experiments. One channel was used for the smooth wall experiments, while the remaining two channels were built to different internal heights in order to accommodate the wall roughness. The wall roughness include closely packed sand grains of nominal mean diameter, 1.5 mm ($k/h \approx 0.08$) and gravel of nominal mean diameter, 5 mm ($k/h \approx 0.25$), which were glued to 4.5 mm acrylic inserts. The inserts were screwed to the bottom wall of the channels to create an asymmetric roughness condition. For all channels, the aspect ratio, $b/(2h)$, was approximately 5:1, where b is the channel width. The channels were screwed to the bottom wall of a main water tunnel of length 2500 mm and cross section dimensions 200 mm × 200 mm. A detailed description of the tunnel facility is available in Tay (2009). The flow in the

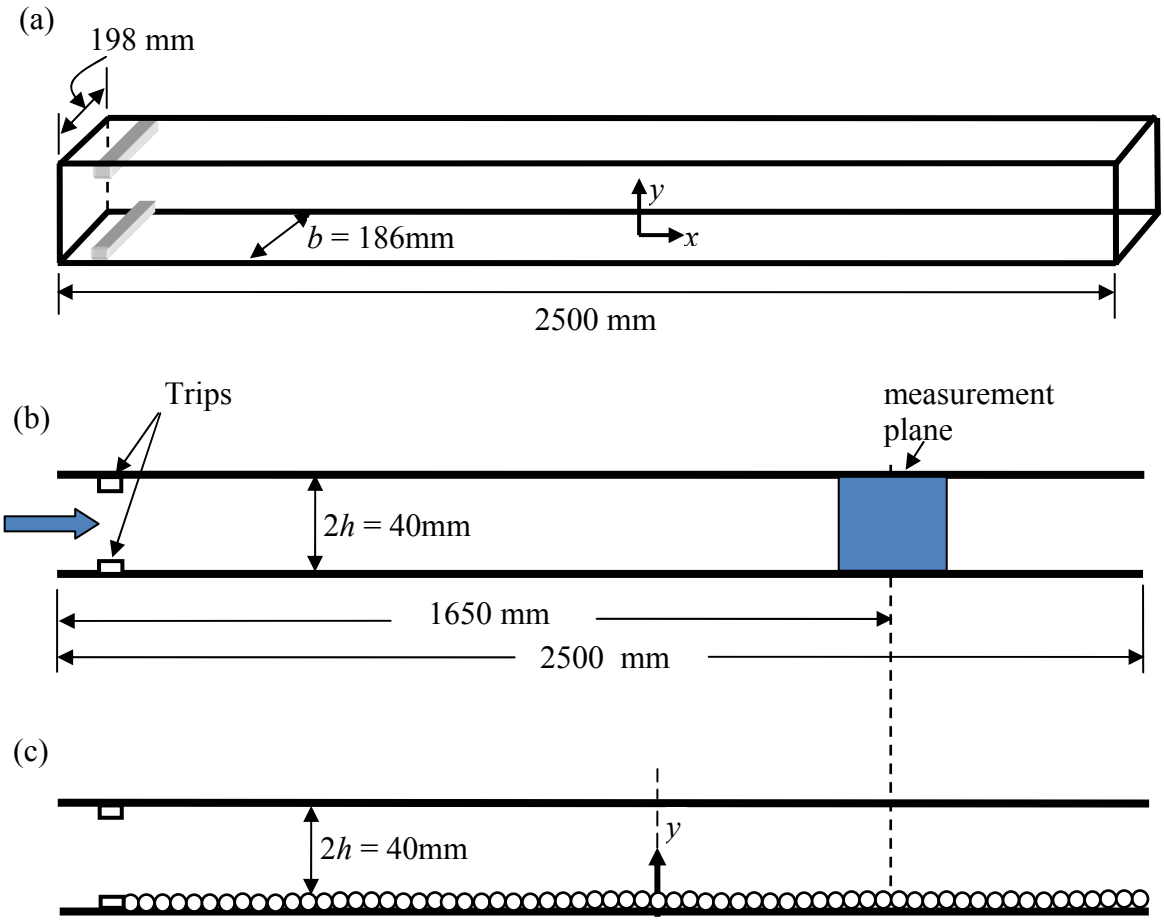

Figure 3.1: Schematic of the test section (not drawn to scale).

tunnel was driven by a centrifugal pump through a series of flow conditioning units that include a perforated plate, a hexagonal honey-comb, mesh screens and a 6.5:1 converging section. The resulting fine-scale flow then passed through the test section for new boundary layers to develop. As indicated in the figure, the x coordinate is aligned with the streamwise direction, while y and z coordinates are respectively aligned with the wall-normal and spanwise directions; $x = 0$ is at the inlet of the test section and $z = 0$ is at the mid-span (see figure 2.1). The origin $y = 0$ is on the lower surface of the smooth-wall and at the crest of the roughness elements. A 3 mm trip made from an acrylic rib was taped to

the lower and upper walls 40 mm downstream of the inlet of the channels to quicken boundary layer transition to turbulence.

3.2 Description of the Particulate Phase

The properties of the two particle types (glass beads and PMMA microspheres) used in the study are summarized in Tables 3.1 and 3.2. The glass beads were purchased from Ferro Cataphote, Jackson, Mississipi, in the size range 100 μm and finer and sieved into the size range 37 - 63 μm. The PMMA particles which were in the size range 120-180 μm were purchased from Fisher Scientific, Ottawa. The values of the particle relative diameter, d_p/L, were calculated using both the viscous length scale (ν/U_τ) and the maximum integral scale (Λ_x) of the fluid. The integral scale was estimated by integrating

Table 3.1: Glass particle characteristics.

	Φ_1	Φ_2
Volume fraction	2.0×10^{-4}	7.0×10^{-4}
Density, ρ (kg/m^3)	2500	2500
Nominal mean diameter, d_p (μm)	50	50
Maximum particle Reynolds number, $Re_{p,max}$	1.5 (10.6)	1.4 (10.6)
Particle time constant, τ_p (ms)	0.35 (0.24)	0.35 (0.24)
Bulk Stokes number, $St_b = \tau_p U_{max}/h$	0.013 (0.005)	0.011 (0.005)
Wall Stokes number, $St_w = \tau_p U_\tau/h$	0.43 (0.29)	0.43 (0.29)
d_p/Λ_x	0.007	0.007
d_p^+	2.2	2.2
Settling velocity, V_s (m/s)	3.4×10^{-3} (2.3×10^{-3})	3.5×10^{-3} (2.3×10^{-3})
Ga	1.36	1.36

Table 3.2: PMMA particle characteristics.

	Φ_1	Φ_2	Φ_3
Volume fraction	2.0×10^{-4}	4.0×10^{-4}	8.0×10^{-4}
Density, ρ (kg/m^3)	1190	1190	1190
Nominal mean diameter, d_p (μm)	150	150	150
Maximum particle Reynolds number, $Re_{p,max}$	38 (14)	35 (10)	38 (9)
Particle time constant, τ_p (ms)	0.75 (1.1)	0.77 (1.2)	0.74 (1.3)
Bulk Stokes number, $St_b = \tau_p U_{max}/h$	0.03 (0.02)	0.03 (0.02)	0.03 (0.02)
Wall Stokes number, $St_w = \tau_p U_\tau/h$	1.51 (2.2)	1.56 (2.4)	1.50 (2.5)
d_p/Λ_x	0.02	0.02	0.02
d_p^+	6.75	6.75	6.75
Settling velocity, V_s (m/s)	7.3×10^{-3} (1.1×10^{-2})	7.5×10^{-3} (1.2×10^{-2})	7.3×10^{-3} (1.2×10^{-2})
Ga	2.50	2.50	2.50

the fluid streamwise velocity fluctuation autocorrelation function. The particle Reynolds numbers correspond to the peak values, $Re_{p,max} = (d_p|U_p\text{-}U_f|/\nu)_{max}$ (calculated near the wall). The corresponding particle response times were calculated using equation 1.18. The particle bulk and wall Stokes numbers were calculated, respectively, using the relations $St_b = \tau_p U_{max}/h$ and $St_w = \tau_p U_\tau/h$. Where property variations occurred due to roughness effects, the rough-wall values are indicated in parentheses.

3.3 Test Conditions

The measurements were made in the mid-plane ($z/b \approx 0$) at $x/h \approx 76$ downstream of the trip. The investigation consists of two series of measurements. In the first series, which was made with the glass beads, the velocities of the carrier and solid phases were measured at different times. The experiments over the smooth wall were run at an

approach velocity of approximately $\overline{U}_{\max} \approx 0.75$ m/s, while those over the rough wall (sand grains) were run at an approach velocity of approximately $U_{max} = 0.50$ m/s, matching the smooth- and rough-wall friction Reynolds numbers at $Re_\tau \approx 700$. The second series of measurements were made with PMMA particles over the smooth wall and gravel roughness. In this case, the velocities of both the carrier and solid phases were measured simultaneously, but under a different set of upstream conditions compared to the glass bead experiment. The change in upstream conditions was necessitated by the occurrence of a more severe decline in the glass particle concentration than expected due to the refined size of the last two meshes (or screens) in the flow conditioning unit. Because of their blockage, a considerable amount of the glass particles was found to collect behind the finer screens, and in the spaces beneath the screen bank of the flow conditioner. Thus, in order to enable a more gradual deposition rate for the larger-size PMMA particles, the finest meshes were removed and the gap underneath the screens sealed with PVC. In the PMMA series, the velocity of the approach flow was set at $\overline{U}_{\max} \approx 1.00$ m/s for the smooth wall and at $\overline{U}_{\max} \approx 0.50$ m/s for the gravel roughness so that the friction Reynolds numbers in both cases is approximately $Re_\tau = 900$. For both series, irrespective of the modifications in the upstream conditions, the turbulence intensity, $\left(\overline{u'^2}\right)^{0.5} / \overline{U}_{\max}$, of the unladen flow, measured in the core region of the channel was about 0.04, which is in agreement with values of approximately 0.04 ± 10 % compiled by Durst et al. (1998) for pipe and channel flows. For ease of reference, the designations $SM\Phi_i$, $SG\Phi_i$ and $GV\Phi_i$ are used to denote the test conditions over the smooth wall, sand grain and gravel roughness, respectively, where $i = 0$ for the unladen flow test cases and $i = 1$, 2, or 3 is used to denote the loading ratio in the particle-laden cases.

3.4 Planar Particle Image Velocimetry

Particle image velocimetry (PIV) is an optical technique for measuring the velocity of small particles moving with a carrier fluid from the images of the particles captured by a digital camera. In the case of small neutrally buoyant particles ($St << 1$, $\rho_p/\rho_f \approx 1$), the particles are considered to follow the carrier fluid motion closely so that the particle velocities can be used to approximate the carrier fluid velocities. In planar PIV, the method is applied to a two-dimensional flow region. Generally, pulsed sheets of light produced by a laser at precise time intervals are used to illuminate the flow field and the images of the light scattered by the particles are recorded on the sensor array of the camera. Image processing methods are then applied to deduce the displacement of the particles from the images. Because the velocity information obtained is over a full field region instead of at pointwise locations as in LDA, PIV provides the desirable advantage of measuring the spatial structures in turbulent flows without the need for using Taylor's hypothesis, for instance, to convert temporal correlations to spatial correlations. Over the past several decades, PIV have been applied to measure fluid velocities in turbulent channel flows and boundary layers (e.g., Liu et al. 1991; Adrian et al. 2000a; Piirto et al. 2001; Stanislas et al. 2008). The technique has also been applied recently in a number of studies on multiphase and particle-laden turbulent flows (e.g., Muste et al. 2009; Deen et al. 2010; Borowsky and Wei 2011).

Figure 3.2 shows the schematic of a typical setup of a planar PIV. The setup consists of a flow carrying small particles, a laser that illuminates the particles in a target window called the field of view (FOV), a charge-coupled device (CCD) camera that captures the images of the illuminated particles, a timer hub that synchronizes the camera

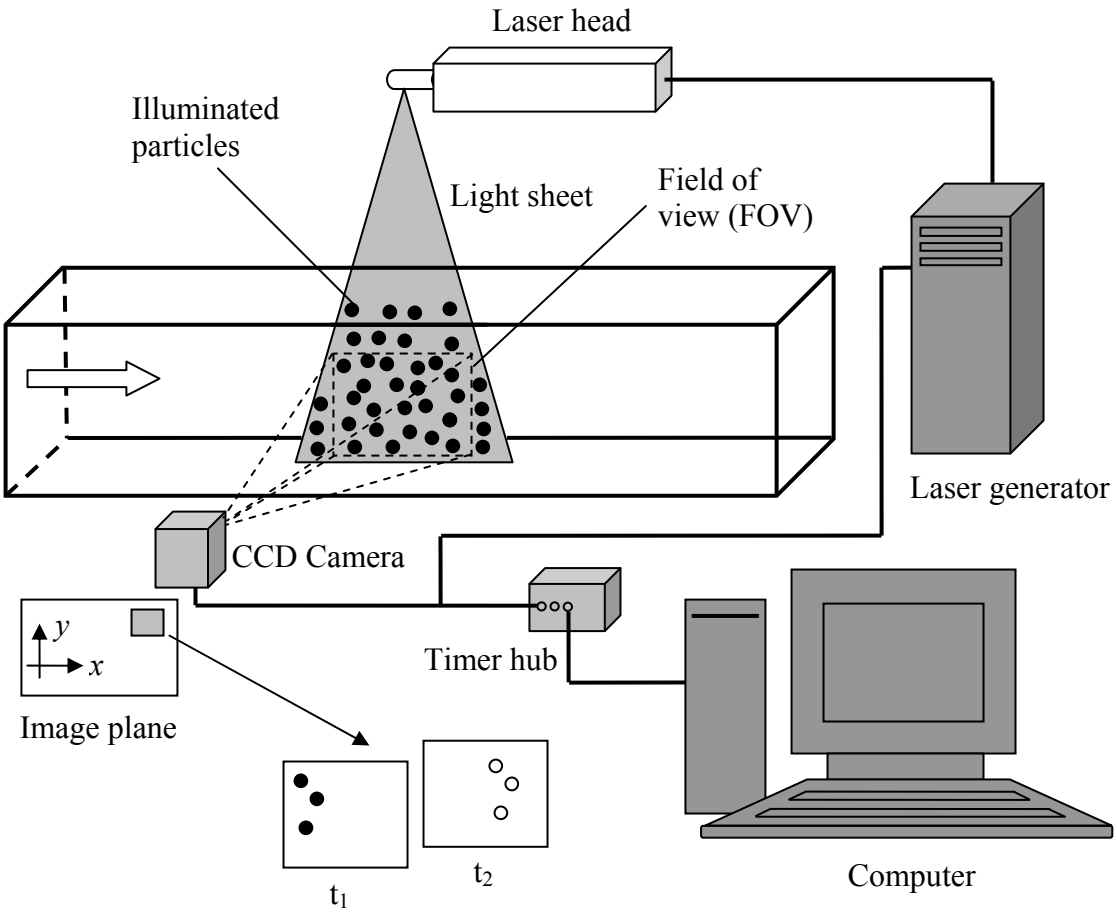

Figure 3.2: A typical setup of a planar PIV system.

with the laser and a computer that controls the entire image acquisition system. During illumination, the laser emits two pulses at times t_1 and t_2 (the time interval Δt depending on the mean flow velocity and the magnification at imaging), and the light scattered by the particles is recorded either on a single frame or on two separate frames of the camera. A computer program is used to divide the image plane into a grid of smaller areas called interrogation areas. For each interrogation area (IA), an auto-correlation or cross-correlation algorithm (depending on number of frames recorded) is applied to statistically determine the local displacement vector ΔX of particles between the first and second

illuminations. The velocity vector, V, within the interrogation area is then calculated as $V = \Delta X/\Delta t$. A velocity vector map of the field of view is obtained by repeating the correlation for each interrogation area over the entire image. The velocities in the FOV are then calculated by taking into account the magnification between sizes of the FOV and the image plane.

3.4.1 Illumination and Recording

Lasers are widely used to illuminate particles in PIV. Their monochromatic light and high-energy intensity makes it possible to form thin sheets of light. A laser consists of three main components, namely, the laser material consisting of atomic or molecular gas, semiconductor or solid material; the pump source that excites the laser material by electromagnetic energy or chemical energy, and the mirror arrangement allowing an oscillation within the laser material. Lasers with double-oscillator systems allow the adjustment of the time interval between the two illuminations irrespective of the pulse intensity. To provide light sheets of high intensity, laser beams with good and stable properties as well as high energy pulses are required. One such laser is the Nd: YAG laser in which the laser beam is generated by Nd^{3+} ions. The laser material can be incorporated into various mediums, and has a high amplification and good thermal properties. Excitation is produced by optical pumping in broad energy bands and non-radiating transitions in to a high energy level. Frequency doubled Nd: YAG lasers emit infra-red radiation whose frequency is doubled to produce green light of wavelength 532 nm. In order to obtain short bursts of light energy, the laser is triggered by means of a quality switch (Q-switch) in which the laser beam is linearly polarized. The intensity of the light

sheet produced is considered to follow a Gaussian distribution of the form

$$I = I_o \exp\left(-8z^2 / d_l^2\right) \qquad (3.1)$$

where I_o is the peak intensity of the sheet and d_l is the light sheet thickness, defined at the $I_o e^{-2}$ intensity level (where $z = d_l/2$).

The most widely used recording device for PIV is the charge-coupled device (CCD) camera, the primary function of which is to provide images at two precisely specified times. The major component of a CCD camera is the CCD sensor which consists of an array of photosensitive cells called pixels. All CCD cameras employed in PIV use high-performance progressive scan interline CCD chips. The chip consists of an array of photosensitive cells and an equal number of storage cells. When the first laser pulse is triggered and the particles are illuminated, the first image is acquired and immediately transferred from the photosensitive cells to the storage cells. When the second laser pulse is triggered, the photosensitive cells again are used to store the second image. Both images are then transferred sequentially from the camera to the computer for storage. CCD sensors are available as large arrays of pixels, the number of pixels depending on the spatial resolution required. Some common examples are 1024 × 1024 pixel (1M pixels) and 2048 × 2048 pixel (4M pixels).

Two general image recording modes are used in PIV: single-frame/multi-exposure recording and multi-frame/single-exposure recording. In single-frame/multi-exposure mode, two or more exposures are made on the same frame, resulting in multiple images of the same particle within the frame. The method is successful only when a relatively small number of particles are involved since too many particles in the flow leads to overlapping images. Another disadvantage relates to the effect that particle motion can

not be determined uniquely as there is no way to decide which image comes from the first illumination or the second illumination. This directional ambiguity is easily overcome by multi-frame/single-exposure techniques that record particle images on two or more frames within a single exposure. The particle image intensity is approximated by a two dimensional Gaussian distribution of the form

$$I_p(x,y) = I \exp\left[-8\left(\left(x-x_p\right)^2 + \left(y-y_p\right)^2\right)\Big/ d_t^{\,2}\right] \tag{3.2}$$

where I is the laser sheet intensity distribution given by equation 3.1, (x_p, y_p) is the location of the peak intensity and d_t is the particle image diameter given by (Adrian 1991):

$$d_t = \left(M^2 d_p^{\,2} + d_s^{\,2}\right)^{1/2} \tag{3.3}$$

where M is the magnification and d_s is the width of the Airy function of a diffraction limited lens. For a camera of f-number, $f^{\#} = f / D_a$, where f is the focal length and D_a the aperture diameter, the Airy function width is given by (Adrian 1991):

$$d_s = 2.44(1+M) f^{\#} \lambda \tag{3.4}$$

where λ is the wavelength of the light. Knowing the particle intensity distribution, the corresponding particle pixel value is the integral over the area of the pixel:

$$I_{px}(x,y) = I \iint \exp\left(-8\frac{\left(x-x_p\right)^2 + \left(y-y_p\right)^2}{d_t^{\,2}}\right) dxdy \tag{3.5}$$

3.4.2 Statistical Evaluation of Recorded Images

The images recorded in a PIV are processed numerically using a correlation algorithm to determine the displacements of the particle images. To calculate the particle displacement

for a given interrogation area (*IA*), the pixel intensity values are statistically correlated with one another over the same *IA* (auto-correlation), or with the pixel intensity values of a corresponding *IA* in another image (cross-correlation). Thus, for an image divided into interrogation areas of size $K \times L$ (where the sizes are in pixels), the general formulation for the correlation for a spatial domain is given by

$$R(x,y) = \sum_{i=-K}^{i=K} \sum_{j=-L}^{j=L} I_1(i,j) I_2(i+x, j+y) \tag{3.6}$$

where the intensity values I_2 belong to either the same *IA*, or the corresponding *IA* of a second image, depending on the approach used.

In practice, the evaluation of the spatial correlations is found to be computationally intensive due to large pixel array sizes of most CCD cameras. Thus, to reduce the cost of calculations, the more efficient two-dimensional fast Fourier transform (FFT) algorithm is utilized. This makes use of the mathematical correlation theorem which is applied to compute cross-correlations of two variables as the inverse Fourier transform (IFFT) of the complex conjugate multiplication of the Fourier transform of the variables. The correlation results in a two-dimensional correlation map with three peaks for auto-correlation and two peaks for cross-correlation. The three peaks in an auto-correlation map correspond to a large central peak (or self-correlation peak) and two displacement peaks, one on each side of the central peak. The distance from the central peak to either of the displacement peaks gives the average displacement of the particle in the interrogation area. The two peaks in a cross-correlation map, on the other hand, correspond to a large (signal) peak and one smaller (noise) peak. The distance of the larger peak from the origin gives the displacement of the particle. A detailed discussion

of the mathematical background of the two correlation methods in PIV and their limitations can be found in Westerweel (1997) and Raffel et al. (1998).

An advanced form of the cross-correlation algorithm known as adaptive-correlation is commonly used in evaluating PIV images. As an iterative method it relies on the knowledge of an initial guessed velocity distribution which is used to introduce an offset from the first interrogation area to the second interrogation area. The result of each single displacement calculation is then used as an input to evaluate the interrogation parameters for the subsequent iteration. The process is terminated after a prescribed number of iterations. The use of adaptive correlation helps to provide two major benefits, including increased signal-to-noise ratio, and the possibility of using multigrid calculations in which coarse grids are used to estimate the offset velocity distribution.

3.4.3 Two-Phase Particle Image Velocimetry

Although PIV has been originally applied to the measurement of single-phase turbulent flows, the technique has been adapted to the study of multi-phase flows as well. In multiphase flow applications, the main difficulty that confronts experimentalists when PIV is employed is how best to discriminate between the different phases with minimal cross-talk. A variety of strategies have been used in the literature to accomplish phase discrimination in the PIV measurement of particle-laden flows. Several examples are cited by Khalitov and Longmire (2002) along with summaries of some of the previous studies that employed those criteria. Khalitov and Longmire (2002), for instance, identified criteria such as colour of the light scattered (or emitted) by particles, differences in image intensity, particle image size (or shape), spatial frequency and

correlation peak properties. In phase discrimination by colour, for example, one of the phases is arranged to produce light of a different wavelength (or colour) that is then filtered by an appropriate filtering method. Discrimination by image intensity and particle image size are based on a comparison of particle image intensities and size, respectively, to pre-set threshold values in order to decide which belong to the particles or the carrier fluid.

In the present work, fluorescence produced by tracer particles and Mie scattering from solid particles are relied upon to obtain phase separation. Similar methods have been applied in previous particle-laden investigations such as Towers et al. (1999), Hagiwara et al. (2002), Toth et al. (2009) and Borowsky and Wei (2011).

3.5 Measurement Procedure

A planar PIV was used to measure the velocities of fluid and particles. In the experiment with glass particles, a single 12-bit CCD camera with 2048 × 2048 pixel array was used to acquire separate images of the glass and tracer particles. The flow was illuminated from above the test section with a Nd: YAG double-pulsed laser of 532 nm wavelength and 15 Hz repetition rate. The laser emits green laser light up to a maximum of 120 mJ/pulse. The PIV parameters are summarized in Table 3.3. The tracer particles (polymer microspheres) were coated with Rhodamine B. Rhodamine B is a fluorescent dye that absorbs green laser light at a wavelength of 532 nm and emits orange light at a wavelength of 590 nm. Because the flow contained both the solid phase and tracer particles, the laser produced Mie scattering images from the solid phase as well as fluorescent images from the tracer particles. In order to discriminate between the two

Table 3.3. PIV experimental parameters

Parameter	Value
Camera pixel pitch	7.4 μm
Laser power	60 mJ (Mie scattering); 120 mJ (Fluorescence)
Aperture (*f* number)	5.6
Light sheet thickness	0.5 mm
Field of view (FOV)	50×50 mm^2
Pulse separation (Δt)	470 μs (U_{max} = 0.5 m/s); 235 μs (U_{max} = 1.0 m/s)
Magnification (M)	0.304
Diameter of tracer particles	10 μm
Image sampling frequency	4 Hz (4 image pairs per second)
Nyquist frequency	2 Hz

phases, the camera was fitted with a long-pass cut-off filter that blocked the green laser light and captured only the fluorescent light emitted by the tracer particles. An ensemble of 5000 images was acquired which was found to be sufficient for the flow statistics to converge. After acquiring the fluid phase velocities, the flow was agitated vigorously to bring settled particles back into circulation. The solid phase velocities were then measured by replacing the fluorescent filter with a green filter that captured only the Mie scattered light from the solid particles.

To measure the velocities of the PMMA particles and the fluid, a two-camera setup was used as shown schematically in figure 3.3. The cameras were mounted on opposite sides of the measurement plane and were synchronized for a simultaneous measurement of the particles and fluid velocities. In order to discriminate between the two phases, one camera was fitted with a green filter that captured the Mie scattering images from the solid phase, while the other camera was fitted with a long-pass cut-off filter to block the laser light but capture the fluorescent images. An ensemble of 7000

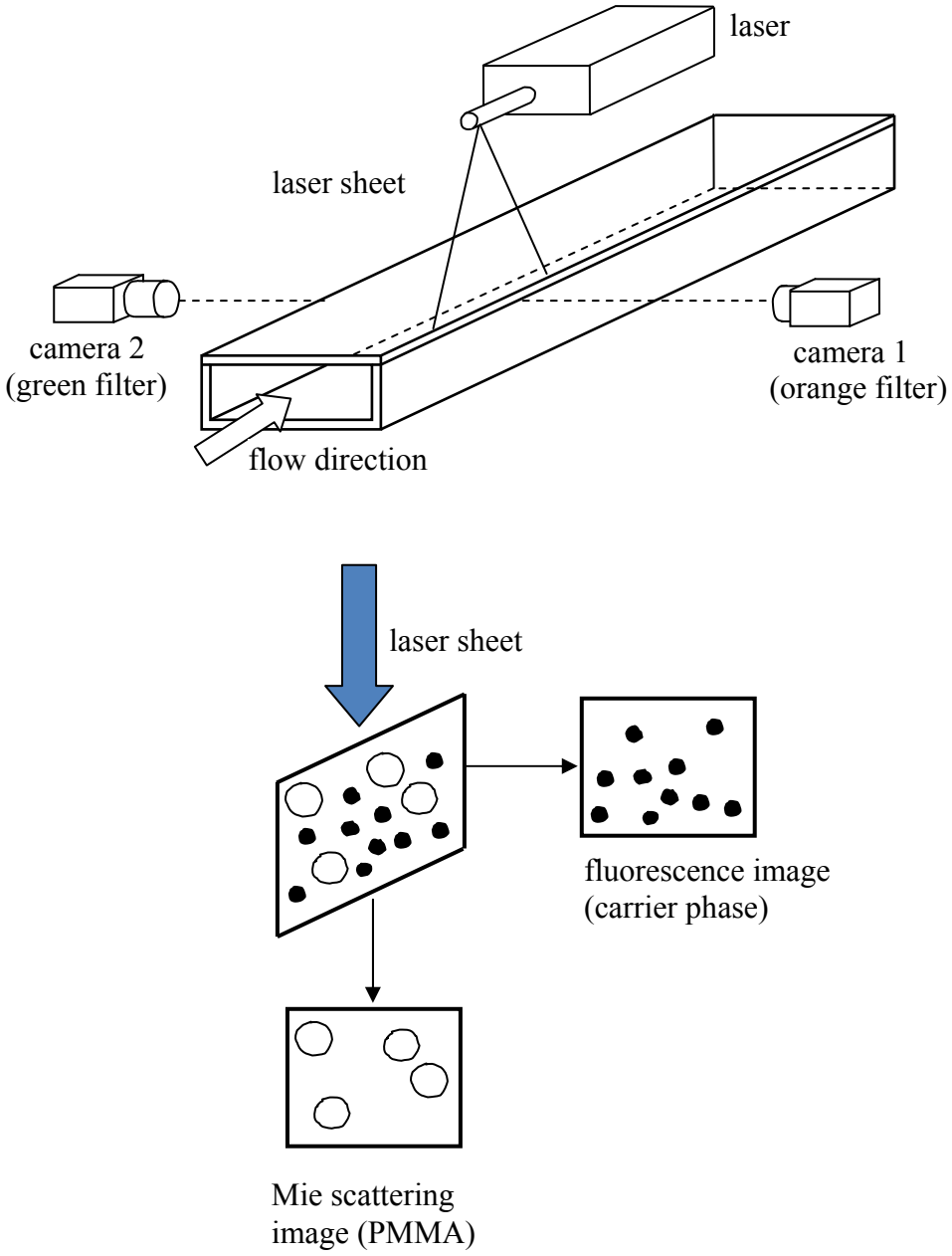

Figure 3.3: Schematic of the two-camera methodology.

instantaneous image pairs was acquired for each phase. However, because the available memory buffer was shared between the two cameras, the data for the particle-laden flows were acquired in two smaller ensembles of 3500 samples.

In all experiments, data acquisition was controlled using the DynamicStudio software developed by Dantec Dynamics. The interrogation area (IA) size for the correlation was set to 32 pixels × 32 pixels with 50% overlap in both x and y. The data were post-processed using the adaptive correlation option of DynamicStudio. The adaptive correlation algorithm used a multi-pass FFT with a one-dimensional Gaussian peak-fitting function to determine the average particle displacement within the interrogation area to sub-pixel accuracy. During the image acquisition, steps were taken to ensure that the maximum particle displacement was less than ¼ of the IA size. With an IA size of 32 pixels × 32 pixels, the maximum particle displacement in the main flow direction was 8 pixels with a dynamic range of 80. The spatial resolution and physical spacing between the velocity vectors in the y-direction were, respectively, 0.788 mm and 0.394 mm.

3.6 Particle Number Density Analysis

The number density of the solid phase was calculated using image processing. An accurate determination of the particle number density in PIV requires an efficient particle identification algorithm. The algorithm has to be able to overcome the drawbacks associated with most particle imaging methods such as uneven illumination, overlapping particle images, too small and out of shape images, out of focus images and image noise. The process of analyzing images to compute particle number distributions consists generally of two main steps, namely, particle centroid determination, and image segmentation. To determine the location of centroids of particles in a laser illuminated image, a Gaussian light intensity distribution is usually assumed (e.g., Ohmi and Li 2000;

Lecuona et al. 2000; Lee et al. 2008; Cardwell et al. 2011). A peak-finding algorithm is then used to detect the locations of the peak intensities, considered to correspond to the particle centroids. To minimize false detections, the peak intensities are compared with a user-specified threshold value that classifies intensity values as belonging to either particles or the background. In the segmentation stage, the image is divided (or segmented) into regions of connected pixels formed by grouping pixel values around the peak intensities.

In the present analysis, an efficient peak-finding algorithm that employed the morphological process of erosion was used. In the image erosion step, a small image mask, also known as a structuring element, which here, is a 5×5 square element, was translated over the image and at each pixel location, was iteratively subtracted from the image intensity values until the peak values were reduced to zero. The locations of the peak values were then recorded for subsequent segmentation. To classify the peak intensities as belonging to either particles or the background, a manual threshold of 350 based on the assessment of contrast enhanced raw images in DynamicStudio, was adopted. Peak intensity values that fell below this threshold level were considered as part of the background and were rejected. Even though this choice of threshold is subjective, it was found to be more reliable than values obtained using automatic thresholding techniques (e.g., Otsu 1979; Zhang and Hu 2008). A region growing algorithm was used to add adjacent pixels to the centroid until a connected object was formed whose diameter matched the particle Airy function diameter.

The reliability of the particle detection algorithm was tested by performing a Monte Carlo simulation with synthetically generated images. The simulation showed

particle recovery to be within 98% for volume fractions less than 1.0×10^{-3}, whereas for the case of larger volume fractions, data recovery was lower (approximately 75%) due to overlapping particle images. Particle number density values were assigned to the *x*-*y* grid by dividing the field of view into bins of dimension equal to the PIV interrogation area size. Values of the particle concentration, C (in kg/m^3), were calculated from the relation $C = m_p N_p$, where m_p is the mass of particles and N_p is the number density (in particles/m^3).

3.7 Uncertainty Estimates

Measurement uncertainty analysis was made following the AIAA standard derived and explained by Coleman and Steele (1995). In general, a complete uncertainty analysis involves identifying and quantifying both the bias and precision errors in each part of the measurement chain. Detailed analyses of bias and precision errors inherent in PIV are available in Prasad et al. (1992) and Forliti et al. (2000). Forliti et al. (2000) have shown that a Gaussian peak-fitting algorithm has the lowest bias and precision errors. In the present study, the uncertainties in the mean velocity, turbulent intensities and Reynolds shear stress at 95% confidence level were estimated to be ±5 %, ±7 %, and ±10 %, respectively. Close to the rough surfaces, uncertainties were estimated to be ±5.5%, ±8% and ±12.5% respectively. In the particle number density measurements, the uncertainty was estimated to be ±2%. Details of the uncertainty estimates are presented in appendix C.

CHAPTER 4

RESULTS AND DISCUSSION

Statistical distributions of various quantities such as particle concentration, particle and fluid mean velocities, velocity fluctuation moments and two-point correlations were extracted over the smooth and rough walls. Statistics calculated at various streamwise and spanwise locations in the unladen flow were used to investigate the streamwise development and two-dimensionality of the flow. Both instantaneous and statistical results obtained in the unladen flow are examined in comparison to the particle-laden cases in order to quantify the impact of particles on the smooth- and rough-wall turbulence. Details of the flow development and two-dimensionality study are presented in appendix B.

4.1 Data Reduction Methods

One of the common methods of data reduction in turbulence measurements is ensemble averaging. In this method, average values of the turbulence quantities are calculated by summing over a number of instantaneous realizations. For statistically steady turbulent flow, the ensemble average taken over a large number of realizations is independent of time. Nevertheless, there are many cases in practice in which a statistically stationary turbulence is never realized such as encountered in pulsatile flows, turbulent combustion and supersonic turbulent flows. For such cases, non-stationary statistical data analysis techniques must be employed in order to interpret the turbulence data. In this study, ensemble averaging was used to calculate the turbulence statistics for the single-phase

flow, while for the particle-laden turbulent flows, non-stationary techniques such as variable interval time averaging (VITA) and a new averaging method that accounted for variations in the particulate phase concentration were used to calculate the flow statistics.

4.1.1 Ensemble Averaging

Because of the randomness of turbulence, the measured instantaneous velocities take on distinctly different values in different realizations of the flow. The ensemble average of the turbulence field, $U_i(x, y, t)$, which yields the mean velocity $\overline{U}$ is given by

$$\overline{U_i} = \frac{1}{N}\sum_{j=1}^{N} U_i\left(x, y, t_j\right) \tag{4.1}$$

where N is the number of independent realizations of the flow field.

Using the Reynolds decomposition formula, the instantaneous velocity values are given by

$$U_i = \overline{U_i} + u_i' \tag{4.2}$$

where u_i' is the fluctuating part of the velocity and $\overline{u_i'} = 0$. To obtain statistics of the higher-order moments of the fluctuating velocity, ensemble averaging is used with the instantaneous fluctuating velocity set to

$$u_i' = U_i - \overline{U_i} \tag{4.3}$$

yielding the Reynolds stresses:

$$\overline{u_i'u_j'} = \frac{1}{N}\sum_{k=1}^{N}\left[U_i\left(x, y, t_k\right) - \overline{U_i}(x, y)\right]\left[U_j\left(x, y, t_k\right) - \overline{U_j}(x, y)\right] \tag{4.4}$$

For the present 2D turbulence experiments, this yields

$$\overline{u'^2} = \frac{1}{N}\sum_{k=1}^{N}\left[U(x,y,t_k) - \overline{U}(x,y)\right]^2 \tag{4.5}$$

$$\overline{v'^2} = \frac{1}{N}\sum_{k=1}^{N}\left[V(x,y,t_k) - \overline{V}(x,y)\right]^2 \tag{4.6}$$

$$\overline{u'v'} = -\frac{1}{N}\sum_{k=1}^{N}\left[U(x,y,t_k) - \overline{U}(x,y)\right]\left[V(x,y,t_k) - \overline{V}(x,y)\right] \tag{4.7}$$

where $\overline{u'^2}$ and $\overline{v'^2}$ are, respectively, the streamwise and wall-normal Reynolds stress, and $\overline{u'v'}$ is the Reynolds shear stress. From equations 4.5 and 4.6, the streamwise and wall-normal turbulence intensities were calculated, respectively, as

$$\overline{u'^2}^{0.5} = \sqrt{\frac{1}{N}\sum_{k=1}^{N}\left[U(x,y,t_k) - \overline{U}(x,y)\right]^2} \tag{4.8}$$

$$\overline{v'^2}^{0.5} = \sqrt{\frac{1}{N}\sum_{k=1}^{N}\left[V(x,y,t_k) - \overline{V}(x,y)\right]^2} \tag{4.9}$$

Bradshaw (1971) recommended that the ensemble averaging technique is also appropriate for the statistical analysis of non-stationary turbulent flows provided the experimental observation consists of records of ensembles of the instantaneous velocities, that is, if one records an ensemble of ensembles. Thus, for example, if there are *M* different ensembles, each of sample size *N*, equations 4.1, 4.5 - 4.9 can be evaluated over the sample size *M* for each temporal point t_k (k = 1 to N) to give time dependent averaged quantities. Since a large number of repetitions (*M* equal to at least 500) would be required for the measured quantities to be statistically significant, this approach was found to be impractical due to data storage constraints.

4.1.2 Variable Interval Time Averaging (VITA)

Variable interval time averaging (VITA) is a technique for calculating time varying local averages in turbulent signals. The VITA values are obtained by averaging the signal over a small moving temporal window whose size, T, is chosen based on the time scales of the turbulence signal. The technique has been used widely in the past to detect the presence of bursting events in steady turbulent flows (e.g., Blackwelder and Kaplan 1976; Bogard and Tiederman 1986; Morrison et al. 1989). For a given velocity field, U_i (x, y, t), the variable interval time average is defined as

$$\hat{U}_i(x,y,t;T) = \frac{1}{T}\int_{t-\frac{1}{2}T}^{t+\frac{1}{2}T} U_i(x,y,t)\,dt \qquad (4.10)$$

where T is the averaging period. In order to capture the turbulent fluctuations in the average, the averaging period T must be large in comparison with the turbulent time scales, but smaller than the time scale of the mean motion, where the time scale of the mean motion is to be understood as the characteristic time of the fluctuations in the time varying mean signal. The values of $\hat{U}_i$ as calculated by equation 4.10 can be considered as low-pass filtered values of the instantaneous signal which can then be subtracted from the corresponding instantaneous velocities to obtain the instantaneous velocity fluctuations or high-pass filtered signal.

When used in burst detection a localized variance of the velocity signal is also calculated, which is given by

$$\hat{U}_{i,\mathrm{var}}(x,y,t;T) = \hat{U_i^2}(x,y,t;T) - \left[\hat{U}_i(x,y,t;T)\right]^2 \qquad (4.11)$$

where a detection is said to occur when the localized variance exceeds some predefined threshold value, K, multiplied by the square of the root-mean-square velocity. However, because of the averaging, VITA can only detect the front and back of a bursting event;

while the central portion or peak signal is dropped out of the averaging process. Another limitation is the sensitivity of the results to the threshold value so that a given fractional change in the threshold, for instance, can produce a fractional change of the same order in the final statistics (Chen and Bradshaw 1988). In the present study, bursting events are investigated by means of the quadrant decomposition method, and the coherent structures in the flow are further explored using more objective structure identification techniques such as POD and wavelet decomposition.

4.1.3 Concentration-Weighted Averaging

In order to account for the non-stationarity of the particle concentration field, and the possible influence on the velocities of the two phases, a concentration-weighted averaging scheme was developed. Using equation 1.5, a volume fraction weighted mean velocity is introduced

$$\langle U_i \rangle = \frac{\overline{\phi U_i}}{\overline{\phi}} \tag{4.12}$$

where ϕ is the volume fraction of the phase in question. For the particulate phase ϕ is taken as ϕ_v, the volume fraction of the particles, while for the carrier fluid $\phi = 1 - \phi_v$. The instantaneous velocity is then decomposed according to equation 1.4 as

$$U_i = \langle U_i \rangle + u_i'' = \frac{\overline{\phi U_i}}{\overline{\phi}} + u_i'' \tag{4.13}$$

where u_i'' represents the fluctuating part of the velocity U_i, which includes the effects of concentration fluctuations. The expression given in equation 4.13 is analogous to Favre decomposition (Favre 1965) used for averaging compressible turbulent flows. From

equation 4.13

$$u_i'' = U_i - \frac{\overline{\phi U_i}}{\bar{\phi}} \tag{4.14}$$

from which it is seen that $\langle u_i'' \rangle = 0$. However, whereas $\overline{u_i'} = 0$ in ensemble averaging, $\overline{u_i''} \neq 0$.

After decomposing the instantaneous velocities according to equation 4.13, a number of relevant ensemble averaged statistics can be calculated, taking into consideration the fact that $\langle u_i'' \rangle = 0$ and in general $\langle u_i'' u_j'' \rangle \neq 0$. The significance of the volume fraction weighted averaging method is elucidated when examined in relation to the two-fluid equations of motion (equations 1.1 and 1.2). Equations 1.1 and 1.2 written for an incompressible turbulent flow are given by

$$\frac{\partial \phi}{\partial t} + \frac{\partial}{\partial x_i}\left(\phi U_i\right) = 0 \tag{4.15}$$

$$\rho\left[\frac{\partial}{\partial t}\left(\phi U_i\right) + \frac{\partial}{\partial x_j}\left(\phi U_i U_j\right)\right] = \phi\rho g_i + F_i - \left(\frac{\partial P}{\partial x_i} - \frac{\partial \sigma_{ij}}{\partial x_j}\right) \tag{4.16}$$

Ensemble averaging 4.15 and 4.16 and noting that

$$\overline{\phi U_i} = \overline{\phi\left(\langle U_i \rangle + u_i''\right)} = \bar{\phi}\langle U_i \rangle + \overline{\phi u_i''} = \bar{\phi}\langle U_i \rangle \tag{4.17}$$

and

$$\overline{\phi U_i U_j} = \overline{\phi\left(\langle U_i \rangle + u_i''\right)\left(\langle U_j \rangle + u_j''\right)} = \bar{\phi}\langle U_i \rangle\langle U_j \rangle + \overline{\phi u_i'' u_j''} \tag{4.18}$$

the volume fraction weighted mean continuity and momentum equations become

$$\frac{\partial \bar{\phi}}{\partial t} + \frac{\partial}{\partial x_i}\left(\bar{\phi}\langle U_i \rangle\right) = 0 \tag{4.19}$$

$$\frac{\partial}{\partial t}\left(\bar{\phi}\langle U_i\rangle\right) + \frac{\partial}{\partial x_j}\left(\bar{\phi}\langle U_i\rangle\langle U_j\rangle\right) = \bar{\phi}g_i + \frac{\overline{F_i}}{\rho} - \frac{1}{\rho}\frac{\partial P}{\partial x_i} + \frac{\partial}{\partial x_j}\left(\frac{\overline{\sigma_{ij}}}{\rho} - \overline{\phi u_i'' u_j''}\right) \quad (4.20)$$

4.2 Particle Count and Concentration Profiles

As some of the solid particles settled out of the flow and were not replenished, the total number of particles in suspension depleted with time. The total number of particles in each image was counted and recorded for both sub-ensembles. The variation of the total particle count with time is shown in figure 4.1 for the first sub-ensemble. The smooth wall results obtained at the loading ratios $\Phi_1 = 2.0 \times 10^{-4}$ and $\Phi_2 = 4.0 \times 10^{-4}$ are presented in figures 4.1a and 4.1b, respectively. Corresponding results over the gravel roughness are presented in figures 4.1c and 4.1d. Each plot follows approximately an exponential distribution where the total particle count decays from its initial value to a final relatively steady value. An exponential decay curve of the form $y = y_1 + y_2 e^{at}$, where a, y_1, and y_2 are curve fitting constants, was fitted to the particle count values. The curve fitting results are displayed in figures 4.1e and 4.1f for the smooth and rough walls, respectively, where the particle count values are normalized by the initial particle count and the time is normalized by the mean time scale $h^*/\langle U\rangle_{max}$. The values of the curve fitting parameters a, y_1, and y_2 are summarized in Table 4.1. The latter plots indicate that the higher the initial concentration, the more quickly particles settle out of the flow. The percentage reductions in particle number density for Φ_1, Φ_2 and Φ_3, are approximately 15%, 30% and 70%, respectively, over the smooth wall while over the rough wall the percentage reductions are approximately 20%, 52% and 90%. Because of the relatively higher concentration decline over the rough wall compared to the smooth wall for a given

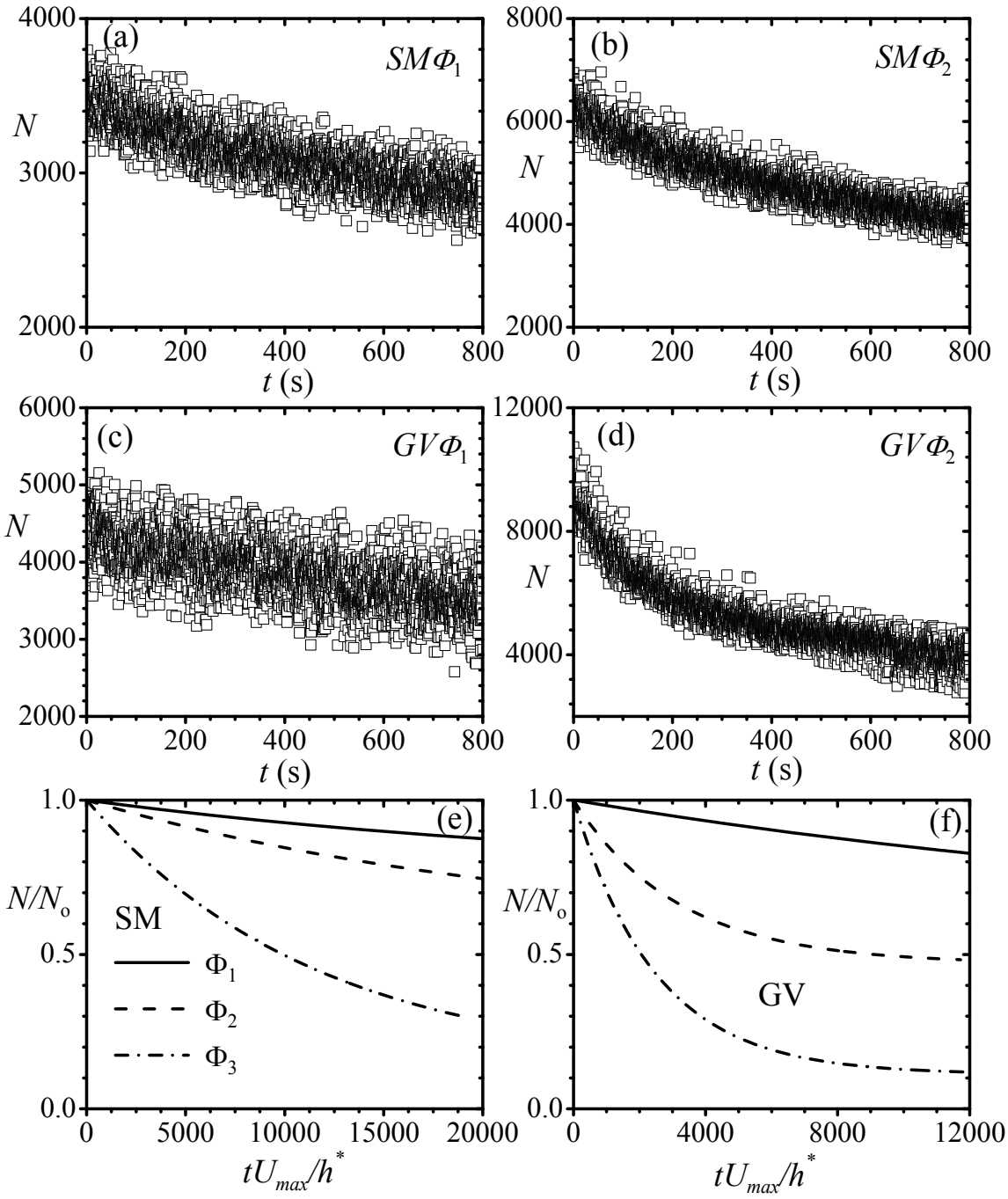

Figure 4.1: Evolution of the total particle count per image over the smooth wall and gravel roughness.

loading ratio Φ, in order to match the smooth and rough wall average volume fractions, a higher startup loading ratio was required for the rough wall. The exponential decay of the

Table 4.1. Values of least square curve fitting parameters for the exponential decay law $y = y_1 + y_2 e^{at}$.

Test	a (s^{-1})	y_1	y_2	R^2-value
$SM\Phi_1$	-1.48×10^{-3}	2597.9	874.6	0.6887
$SM\Phi_2$	-1.85×10^{-3}	3487.5	2747.4	0.8805
$SM\Phi_3$	-3.58×10^{-3}	7735.2	51345.8	0.8111
$GV\Phi_1$	-7.16×10^{-4}	2408.0	1934.8	0.4050
$GV\Phi_2$	-5.55×10^{-3}	4331.6	4886.9	0.9071
$GV\Phi_3$	-6.92×10^{-3}	8906.6	70680.5	0.9826

particle count over the present smooth and rough walls is in qualitative agreement with results obtained by Dritselis (2009) in the study of the deposition of solid particles over a smooth wall and rib roughness.

Since knowledge of the values of the particle mean concentration is very relevant to the present approach, the mean concentration of each test condition was calculated by ensemble averaging. Profiles of the mean concentration across the lower half of the channel are presented in figure 4.2, where the concentration values are normalized by the corresponding bulk value C_b and the wall-normal distance is normalized by the outer scale h^*. The length scale h^*, which corresponds to the distance from the wall to the location of zero crossing of the Reynolds shear stress, is often the normalizing scale of choice for asymmetric (one-sided) rough wall flows. Over the smooth wall, h^* coincides with the channel half-height and is equal to the location of maximum streamwise mean velocity. Over the rough wall, the roughness asymmetry shifts the location of the maximum streamwise mean velocity towards the opposite smooth wall where $h^* \approx 1.5h$. As can be seen, for both the smooth and rough walls, the mean concentration increases towards the bottom wall and the effect increases with increasing volume fraction. In

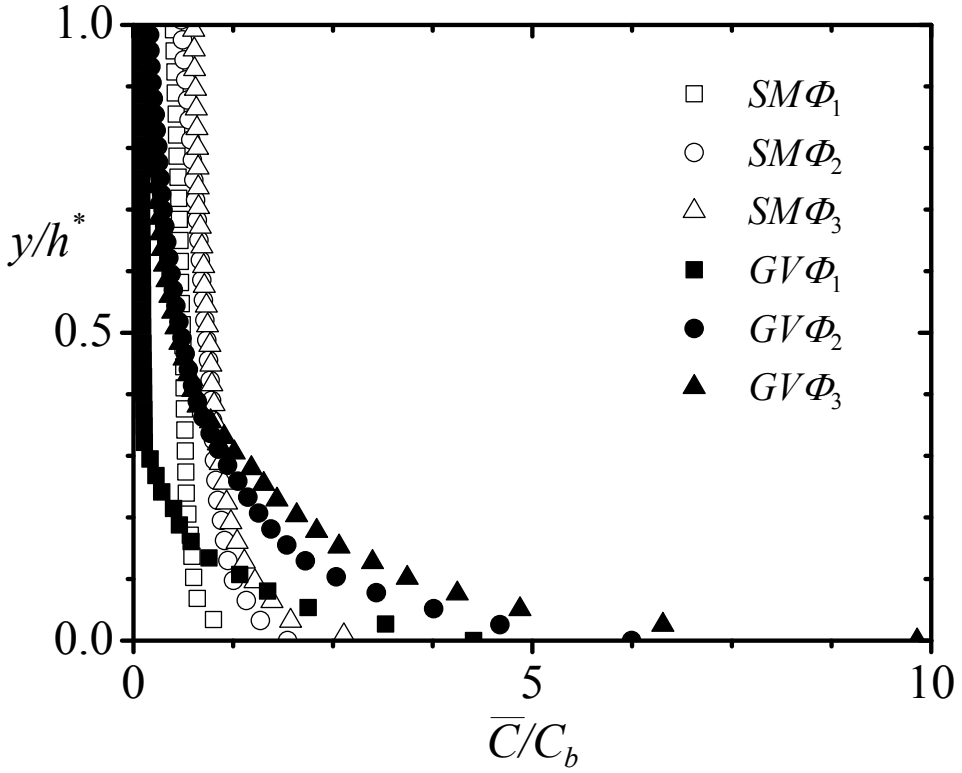

Figure 4.2: Distributions of the particle mean concentration over the smooth wall and gravel roughness.

general, the mean concentration attains a peak value close to the channel wall because of two main reasons: namely, the particles propensity to collect in regions of high strain rate or velocity gradient, and turbophoresis, the process under which particles migrate from regions of high turbulence intensity to regions of low turbulence intensity. In horizontal channels, gravitational settling also plays a part in bringing particles towards the wall. The results also indicate that for a given volumetric loading, wall roughness enhances the peak mean concentration. This enhancement may be considered as an effect of the balance of two forces, namely, the gravitational force and the lift force due to velocity gradient (Saffman lift force). Near the rough wall, because the velocity gradient is higher, particles are trapped by the effect of the Saffman lift force, leading to the presence of

more particles in the vicinity of the rough wall. Because of the larger particle concentration near the rough wall, the values in the core region are comparatively lower than the smooth wall values. This reduction may be attributed to the more rapid particle count decline over the rough wall, resulting from a faster deposition over the rough wall compared to the smooth wall.

4.3 Instantaneous Fluid Velocity Distributions

A quick way of checking for possible non-stationarities in a turbulent velocity signal is by visual examination of the time history plots of the instantaneous velocities. Examples of such plots in the case of the streamwise instantaneous velocity are depicted in figures 4.3a and 4.3b for the smooth and rough wall particle-laden flows, respectively, at $y/h^* = 0.15$. The plots shown correspond to the test conditions $SM\Phi_1$ and $GV\Phi_1$. In both cases, the velocity signal appears fairly random and there are no discernible artifacts of unsteadiness (e.g. periodicity, dampening of the signal amplitude with time, or signal discontinuities). As suggested earlier, a time-dependent mean value of the signal can be calculated by using the variable interval time averaging (VITA) method, by selecting a suitable window size for the averaging. Figures 4.3c, 4.3e and 4.3g, for instance, show plots of the locally averaged mean velocities versus time for increasing values of the averaging period (T = 5s, 25s, and 75s). It should be noted that these periods correspond to sampling frequencies of 0.2Hz, 0.04Hz, 0.013Hz, all of which satisfy the Nyquist sampling criterion. The corresponding plots over the gravel are shown in figures 4.3d, 4.3f and 4.3h. It is clear that the influence of VITA on the instantaneous velocity is to filter out the fluctuations in the signal, and this effect is enhanced as the value of the

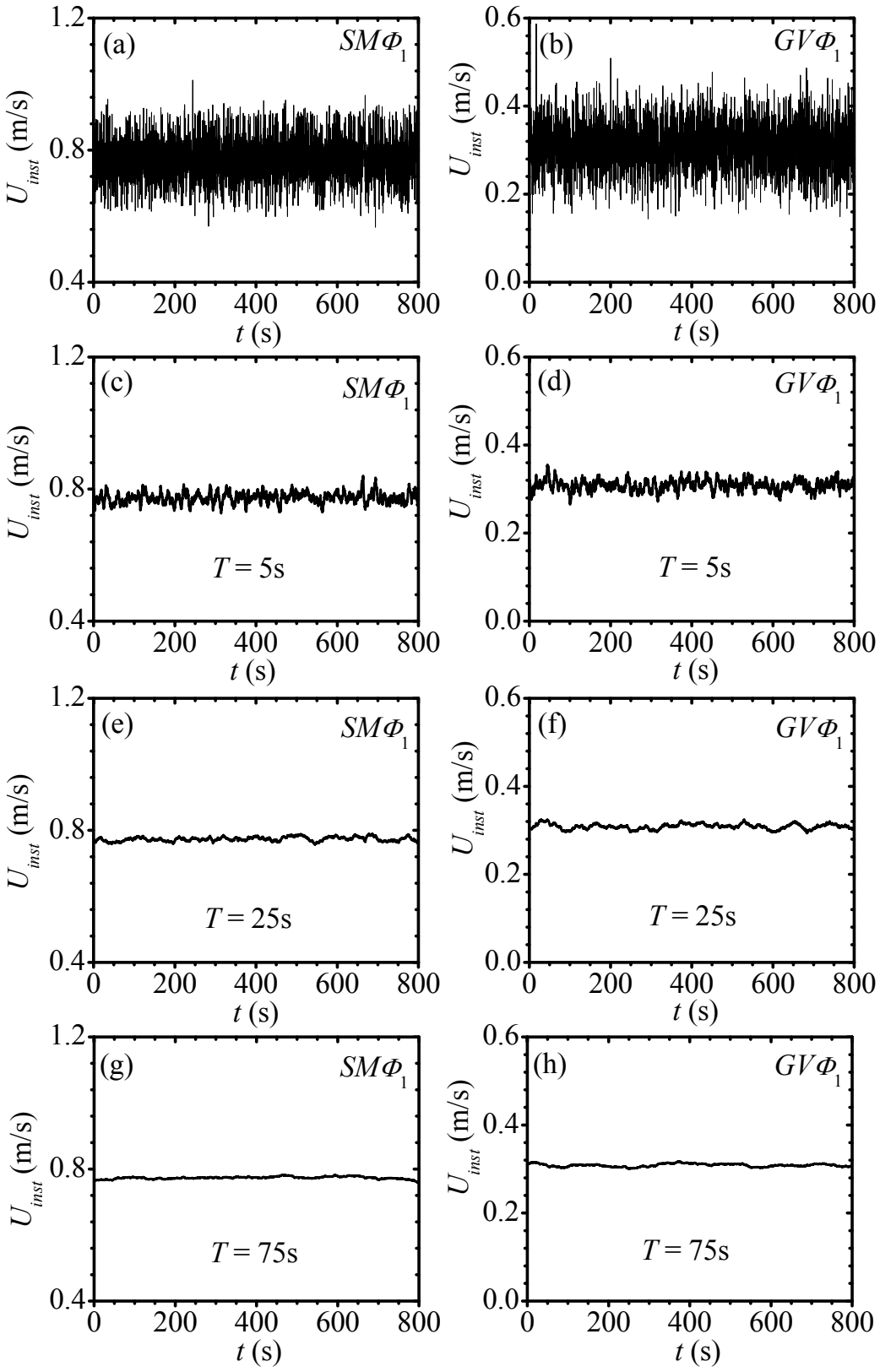

Figure 4.3: Effects of VITA period on the instantaneous streamwise velocity of carrier fluid ($\Phi_1 = 2.0 \times 10^{-4}$) at $y/h^* = 0.15$ over the smooth wall and gravel roughness.

averaging period increases. By progressively increasing the size of the averaging window, the mean velocity approaches more and more the global ensemble averaged mean velocity.

Since the VITA method low-pass filters the velocity, it can be used to decompose the instantaneous velocity fields to reveal the coherent structures in the flow. To accomplish this, a suitable averaging period must be selected. In order to select the most appropriate value of T, a sensitivity analysis was conducted in which various velocity vector maps of the instantaneous fluctuating velocity were examined for structures. The decomposed fields were obtained by subtracting the averaged fields calculated with different values of T from the instantaneous fields. A value of $T = 1.75$s ($f \approx 0.57$Hz) was found to be a good choice of window size for exposing most of the underlying turbulent structures. Figure 4.4 shows the vector maps of selected instantaneous velocity realizations of the smooth and rough wall flows. Figure 4.4a, which corresponds to the unladen smooth wall flow ($SM\Phi_0$), shows sweep-like (Q4) motions. Other realizations revealed ejection-like (Q2) events (not shown), and it was found that both these events are recurrent features of the unladen instantaneous realizations over the smooth wall. In the presence of particles (figures 4.4c, 4.4e and 4.4g), the flow is predominated by large-scale ejections towards the outer layer. The unladen rough wall flow (figure 4.4b), is pervaded by fluid ejections towards the outer layer. These were found to be frequent features of the rough wall flow, which are retained in the presence of particles (figures 4.4d, 4.4f and 4.4h). For a given loading condition, the effect of roughness is to intensify the turbulent motions as portrayed by the darker vector arrows in the rough wall figures.

Figure 4.5 shows the same instantaneous velocity fluctuation fields visualized

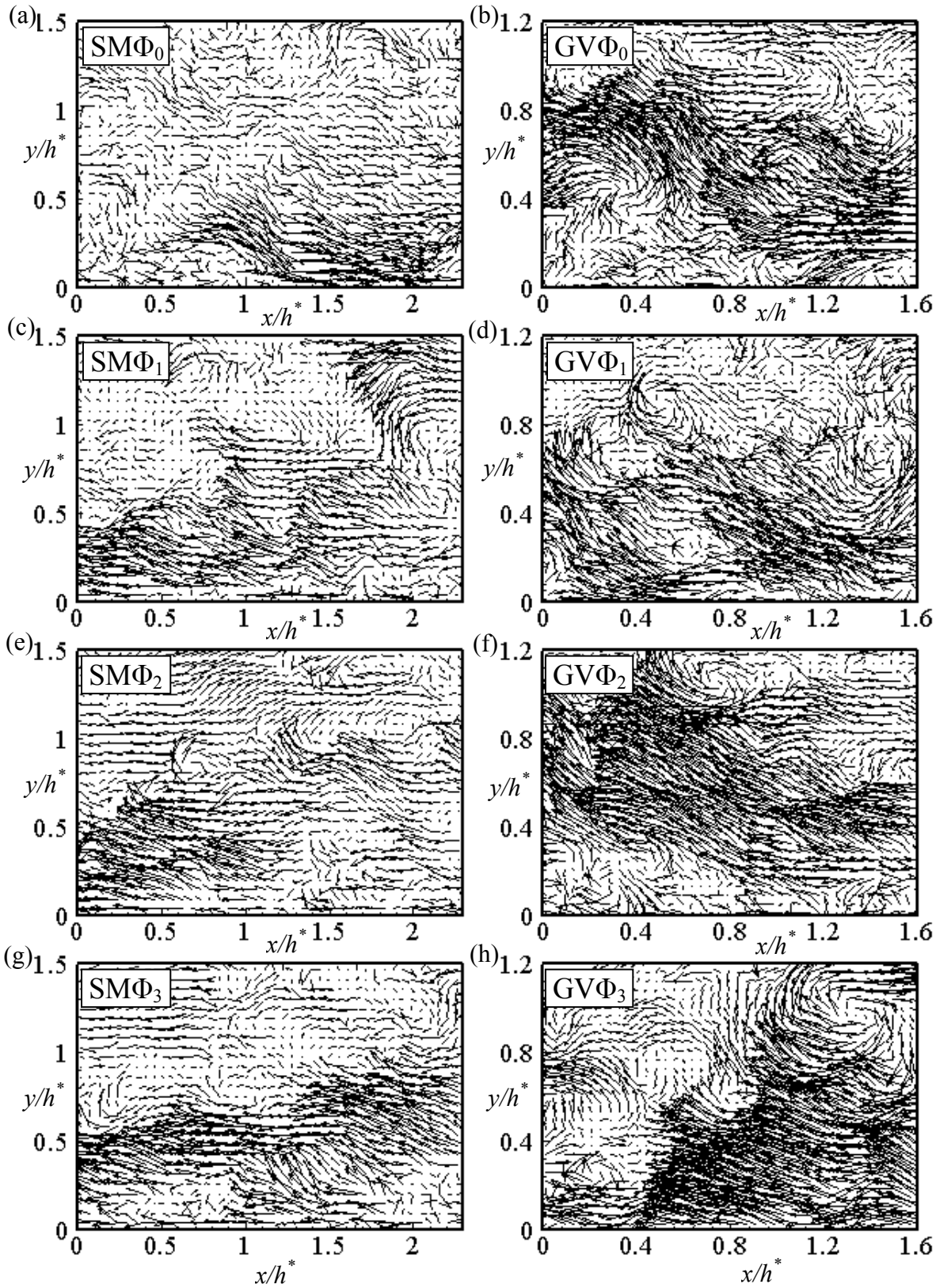

Figure 4.4: Vector maps of the instantaneous fluid velocity fields using the VITA method.

by further decomposition of the high-pass filtered velocity fields of figure 4.4 using the orthogonal wavelet transforms technique. The combined VITA and wavelet decomposition plots retain the gross characteristics revealed by the VITA-only or high-pass filtering method, except that the structures are more clearly visible than before. The fact that no additional features are revealed would imply that the period of T = 1.75s used in the VITA-only decomposition is optimal.

4.4 Statistical Results

In section 4.1.3, the volume fraction-weighted averaging method that couples variations in the particle concentration to the velocity of the two phases was outlined. Before the resulting particle-laden statistics can be compared to their unladen flow counterparts (obtained by Reynolds decomposition), a relationship is needed that will allow a conversion between the two cases. From the definition of the volume fraction-weighted mean velocity, the Reynolds averaged mean velocity can be recovered:

$$\langle U_i \rangle = \frac{\overline{\phi U_i}}{\overline{\phi}} = \frac{\overline{\left(\overline{\phi} + \phi'\right)\left(\overline{U_i} + u_i'\right)}}{\overline{\phi}} = \overline{U_i} + \frac{\overline{\phi' u_i'}}{\overline{\phi}} \tag{4.21}$$

$$\text{Thus, } \overline{U_i} = \langle U_i \rangle - \frac{\overline{\phi' u_i'}}{\overline{\phi}} \tag{4.22}$$

To obtain the Reynolds averaged velocity fluctuations, u_i', we note that

$$\langle U_i \rangle + u_i'' = \overline{U_i} + u_i' . \tag{4.23}$$

This leads to the relation

$$u_i' = u_i'' + \frac{\overline{\phi' u_i'}}{\overline{\phi}} \tag{4.24}$$

Thus, knowing the correlation between the concentration fluctuation and velocity

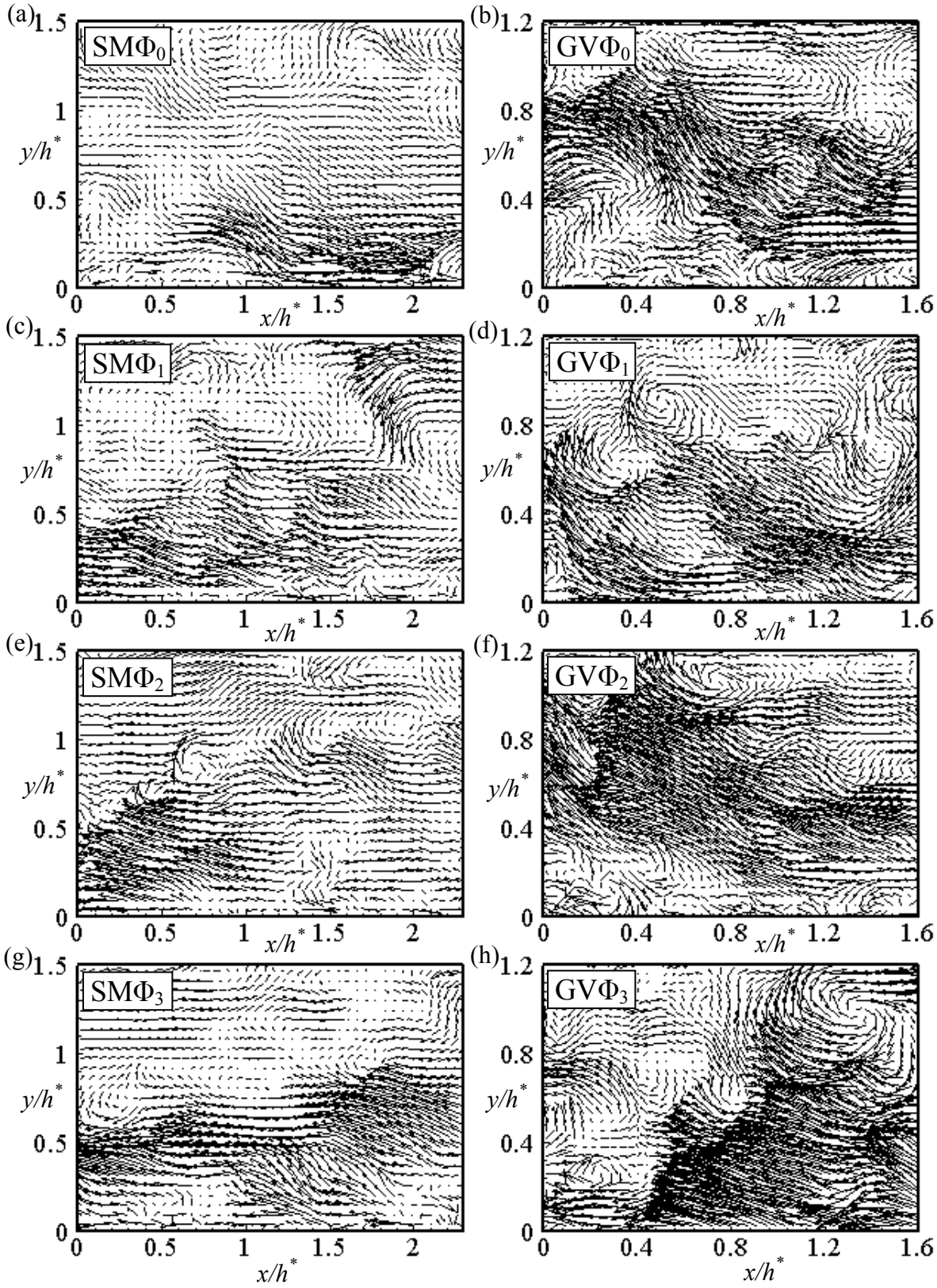

Figure 4.5: Instantaneous velocity vector maps of the flow fields using the combined VITA and wavelet decomposition method.

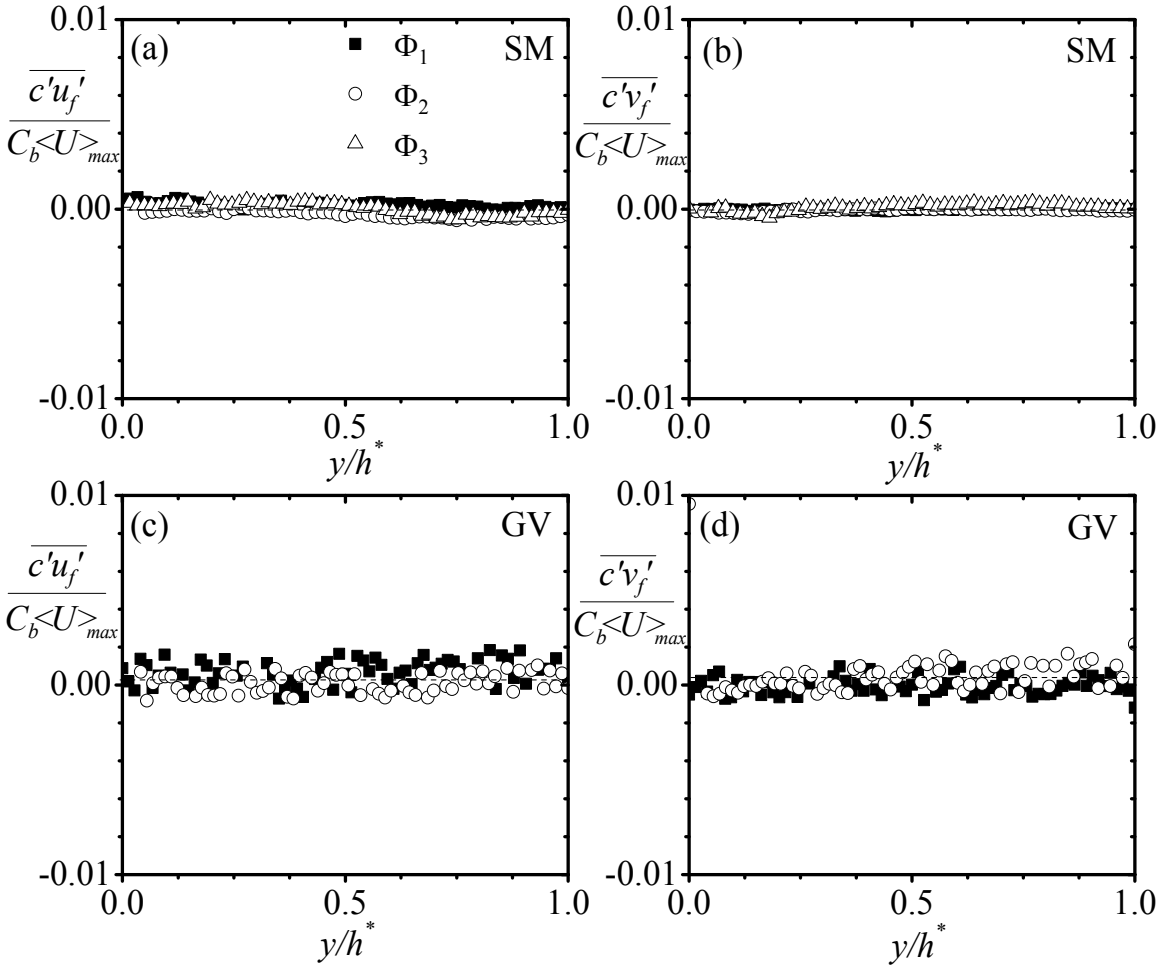

Figure 4.6: Profiles of the particle concentration and fluid velocity correlations over the smooth and rough walls.

fluctuation, the Reynolds averaged velocity fluctuation can be calculated. Sample profiles of concentration-velocity fluctuation correlation for the fluid are shown in figure 4.6. In the plots, the correlation values are normalized by the product of the particle bulk concentration and the maximum streamwise mean velocity of the fluid. The results show that the particle concentration and fluid velocity are uncorrelated. This suggests that the concentration-coupled results can be reasonably compared with the unladen flow results without loss of accuracy.

In the light of the preceding discussion, all statistical quantities, including the mean velocity, turbulent intensities, Reynolds shear stress and two-point correlations are calculated using the volume fraction-weighted averaging method. All calculations are based on the entire ensemble of 7000 images. The velocity fluctuations from which the root-mean-square fluctuations and higher order moments are calculated are based on the decomposition $U_i = \langle U_i \rangle + u_i''$.

4.4.1 Solid Mean Velocity, Turbulent Intensities and Reynolds Shear Stress

Figure 4.7 shows distributions of the particles mean velocity and turbulence characteristics compared to those of the unladen flow. The particle streamwise mean velocity (figure 4.7a) closely matches that of the unladen fluid for the smooth wall irrespective of the three-fold increase in the loading fraction. The same is true for the turbulent intensities and Reynolds shear stress (figures 4.7b-4.7d). The particle streamwise velocity fluctuation intensity reaches peak values close to the wall as in the unladen smooth wall flow. The occurrence of the peak streamwise turbulence intensity near a smooth wall is generally considered a feature of the quasi-streamwise vortices in the near-wall region (e.g. Krogstad et al. 2005). The fact that this is also observed for the solid phase profiles further speaks to how closely the particulate phase motion mimics the carrier fluid motion. Surface roughness reduced both the fluid and solid mean velocities making the mean velocity less full in comparison with the smooth wall profiles. Over the rough wall, though, increasing the loading fraction enhances the roughness effect on the solid phase mean velocity profile. Surface roughness also modifies the fluid and solid

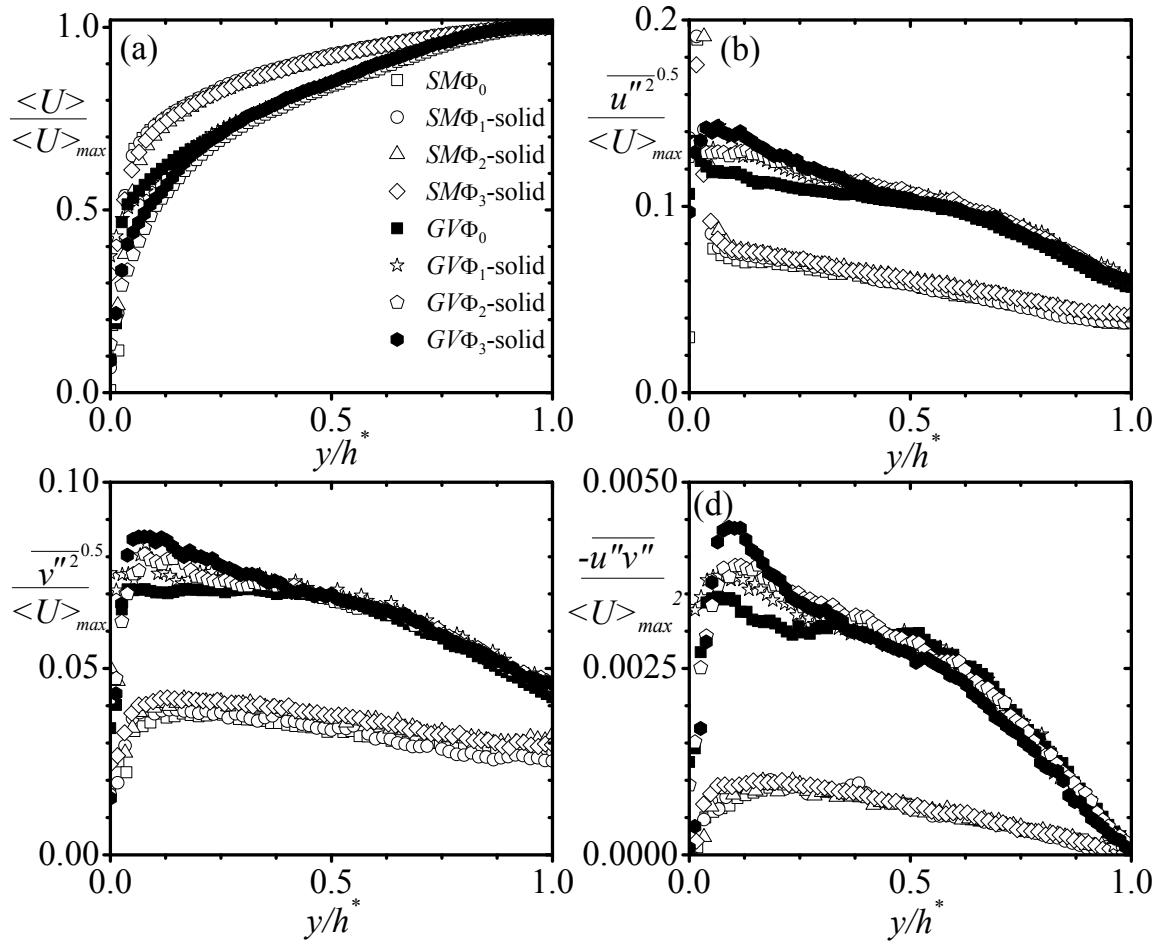

Figure 4.7: Profiles of the mean velocity, turbulent intensities and Reynolds shear stress of the solid phase.

phase turbulence intensities and Reynolds shear stress substantially when compared to the corresponding smooth wall profiles. For the streamwise turbulence intensity, roughness suppresses the peak values but enhances the intensity values over the rest of the flow region. The wall-normal turbulence intensities and Reynolds shear stress are rather increased by roughness over the entire flow region and the effect is more dramatic in the case of the Reynolds shear stress. As with the mean velocity, increasing the loading ratio causes further augmentation of the turbulence intensities and Reynolds shear stress

for $y/h^* \leq 0.35$. The present rough wall results are consistent with results from previous studies (e.g. Benson et al. 2005; Lain and Sommerfeld 2008). These studies explained that particles turbulence intensity profiles tend to develop larger peak values in the presence of wall roughness due to particle-wall collisions.

The good agreement observed between the solid phase and unladen fluid mean velocity, turbulence intensities, and Reynolds shear stress over the smooth wall can be attributed to the relatively low value of the Stokes number ($St_b \approx 0.03$). Over the rough wall, low Stokes number effects are offset by particle-wall collisions. It has been suggested that at low Stokes numbers, the particle velocities can be calculated as a power series expansion of the unladen fluid velocities and the particle response time. This approach, also known as the equilibrium Eulerian method, first proposed by Ferry and Balachandar (2001) is widely used in the numerical study of particle-laden turbulent flows. According to Ferry and Balachandar (2001) and Shotorban and Balachandar (2006), for small particle response times, the particle velocity can be expressed, to first order accuracy, as a series expansion in terms of the surrounding fluid velocity, settling velocity and the particle response time as

$$U_{p,i} = U_{f,i} + V_{s,i} - \tau_p \left(\frac{DU_{f,i}}{Dt} + V_{s,j} \frac{\partial U_{f,i}}{\partial x_j} \right) + O\left(\tau_p{}^2\right) \qquad (4.25)$$

where V_s is the particle settling velocity, $DU_{f,i}/Dt = \partial U_{f,i}/\partial t + U_{f,j}\partial U_{f,i}/\partial x_j$ is the total acceleration of the fluid, and i is a Cartesian index. Thus, as an alternative approach, the above expansion was used to calculate the particulate phase instantaneous velocities, and the corresponding particle mean velocities, turbulence intensities and Reynolds shear stress were calculated. The results are shown in figure 4.8 along with the measured values for comparison. The agreement between the measured and equilibrium approximation

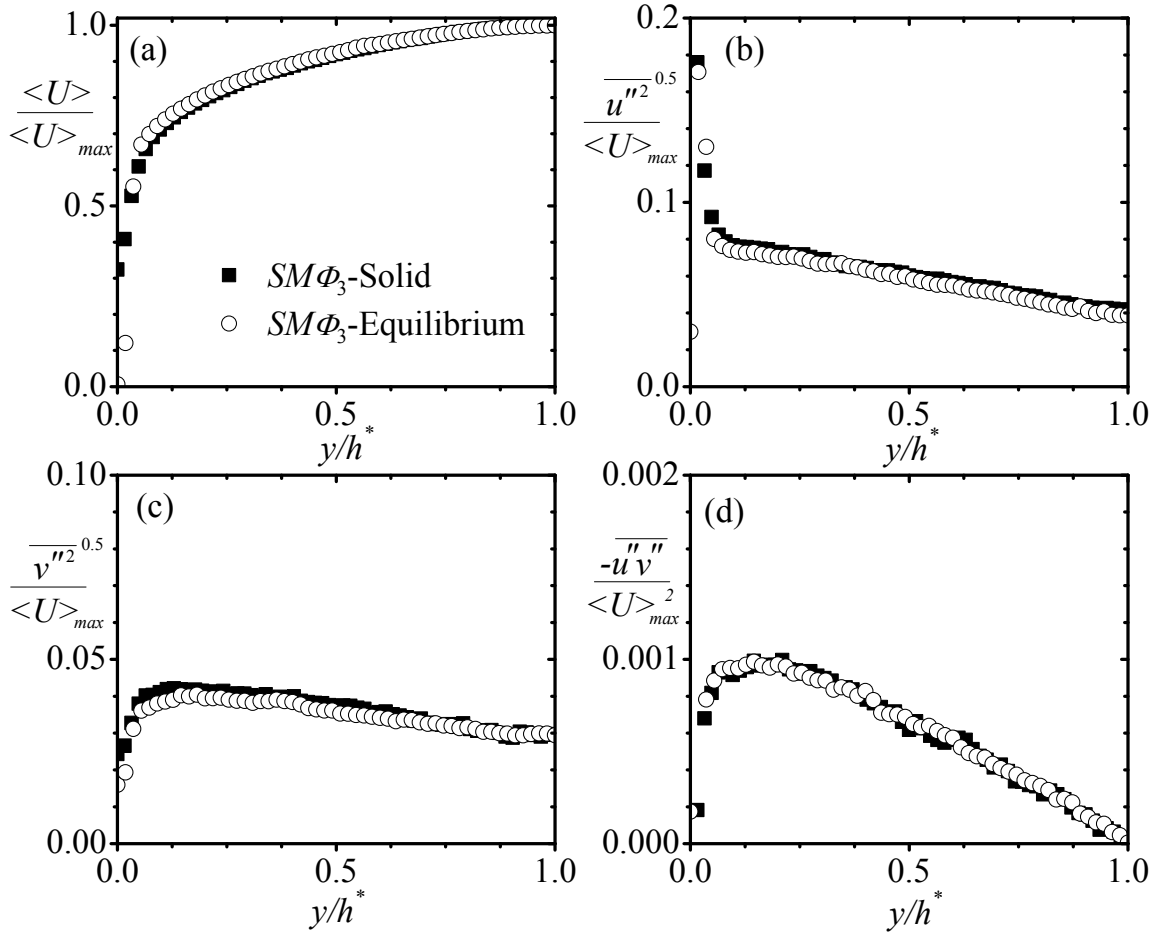

Figure 4.8: Comparison of solid phase profiles obtained from the measurements and by using the equilibrium approximation approach.

results is very good, providing new empirical support for the equilibrium Eulerian methodology.

4.4.2 Fluid Mean Velocity, Turbulent Intensities and Reynolds Shear Stress

Profiles of the fluid mean velocity, turbulence intensity and Reynolds shear stress are examined in figure 4.9. The fluid mean velocity is unaffected by particles over both the smooth and rough walls (figure 4.9a). In the rough wall flows, although the mean velocity values are reduced compared to the smooth wall, the additional enhancements observed

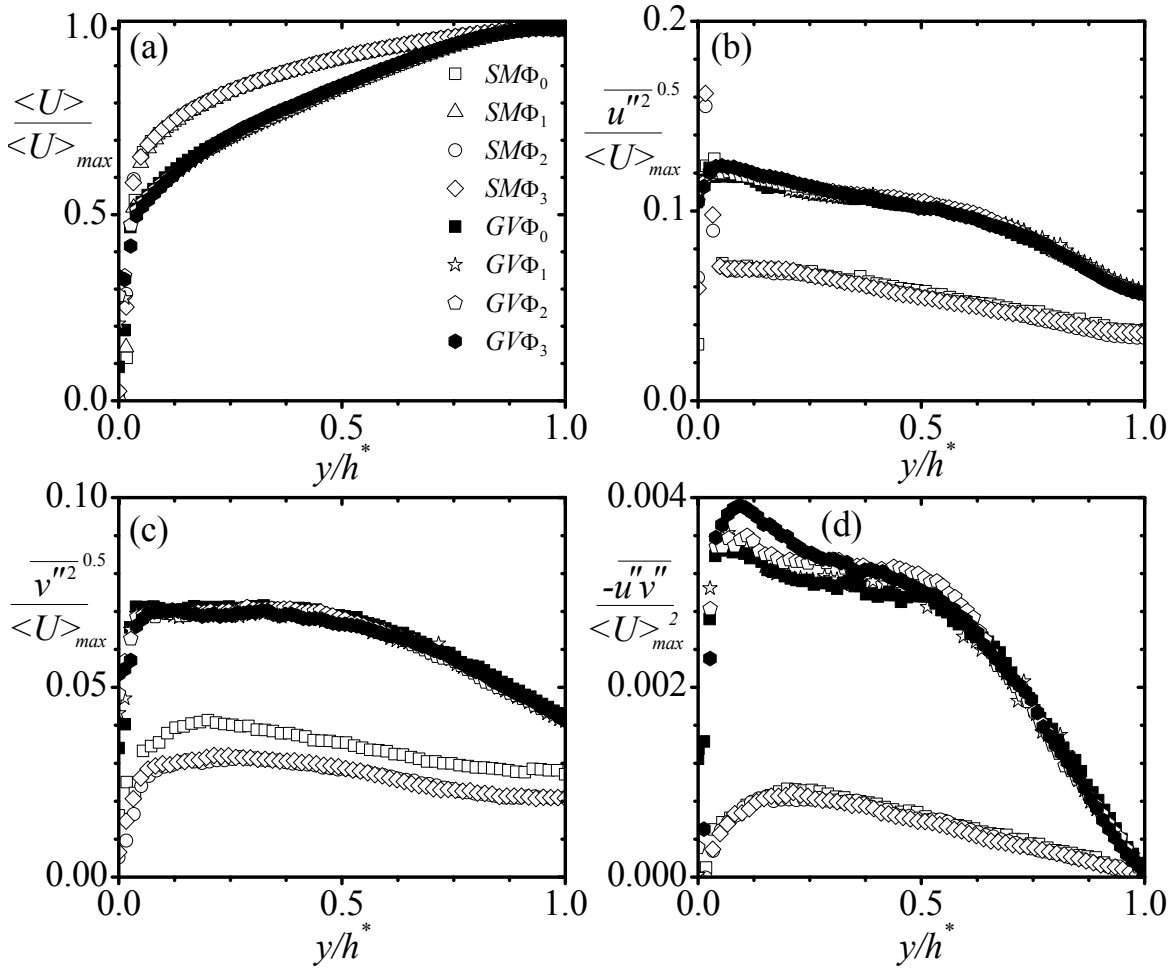

Figure 4.9: Profiles of the mean velocity, turbulent intensities and Reynolds shear stress of the carrier fluid.

for the solid phase with increasing loading ratio did not occur in this case. The streamwise turbulence intensity (figure 4.9b) also shows no sensitivity to the presence of particles over the smooth and rough walls. This can be attributed to the loss of streamwise momentum by particles as they settle towards the lower wall. Figure 4.9c shows that particles attenuate the fluid wall-normal turbulence intensity both near the wall and in the outer parts of the smooth channel flow. Over the rough wall, where the wall-normal turbulence intensities are considerably larger than the smooth wall values,

roughness collapsed the profiles. The Reynolds shear stress profiles over the smooth wall are nearly indistinguishable in spite of the reduction in the wall-normal turbulence intensity in the presence of particles. On the contrary, the rough wall profiles show enhancement in the presence of particles and the effect is seen to increase with increasing loading ratio.

The suppression of the fluid wall-normal turbulence intensities over the smooth wall may be attributed to the turbulence attenuation arising from a self-induced stratification of the particle concentration field. The streamwise turbulence intensities and Reynolds shear stress are unaffected because they are more closely associated with the larger-scale quasi-streamwise vortices. It is also plausible that for the Reynolds shear stress, any reduction over the smooth wall is offset by an improved correlation between the streamwise and wall-normal velocity fluctuations due to the presence of the particles. This effect is more dramatic over the rough wall so that the Reynolds shear stress is increased as the loading ratio increases. To examine the effects of particles and wall roughness on the correlation between the streamwise and wall-normal velocity fluctuations, values of the Reynolds shear stress correlation coefficient, $\rho_{-uv} = -\overline{u''v''} \Big/ \left(\overline{u''^2}\,\overline{v''^2}\right)^{0.5}$ can be compared as shown in figure 4.10. It should be noted that it is sufficient to use only the one-point correlation coefficient values due to its correspondence with the maximum value of the two-point cross-correlation between streamwise and wall-normal velocity fluctuation, R_{uv}. The results show that the correlation coefficient is enhanced in the presence of particles as well as over the rough wall. The rough wall values are also augmented with increasing loading ratio in a manner that is consistent with the trend in the Reynolds shear stress.

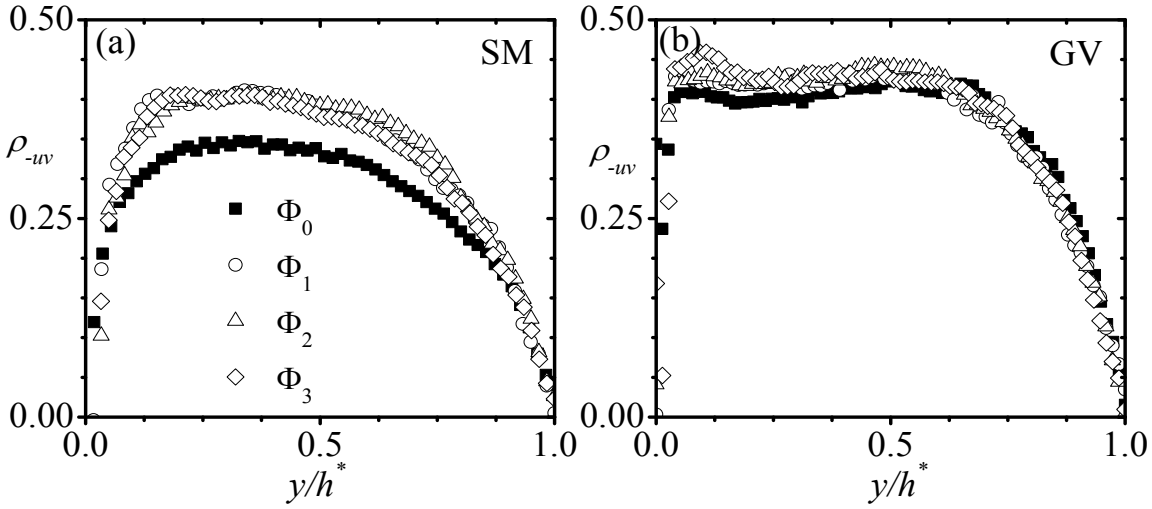

Figure 4.10: Profiles of the Reynolds shear stress correlation coefficient of the carrier fluid.

4.4.3 Quadrant Decomposition of the Reynolds Shear Stress

The hyperbolic hole method of Lu and Willmarth (1973) was used to decompose the fluid Reynolds shear stress into the four quadrants of the *u*-*v* plane. The values of the quadrant contributions were calculated based on a hyperbolic hole size, $H = 0$, for the unladen and the particle-laden flows. Figure 4.11 shows the distributions of the quadrant contributions normalized by $<U_{max}>^2$. The outward and inward interaction terms, shown in figures 4.11a and 4.11b, respectively, are predominantly negative and their magnitudes are negligibly small over the smooth wall. The magnitudes increase with wall roughness and more rapidly as the wall is approached, but for both the smooth and rough wall conditions no significant modification is observed in the presence of particles. The distributions of ejections (Q2) and sweeps (Q4) are shown in figures 4.11c and 4.11d, respectively. The plots indicate that the ejections and sweeps are the more dominant contributors to the mean Reynolds shear stress. The dramatically enhanced levels of ejections and sweeps

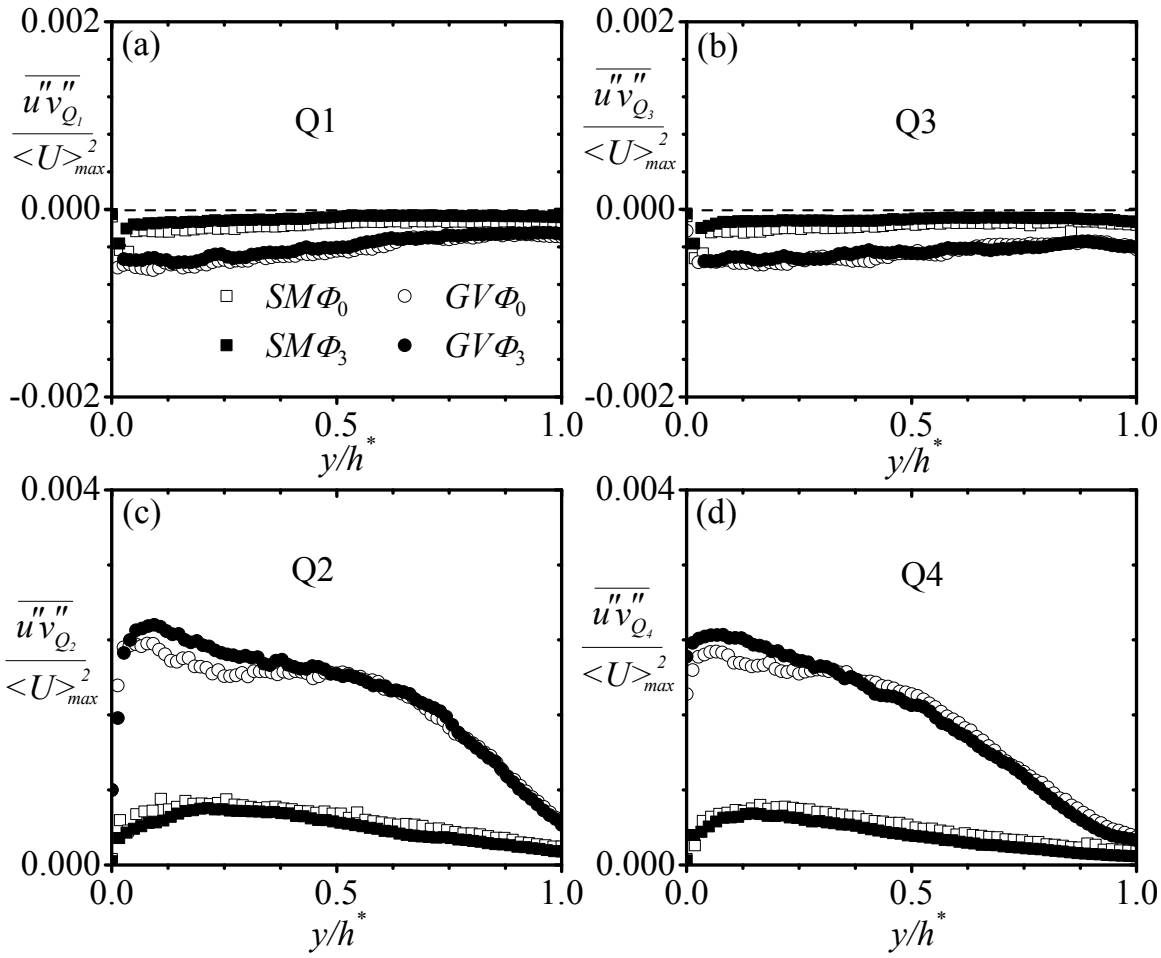

Figure 4.11: Quadrant decomposition of the carrier fluid Reynolds shear stress.

over the rough wall are consistent with the rapid increase in the Reynolds shear stress by the roughness perturbation. The rough wall results also reflect the additional disturbance introduced by particles in the form of promoting a more rapid increase in the Q2 and Q4 motions in the inner region.

Particle effects on the quadrant decomposition of the Reynolds shear stress have been examined in a number of particle-laden smooth wall studies. Kaftori et al. (1998), for instance, observed that large polystyrene particles ($d_p/L_e \approx 0.13$) increased Q3 and Q4 motions more strongly, with larger effects near the wall, while Q1 and Q2 motions

remained relatively unchanged. Because the large particles increased the Q4 motions more strongly than Q3, the authors observed larger Reynolds shear stress values in the wall region. The results presented by Righetti and Romano (2005) for small glass particles ($d_p/L_e \approx 0.02$ and $d_p/L_e \approx 0.04$) indicated enhancements of all four quadrant contributions near the wall and reduced contributions in the outer layer. As a result, the authors observed larger Reynolds shear stress values near the wall and smaller values in the outer layer. Borowsky and Wei (2011) who also used small glass particles ($d_p/L_e \approx 0.03$) reported no significant modification in the interaction terms, but particles dampened the ejections near the wall, enhanced them in the outer layer. The effect on sweeps was found to be opposite to that of ejections. The results of the present smooth wall decomposition do not exhibit any significant modification in the ejections and sweeps in comparison with the unladen values, which is consistent with the smooth wall Reynolds shear stress distributions.

4.4.4 Profiles of Swirling Strength

The statistics of swirling strength are now employed to characterize the impact of particles and roughness on the strength of the vortical structures. Figure 4.12a shows the profiles of the mean swirling strength (unsigned) over the smooth and rough walls. For a given surface, the mean swirling strength is unaffected by particles except in the wall region where damping occurs. For the unladen case, wall roughness has caused a considerable increase in the mean swirling strength over the entire half-channel region. Under loading conditions, while roughness can be described as enhancing the swirling strength, this increase by roughness is nullified by attenuation by particles in the wall

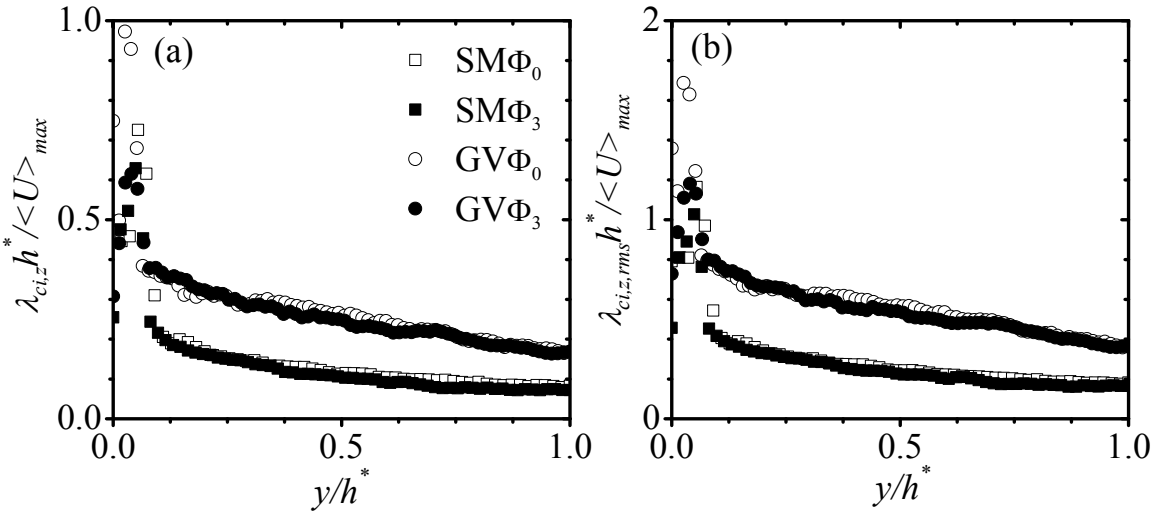

Figure 4.12: Profiles of the mean and root-mean-square swirling strength over the smooth wall and gravel roughness.

region. Figure 4.12b shows the effects of particles and roughness on the root-mean-square values of the unsigned swirling strength. These plots also show attenuation by particles in the wall region and enhancements in the presence of wall roughness. These results are in qualitative agreement with findings by Ahmed and Elghobashi (2000) and Dritselis and Vlachos (2011) that small particles attenuate the near wall vortices and reduce turbulence.

Figure 4.13 shows the decomposition of the signed swirling strength into its two components (prograde and retrograde swirling strength). Figures 4.13a and 4.13b show the fractions of prograde and retrograde swirling strength, respectively. These profiles are universal over most of the flow region ($y/h^* > 0.13$). This provides a rough indication that the flow structure in terms of the population of prograde and retrograde vortices remains essentially the same. Also, for most of the flow region, the proportion of prograde swirling strength is substantially larger than that of retrograde swirling strength, which

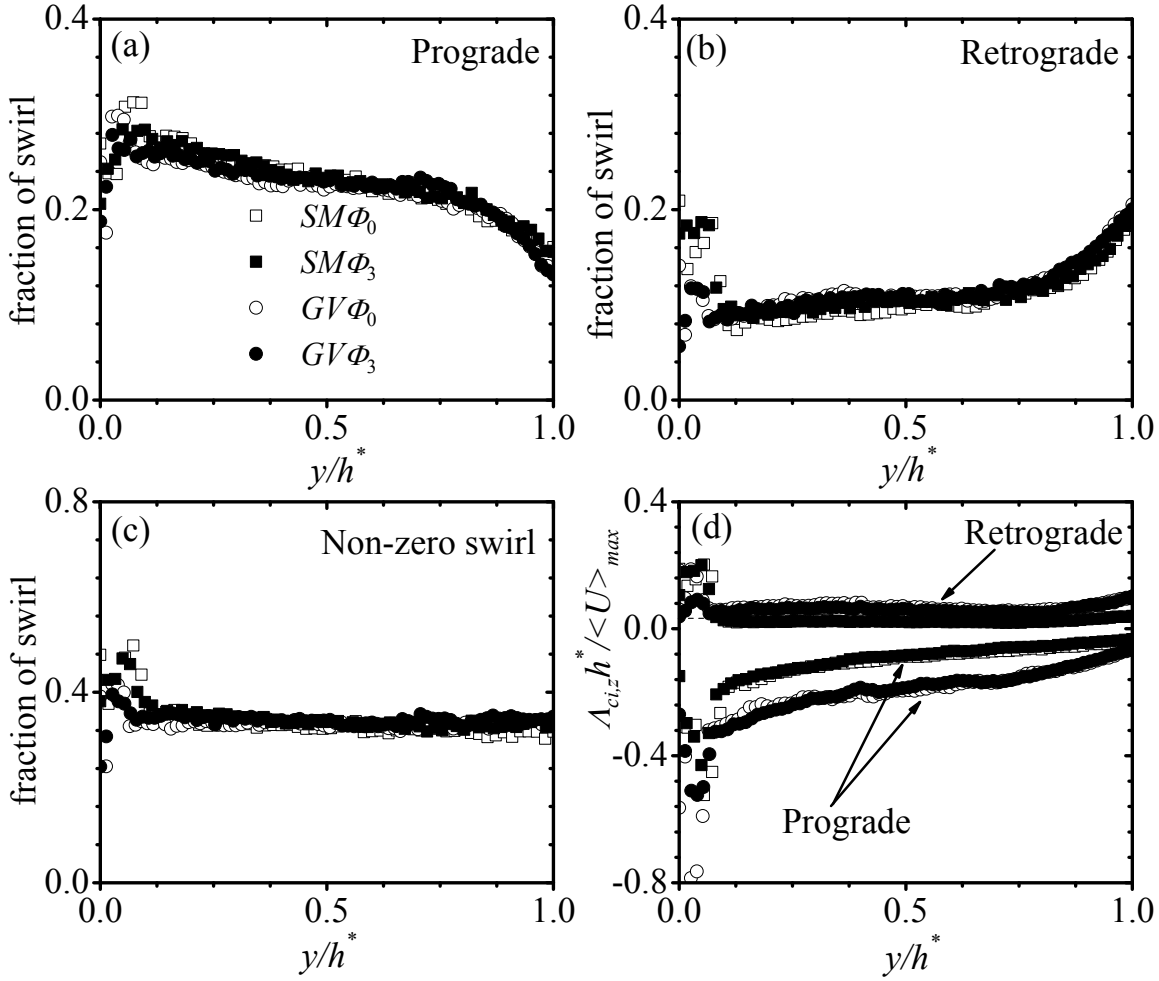

Figure 4.13: Profiles of the proportions of prograde, retrograde and non-zero swirl and their contribution to the mean swirling strength.

would imply that prograde vortex cores are the dominant vortical structures in these flows. Figure 4.13c shows the proportion of non-zero swirl, which is the union of progrades and retrogrades. This also shows universality over most of the half-channel region. However, because variations in the prograde and retrograde swirling fractions occur at nearly the same rate, the swirling strength is non-zero for about 35% of the time. These results are in qualitative agreement with similar distributions presented by Volino *et al*. (2007). Volino *et al.* (2007) who conducted measurements in turbulent boundary

layers over smooth and rough walls also found that the swirling strength was non-zero in the outer layer for about 30% of the time. Figure 4.13d shows the mean values of the swirling strength due to each component. The contribution of retrogrades is significant only in the immediate vicinity of the wall. This suggests the presence of positive swirl close to the wall, which is in agreement with previous observations (e.g., Jeong *et al.* 1997) that positively signed vortex cores appear near the wall due to the no-slip boundary condition. The contribution of prograde to the mean signed swirl is much larger than that of retrogrades and these are augmented by the wall roughness over most of the flow region. The larger values of the prograde swirling strength also reflects the predominance of the prograde vortex cores in the laden and unladen flows.

4.4.5 Two-Point Correlations of Velocity Fluctuations

Two-point correlations were calculated at selected wall-normal locations to investigate the spatial correlations between the velocity fluctuations. The two-point correlation, R_{AB}, between any two arbitrary quantities $A(x, y)$ and $B(x, y)$ was calculated as

$$R_{AB}\left(x_{ref}+\Delta x, y_{ref}+\Delta y\right)=\frac{\overline{A(x_{ref}, y_{ref})B(x_{ref}+\Delta x, y_{ref}+\Delta y)}}{\sigma_A(x_{ref}, y_{ref})\,\sigma_B(x_{ref}+\Delta x, y_{ref}+\Delta y)}, \qquad (4.26)$$

where the point (x_{ref}, y_{ref}) denotes the reference location, Δx and Δy are the spatial separations between A and B in the streamwise and wall-normal directions, respectively, and σ_A and σ_B are the root-mean-square values of A and B at (x_{ref}, y_{ref}) and ($x_{ref}+\Delta x$, $y_{ref}+\Delta y$), respectively. Figure 4.14 shows iso-contours of R_{uu} centred at $y/h^* = 0.15$. In each plot, the highest and lowest contour levels are respectively 0.9 and 0.5, and the contours are at intervals of 0.1. The iso-contours of R_{uu} are elongated in the streamwise direction

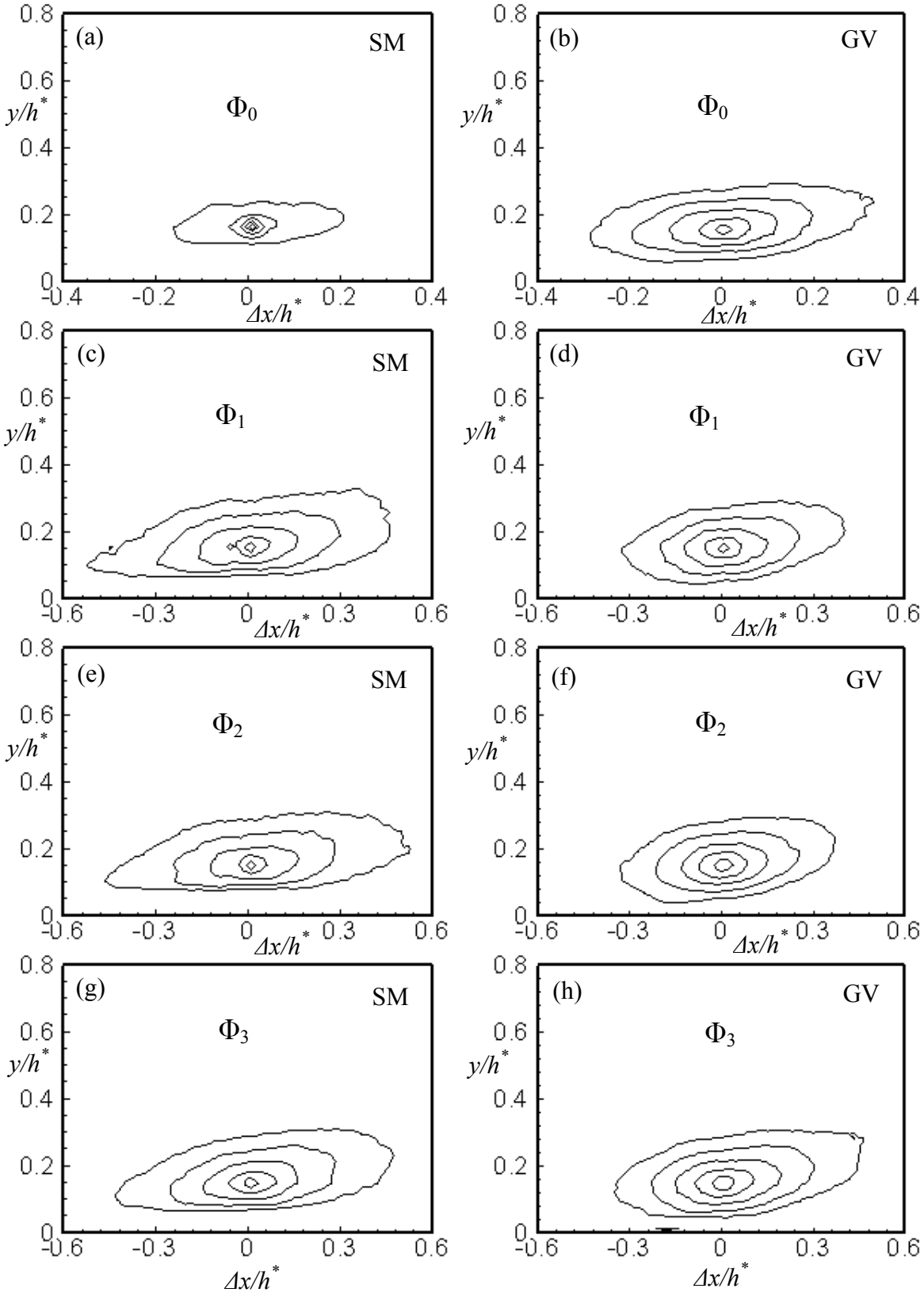

Figure 4.14: Iso-contours of the two-point correlation R_{uu} at $y_{ref}/h^* \approx 0.15$.

and have a relatively shallow streamwise inclination. The quasi-streamwise alignment of the R_{uu} correlation may be attributed to the convection of the wall structures by the mean flow and its inclination may be attributed to the tendency of wall ejections to lift the structures from the wall. On the other hand, contours of R_{vv} (not shown here) are generally compact and more rounded than R_{uu}, a feature that is attributable to the association between R_{vv} and the spanwise vortex cores.

Two-point correlations are often used to provide a rough indication of the average size and inclination of the wall structures. Hence, they were employed here to provide insight into the response of the turbulence structure to the presence of particles and surface roughness. To compare the average sizes of the larger and smaller scale structures, the spatial extents of the two-point correlations (R_{uu} and R_{vv}) contours were calculated. The wall-normal distributions of the streamwise and wall-normal extents of the correlations are shown in figure 4.15. Following Volino *et al.* (2009), the streamwise extent of R_{uu}, denoted here as Lx_{uu}, was estimated as twice the distance between the self-correlation peak and the most downstream point on the $R_{uu} = 0.5$ contour level. The wall-normal extent of R_{uu}, denoted as Ly_{uu}, was estimated as the wall-normal distance between points closest and furthest from the wall on the $R_{uu} = 0.5$ contour level. For R_{vv}, the spatial extents Lx_{vv} and Ly_{vv} were estimated as the streamwise and wall-normal distances, respectively, between the extreme points on the $R_{vv} = 0.5$ contour level. The plots presented in figures 4.15a-4.15d suggest a general increase in the spatial extents of the two-point correlations in the presence of particles and the rough wall. Because roughness and particles strongly influence the flow in the inhomogeneous (wall-normal) direction, the spatial extents of R_{vv} are more significantly enhanced, with a more dramatic effect in

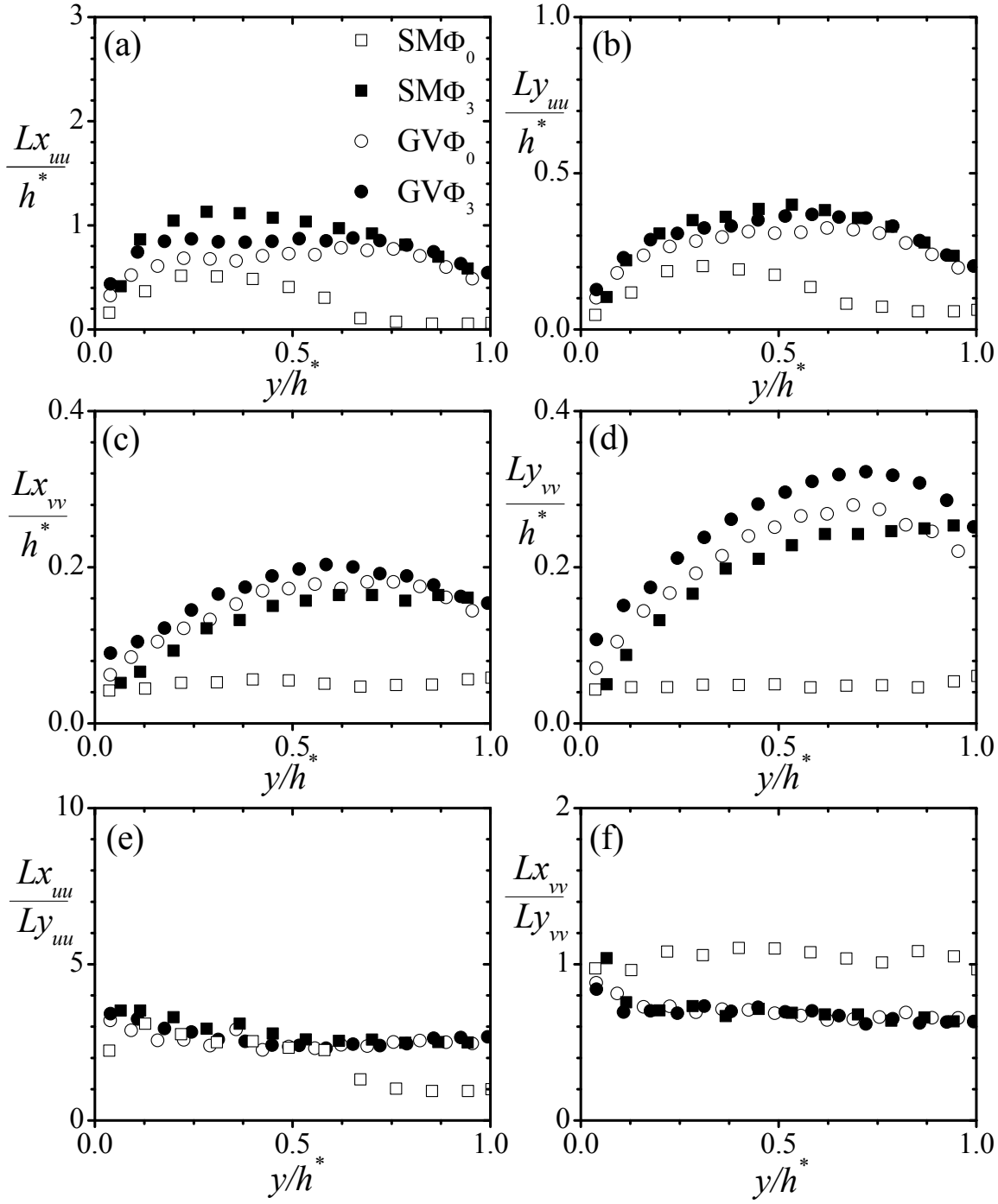

Figure 4.15: Profiles of the streamwise and wall-normal extents of the two-point correlations R_{uu} and R_{vv}.

values of Ly_{vv}.

The effects of the particles and roughness disturbances on the shape of the correlation contours are examined in figures 4.15e and 4.15f. The ratio of Lx_{uu} to Ly_{uu} is predominantly within the range 3.0 ± 0.3 for the rough wall and particle-laden flows, suggesting that in these cases, the R_{uu} contours are about three times larger in the streamwise direction than in the wall-normal direction. The ratio is closer to unity for the unladen smooth wall flow in the outer layer because the contours, being far away from the influence of the wall, became more rounded. The ratio of Lx_{vv} to Ly_{vv} is shown in figure 4.15f. The values of the ratio lie approximately within 1.0 ± 0.1 for the unladen smooth wall, which is in reasonable agreement with the value of $Lx_{vv}/Ly_{vv} \approx 1.3$ reported by Nakagawa and Hanratty (2001) for single-phase smooth channel flows. On average the level of Lx_{vv}/Ly_{vv} is reduced by about 30% in the presence of roughness and particles.

The increased spatial extents of R_{uu} and R_{vv} due to the particles and roughness disturbance may be explained by the observation in figures 4.4 and 4.5 that sedimenting particles and wall roughness induce significant fluid motion in the upward direction. The velocity fluctuations associated with these upward motions may contribute directly to the two-point correlations. The present smooth wall results are in good agreement with DNS results presented by Vreman (2007) and Dritselis and Vlachos (2011). Vreman (2007) computed the two point correlation function of the streamwise velocity fluctuation and found that the streamwise length scale is substantially increased in the presence of small particles. Dritselis and Vlachos (2011) whose observation was based on conditional average of the flow structure found that the mean coherent structure was larger in the presence of small particles.

Figure 4.16 shows the wall-normal distributions of the average inclination, β of

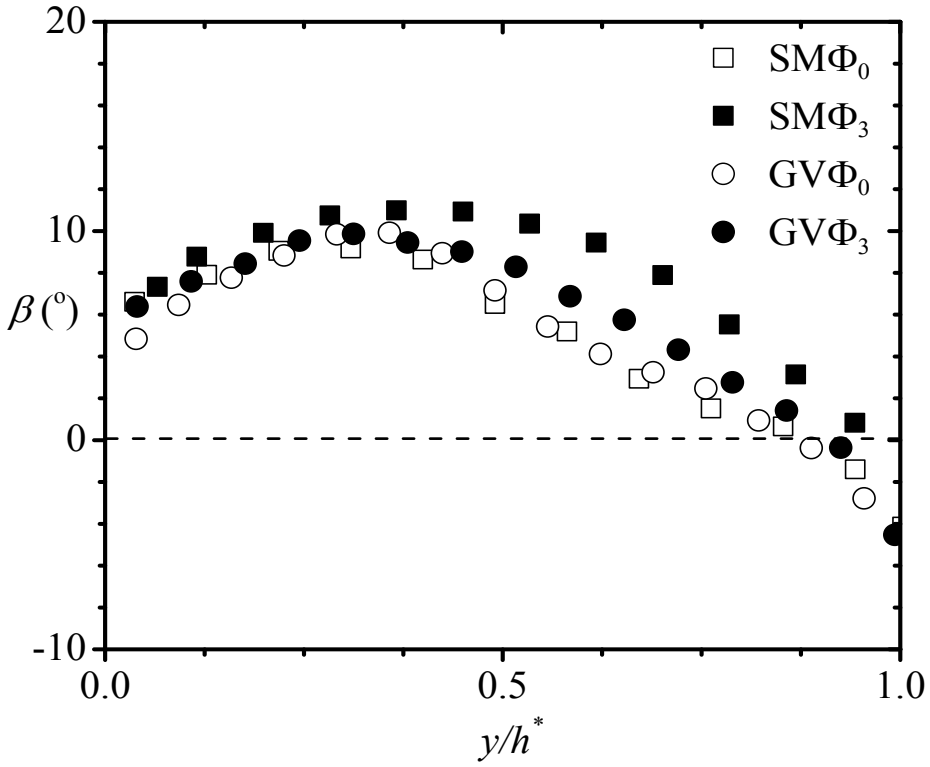

Figure 4.16: Profiles of the streamwise inclination of the two-point correlation R_{uu}.

R_{uu}. The values of β are often used to measure the average streamwise inclination of the larger-scale structures. Following Volino et al. (2009), the values of β were estimated by fitting a least-square line through the self-correlation peak of R_{uu} and the extreme points on the five contour levels: 0.9, 0.8, 0.7, 0.6 and 0.5. The curves are parabolic, which is a characteristic feature of turbulent channel flows. This shape is imposed by the property that the structures are smaller as the channel wall and core region are approached. The distributions reach peak values of approximately 10.0º ± 1.5º, which compare well with the values of 9º-12º obtained in previous unladen turbulent channel investigations (e.g., Jeong et al. 1997; Nakagawa and Hanratty 2001; del Álamo et al. 2006). Roughness and particle effects are important only in the outer region, and these are respectively, to

promote and delay the decay of values in the outer region. The negative values in the core region correspond to contours whose reference locations, y_{ref}/h^* are below the centres of the structures producing the correlation.

4.4.6 Two-Point Correlations of Velocity Fluctuations and Swirling Strength

In order to examine the relationship between the velocity fluctuations and the spanwise vortex cores, which have been observed earlier to be predominantly prograde vortex cores, two-point correlations between the velocity fluctuations and swirling strength, $R_{\lambda u}$ and $R_{\lambda v}$, were calculated at selected wall-normal locations. In calculating $R_{\lambda u}$ and $R_{\lambda v}$, the unsigned swirling strength $\lambda_{ci,z}$ was used so that $R_{\lambda u}$ and $R_{\lambda v}$ retain the signs of the velocity fluctuations u and v, respectively. In the streamwise–wall-normal plane, if a prograde vortex is the dominant vortex at the reference location, $R_{\lambda u}$ is positive above the reference point and negative below the reference point, while $R_{\lambda v}$ is positive upstream of the reference point and negative downstream of the reference point. Physically, the two-point correlations provide an indication of the average spatial extent and strength of the velocity field associated with the vortex. Figure 4.17a shows the iso-contours of the $R_{\lambda u}$ at $y/h^* = 0.15$ for the unladen smooth wall ($SM\Phi_0$). The magnitudes of the contours are 0.00, 0.04, 0.06, 0.08 and 0.10. These contours are qualitatively consistent with those presented by Christensen and Adrian (2001) for a fully developed channel flow. The positive $R_{\lambda u}$ values above the reference location and the negative values below the reference location are consistent with the flow pattern around a prograde vortex core whose direction of rotation is clockwise. It has been suggested that when the vortex core is part of a coherently aligned group (or packet) of vortices, the correlation extends along

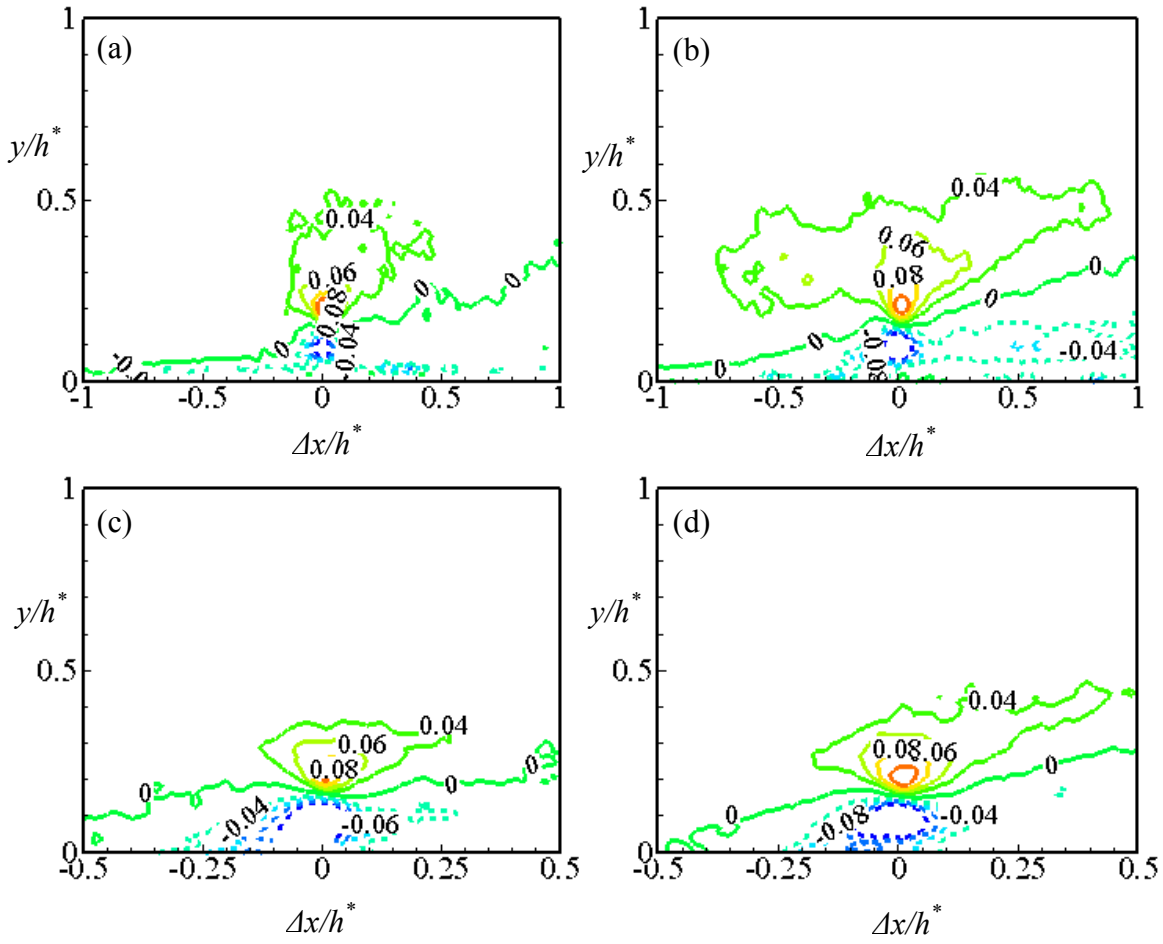

Figure 4.17: Two-point correlations of swirling strength and the streamwise velocity fluctuation, $R_{\lambda u}$, at $y_{ref}/h^* = 0.15$. (a) SMΦ$_0$, (b) SMΦ$_3$, (c) GVΦ$_0$, (d) GVΦ$_3$. Contour levels are 0.00, 0.04, 0.06, 0.08 and 0.10. Dashed lines denote negative correlations.

the packet. This is demonstrated by the zero-contour level. Since $\lambda > 0$, the contour level $R_{\lambda u} = 0$ connects the regions in the flow where negative u- and positive u-motions (i.e., Q2/Q4 events) of equal magnitude converge to produce $u = 0$. This region of stagnation flow also corresponds to the inclined edge of the shear layer associated with the prograde vortex. A line fit through the points on the $R_{\lambda u} = 0$ contour level yielded an average inclination angle of approximately 10º, which is consistent with the angle extracted from the streamwise velocity auto-correlation function, R_{uu}, at this location. Figure 4.17b

shows the corresponding contours of $R_{\lambda u}$ for the particle-laden case ($SM\Phi_3$). The spatial extents of both the positive and negative correlations are larger in the presence of the particles compared to the unladen flow. Iso-contours of $R_{\lambda u}$ over the unladen and particle-laden rough wall, $GV\Phi_0$ and $GV\Phi_3$, are shown in figures 4.17c and 4.17d, respectively. The contours are qualitatively similar to those observed over the smooth wall.

The iso-contours of the correlations in the outer layer are shown in figure 4.18 for the smooth and rough wall flows at $y/h^* = 0.4$. In the outer layer, the correlations are predominantly negative, indicating that ejection-like (Q2) motions are the dominant motions associated with the prograde vortex cores for both the unladen and particle-laden flows. However, the ejections are more strongly correlated with the vortices for the particle-laden flows than the unladen flows. It is interesting to note that when corresponding plots of figure 4.18 are superimposed over those of figure 4.17, the resulting flow field presents the appearance of regions of alternating positive and negative fluctuating streamwise velocity. This is in concert with the presence of uniform momentum zones detected by Adrian et al. (2000a) in a Galilean transformation of the streamwise velocity field.

Figure 4.19 shows the iso-contours of $R_{\lambda v}$ at $y/h^* = 0.15$. The contours are much smaller than the $R_{\lambda u}$ contours because the v-fluctuations are more localized in space than the u-fluctuations. Nevertheless, the positive values of $R_{\lambda v}$ on the left of the reference location and the negative values on the right of the reference location are consistent with their $R_{\lambda u}$ counterparts, reflecting the Q2/Q4 flow signature around the prograde vortices at this location. The rough wall $R_{\lambda v}$ correlations are more rounded and in closer contact with the wall than the smooth wall correlations, which speaks to the higher intensity of

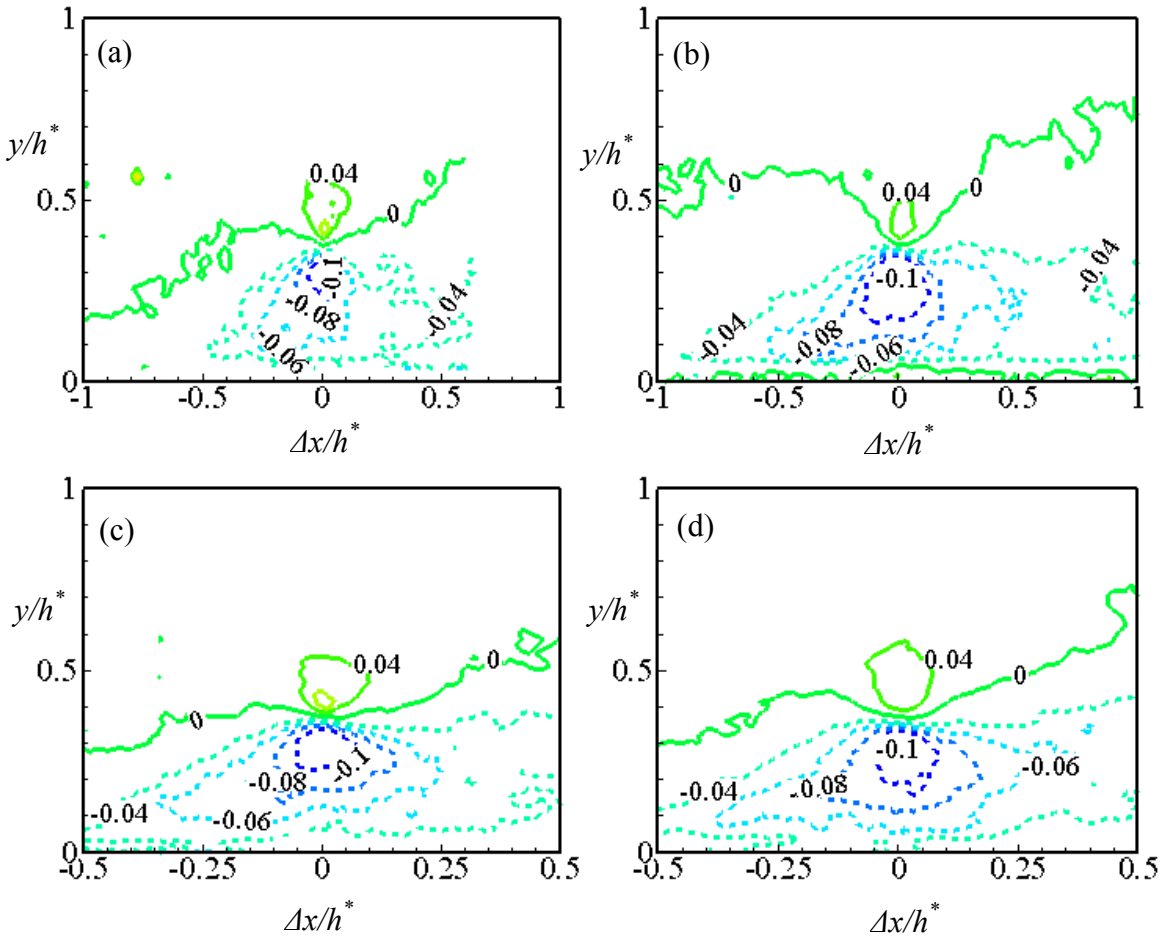

Figure 4.18: Two-point correlations of swirling strength and the streamwise velocity fluctuation, $R_{\lambda u}$, at $y_{ref}/h^* = 0.4$. (a) SMΦ$_0$, (b) SMΦ$_3$, (c) GVΦ$_0$, (d) GVΦ$_3$. Contour levels are 0.00, 0.04, 0.06, 0.08 and 0.10. Dashed lines denote negative correlations.

vortices (swirling strength) over the rough wall. The outer layer $R_{\lambda v}$ correlations are shown in figure 4.20. The positive values of $R_{\lambda v}$ are significantly wider than the negative correlations, in agreement with the more dominant ejections in the outer layer. The positive correlations also have a much wider spatial extent in the presence of particles when compared to the unladen flow due to the induced upward flux of fluid by the particles.

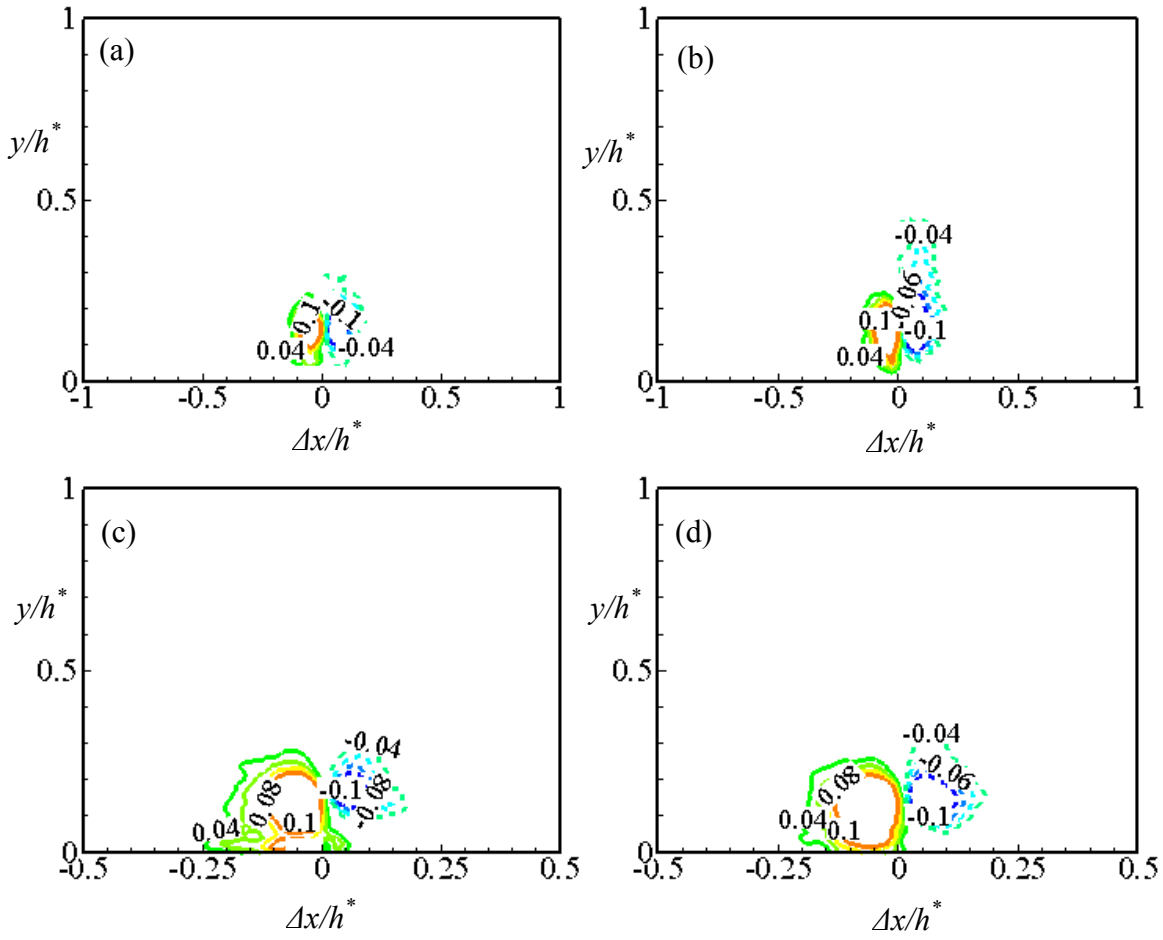

Figure 4.19: Two-point correlations of swirling strength and the streamwise velocity fluctuation, $R_{\lambda v}$, at $y_{ref}/h^* = 0.15$. (a) SMΦ$_0$, (b) SMΦ$_3$, (c) GVΦ$_0$, (d) GVΦ$_3$. Contour levels are 0.00, 0.04, 0.06, 0.08 and 0.10. Dashed lines denote negative correlations.

The observed characteristics of the two-point correlations (both between the velocity fluctuations, and between the velocity fluctuations and swirling strength) can be considered as the statistical imprints of attached and detached eddies. The concept of attached eddies was first introduced by Townsend (1976) who remarked that the eddies that contribute strongly to the Reynolds shear stress at a given wall-normal height, y, scale with that height and are therefore in a sense attached to the wall. Perry and Chong (1982) in an extensive analytical investigation proposed a model of the turbulent

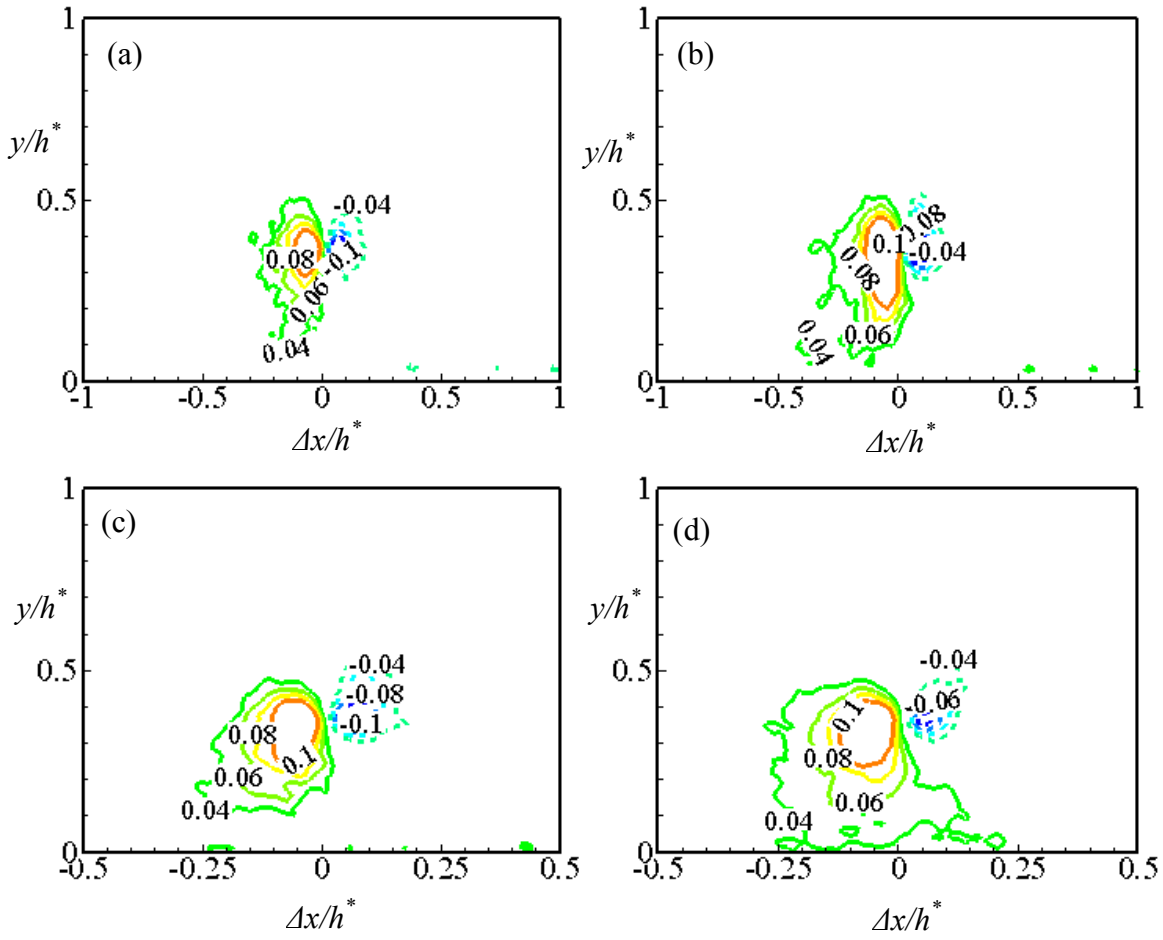

Figure 4.20: Two-point correlations of swirling strength and the streamwise velocity fluctuation, $R_{\lambda v}$, at $y_{ref}/h^* = 0.4$. (a) SMΦ$_0$, (b) SMΦ$_3$, (c) GVΦ$_0$, (d) GVΦ$_3$. Contour levels are 0.00, 0.04, 0.06, 0.08 and 0.10. Dashed lines denote negative correlations.

boundary layer consisting of attached eddies whose size grows in proportion to their distance from the wall in a self-similar manner. When separated from the wall, they are considered as detached eddies according to the formulation by Perry and Marušić (1995) where they are thought to be responsible for the outer layer structure. In the present work, the larger extents of the spatial correlations in the particle-laden and rough wall flows (figure 4.15) provide an indication of structure growth across the flow region. The results also suggest that in the particle-laden and rough wall cases, the velocity fluctuations at a

given height, y_{ref}, are more likely to be correlated with the near wall flow than over the unladen smooth wall. Thus, the presence of wall roughness and particles may be envisaged as creating a direct connection between the outer and inner layers. As noted in previous turbulent boundary layer investigations (e.g., Hutchins et al. 2005; Volino et al. 2009) and fully developed channel flows (e.g., Tay et al. 2015), for the unladen smooth walls, beyond a certain y_{ref}, the structures simply lift off from the wall to become detached eddies, thus breaking the communicative link between the fluctuations at y_{ref} and those near the wall. This would result in smaller extents of the two-point correlations for reference locations in the outer layer (as was observed for the unladen smooth wall, $SM\Phi_0$).

The larger structures in the particle-laden and rough wall flows can be seen therefore as enhancing the outer and inner layer interaction. This has important implications for wall-layer turbulence models such as the attached/detached eddy hypothesis and LES wall shear stress models that are based on the assumption that the outer layer is detached from the inner layer. In most LES of the turbulent boundary layers, for instance, the wall boundary condition requires the specification of the instantaneous filtered wall shear stress based on the filtered velocity at the closest grid point from the wall. In order to replicate the near-wall dynamics such as the streamwise inclination of the coherent structures, the filtered instantaneous velocity is shifted in the streamwise direction by an amount Δl, which can be obtained from either experiments or DNS. The value of this shift is also sometimes estimated using the relation, $\Delta l = (1 - |y|)\cot\theta$ (Piomelli et al. 1989), where θ is the inclination angle of the correlation between the wall shear stress and the streamwise velocity. For values of y^+ within $30 < y^+ < 50$-

60, $\theta \approx 8^{o}$ is used, while at larger distances from the wall, θ is taken to be approximately equal to 13º, which is comparable to the inclination angle of the streamwise velocity fluctuation auto-correlation, R_{uu}, in the logarithmic region. Contrary to fully developed channel simulations that rely on the log region value of the R_{uu} inclination angle (i.e., $\beta \approx$ 13º) for the outer layer computations, the present results indicate a functional dependency of β (or θ) on y/h^{*}.

4.4.7 Linear Stochastic Estimation of the Velocity Fields

The swirling strength and two-point correlation results have shown a high prevalence of prograde vortex cores over the smooth and rough walls. To determine the average flow structure associated with these vortex cores, conditional averages of the flow fields were calculated using the linear stochastic estimation technique. Figure 4.21 presents vector plots of the linear stochastic estimate of the conditionally averaged flow fields given a prograde vortex core at $y/h^{*} = 0.36$. In each plot, a solid circle is used to mark the event location. As is often done (e.g., Christensen and Adrian 2001), the velocity vectors in the plots were set to unit magnitude to prevent the obscuring of weaker motions away from the event. The event vortex lies along a crease in the velocity field inclined at a shallow angle from the wall. This crease or ridge-like feature is common to all four flow fields although it is more sharply defined in the rough wall and particle-laden flows. The crease marks the inclined edge of the shear layer associated with the vortex. The shear layers present the appearance of large-scale coherent regions of Q2 motions emanating from the wall. Similar structures have been observed in previous single-phase wall-bounded investigations over smooth surfaces (e.g., Johansson et al. 1991; Christensen and Adrian

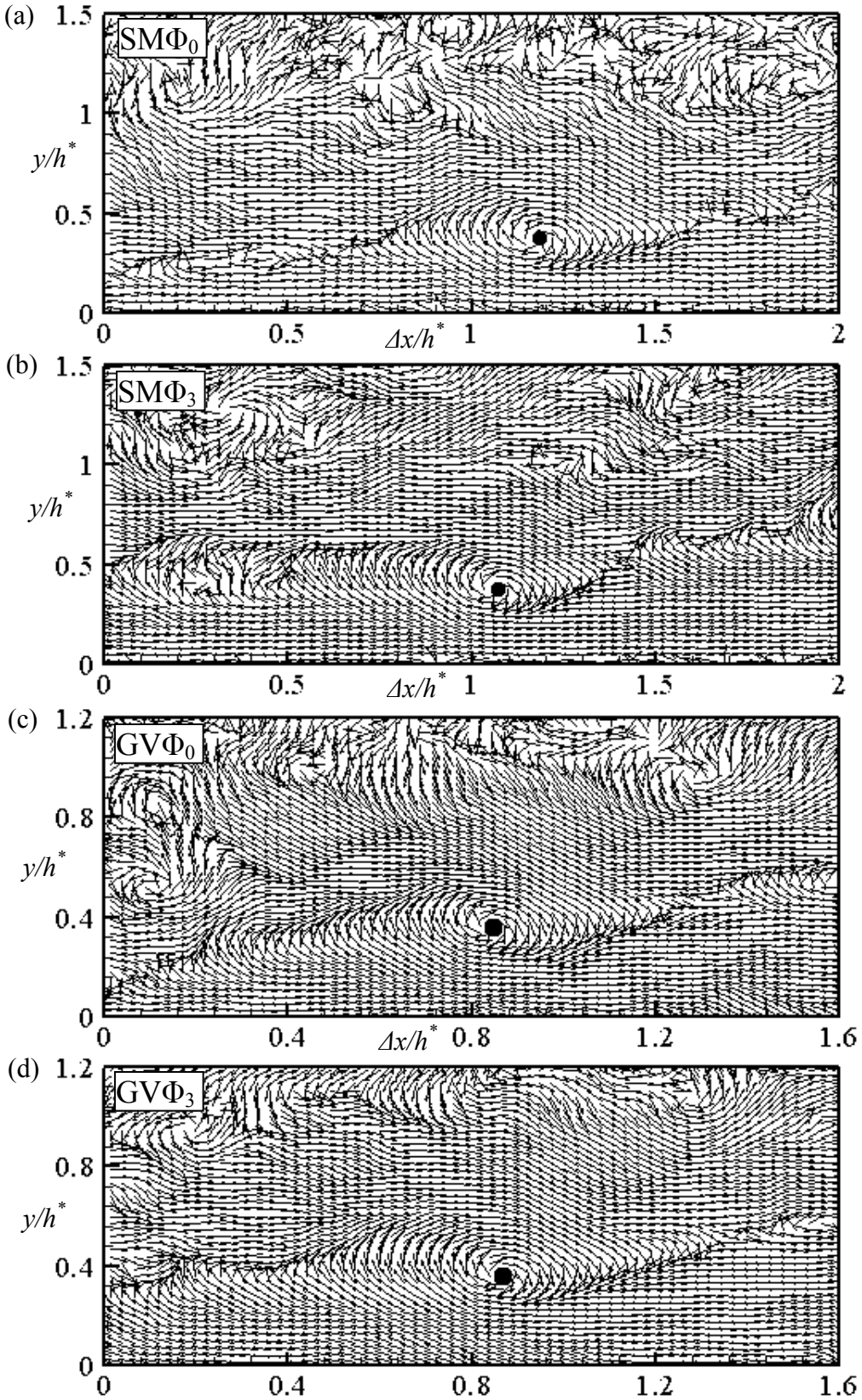

Figure 4.21: LSE of the velocity fields given a prograde vortex at $y_{ref}/h^* = 0.36$.

2001; del Álamo et al. 2006), and over rough walls (e.g., Volino et al. 2009; Tay et al. 2013). In the literature, their presence is often related to the combined action of smaller-scale vortices. Adrian et al. (2000a), for instance, suggested that they may be attributed to the coherent alignment of hairpin-like vortices that cooperatively produce regions of induced backflow against the mean flow. This viewpoint was confirmed by conditional average results obtained by Klewicki and Hirschi (2004) that showed a strong spatial correlation between the shear layers and clusters of spanwise vortices. Contrary viewpoints have also been offered in the literature, including their generation from the instability of low speed streaks (Schoppa and Hussain 2002), from the merger among neighbouring low speed streaks (Brandt and de Lange 2008), or as a direct result of the geometric constraints imposed by solenoidality of the vorticity field (Klewicki 1997). Nevertheless, the inclined shear layers have been identified to be dynamically significant in the production of the largest fraction of the turbulent kinetic energy and Reynolds shear stress (Johansson et al. 1991; Na et al. 2001).

4.5 POD of the Velocity Fields

The POD method was applied to both the fluctuating and total velocity fields to assess the contributions of the larger-scale structures to the fluid kinetic energy. Decomposition of the velocity fluctuations provides insight into the relative contributions of the various POD modes to the fluid turbulence kinetic energy (TKE). On the other hand, a POD of the total velocity field, where the correlation kernel is formed from the instantaneous velocities, instead of the fluctuations, offers one way of reconstructing the mean flow.

Table 4.2: Percentage contributions of the first POD mode to the resolved turbulent kinetic energy for increasing number of snapshots.

N	$SM\Phi_0$ (λ_1/E)	$SM\Phi_3$ (λ_1/E)	$GV\Phi_0$ (λ_1/E)	$GV\Phi_3$ (λ_1/E)
10	21.672	21.303	27.288	25.425
50	12.760	14.389	17.647	16.115
100	10.963	11.747	14.115	16.921
200	11.718	12.327	13.424	17.193
500	9.802	12.015	15.262	16.769
700	9.808	12.466	15.107	16.978
1000	9.890	12.834	14.646	17.514
1500	9.695	12.615	14.299	16.857
2000	9.664	12.758	14.171	16.693
2500	9.520	13.150	13.666	16.892
3000	9.349	13.287	13.564	16.534

4.5.1 POD of the Fluctuating Velocity Fields

For the POD, a convergence test was first carried out in order to determine the number of snapshots necessary to capture the largest fraction of the turbulent kinetic energy. The percentage contributions of the most dominant POD mode (λ_1/E) are summarized in Table 4.2 for $10 \leq N \leq 3000$, where N is the number of snapshots. The variation of λ_1/E down each column is non-monotonic, although a general tendency to decrease with N is observed. The energy of mode 1 would decrease generally because as N increases the total energy (which remains the same) is shared among more POD modes. In the present analysis, the unladen and particle-laden smooth wall ($SM\Phi_0$ and $SM\Phi_3$) contributions fall within (10.0 ± 2.0)% and (12.0 ± 1.5)%, respectively, for $N \geq 100$. The rough wall contributions are within (14.5 ± 1.0)%, and (15.5 ± 1.8)%, for $GV\Phi_0$ and $GV\Phi_3$, respectively, for $N \geq 100$. The present unladen smooth wall results are in qualitative

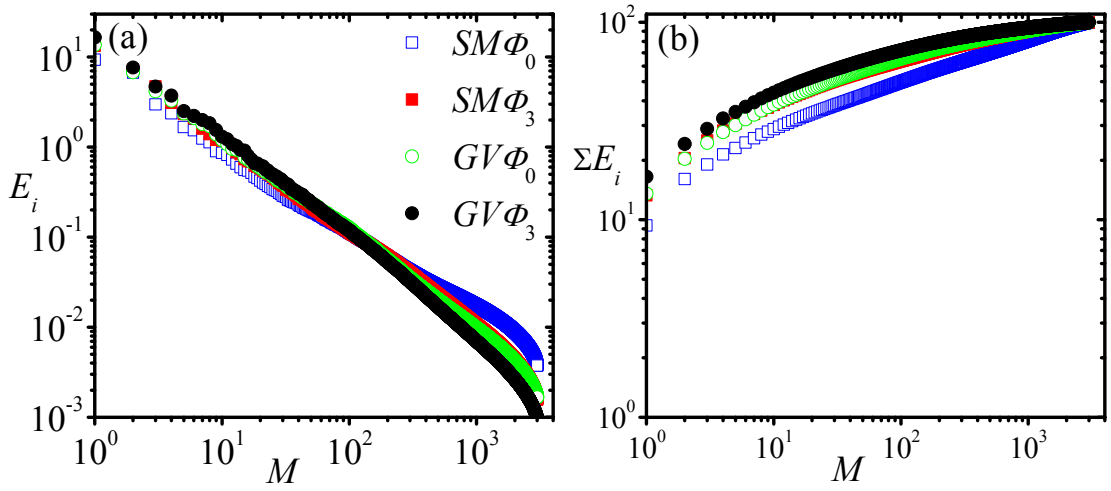

Figure 4.22: Eigenvalue spectra and cumulative energy distributions based on the POD ($N = 3000$) of the smooth and rough wall fluctuating velocities.

agreement with previous single-phase canonical applications of the POD (e.g., Reichert et al. 1994; Kostas et al. 2005). The present increase of the fractional contribution of Mode 1 with wall roughness is also consistent with previous rough wall experiments (e.g., Wu and Christensen 2010). Figure 4.22a compares the eigenvalue spectra of the four test cases based on the decomposition of 3000 snapshots. The plots show that the first few modes ($M \leq 50$) captured more of the total tke over the rough wall and with particles than the unladen smooth wall flow ($SM\Phi_0$). As a result, there is a crossover at $M = 200$, say, where it is seen that the unladen smooth wall spectra outstrips the others. That is to say, the smaller scales in $SM\Phi_0$ still retain a substantial amount of the total TKE compared to particle-laden and rough-wall flows. These results also show that the energy converges more rapidly for the particle-laden and rough wall flows than the unladen smooth wall flow. This is not unexpected since both particles and wall roughness enlarged the size of the structures. Figure 4.22b, which shows the cumulative energy distributions, confirms that the energy converges much faster over the rough wall and with particles.

4.5.2 POD of the Total Velocity Fields

With the POD (temporal) coefficients, $a_n(t)$ and eigenfunctions, $\Phi^n(x, y)$, calculated from the instantaneous total velocities, an instantaneous mean velocity can be reconstructed based on the first M modes given by (Druault and Chaillou 2007):

$$U(x,y,t) = \sum_{n=1}^{M} a_n(t)\Phi^n(x,y) \tag{4.27}$$

The mean velocity is finally recovered from a summation of the instantaneous values, which mathematically is equivalent to

$$\overline{U(x,y)} = \sum_{n=1}^{M} \overline{a_n}\,\Phi^n(x,y) \tag{4.28}$$

where the overbars denote ensemble averaging.

It should be noted, however, that in order to use equation (4.28), the cut-off value of M that separates the mean flow field from the fluctuating component must be determined. One approach suggested by Druault and Chaillou (2007) is to infer the value of M from the distribution of the root-mean-square values of the temporal coefficients. Figure 4.23 shows the distributions of the first and second POD coefficients of the total field plotted versus time. These plots indicate that the POD coefficient is a fluctuating quantity. It can be seen that for Mode 1, all the values are positive. The rough wall coefficients fluctuate about mean values that are approximately one-half of those over the smooth wall. This is proportionate with the relationship between the maximum streamwise mean velocities of $U_{max} \approx 1.0$ m/s and 0.5 m/s, respectively, over the smooth wall and the gravel roughness. With increasing order of modes, the distributions fluctuate between positive and negative values. At a sufficiently high order, the distributions acquire the character of the velocity fluctuations so that the mean values $\overline{a_n} \approx 0$.

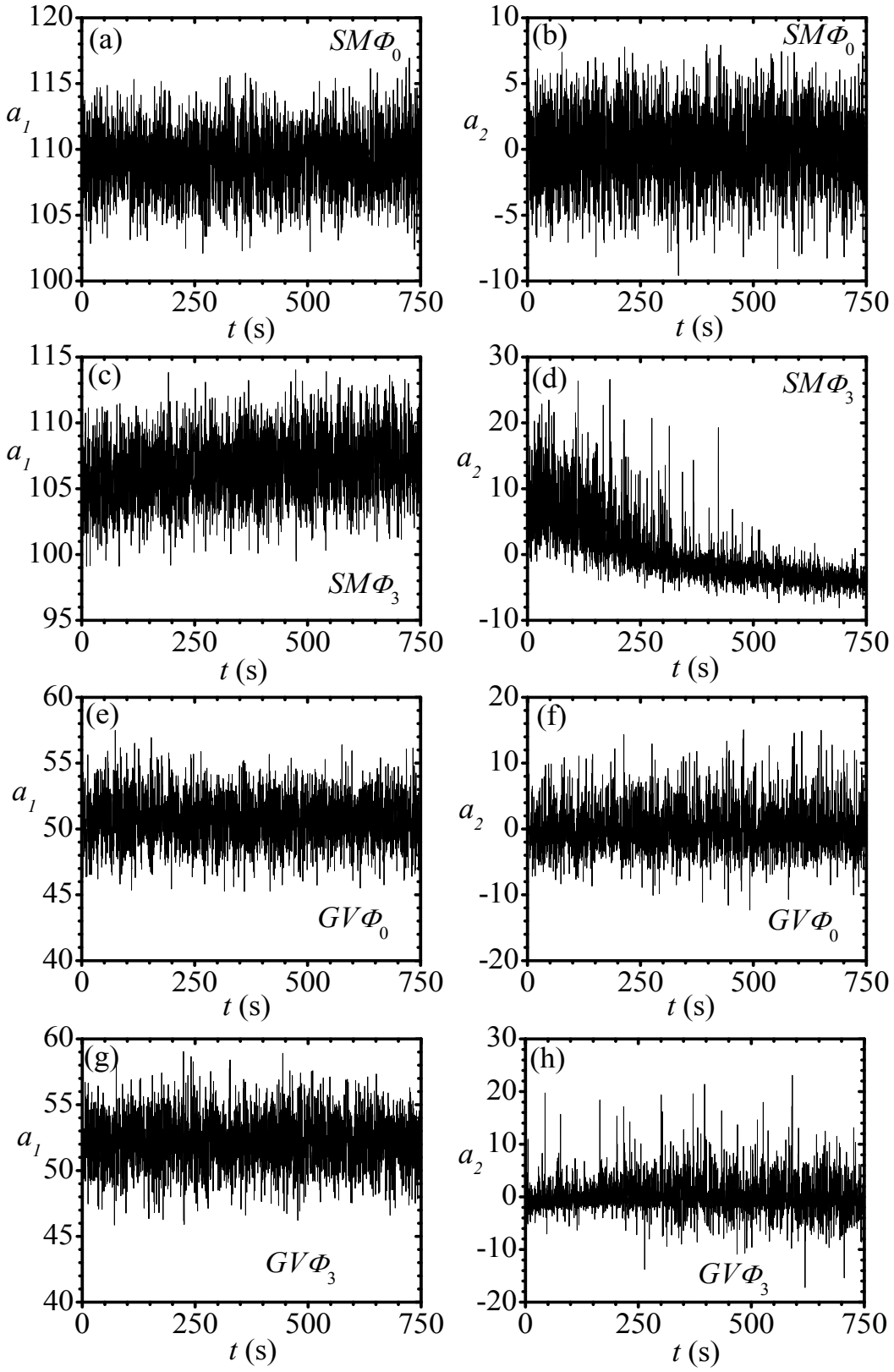

Figure 4.23: Temporal coefficients of the first and second modes of the POD (N = 3000) of the total velocity field.

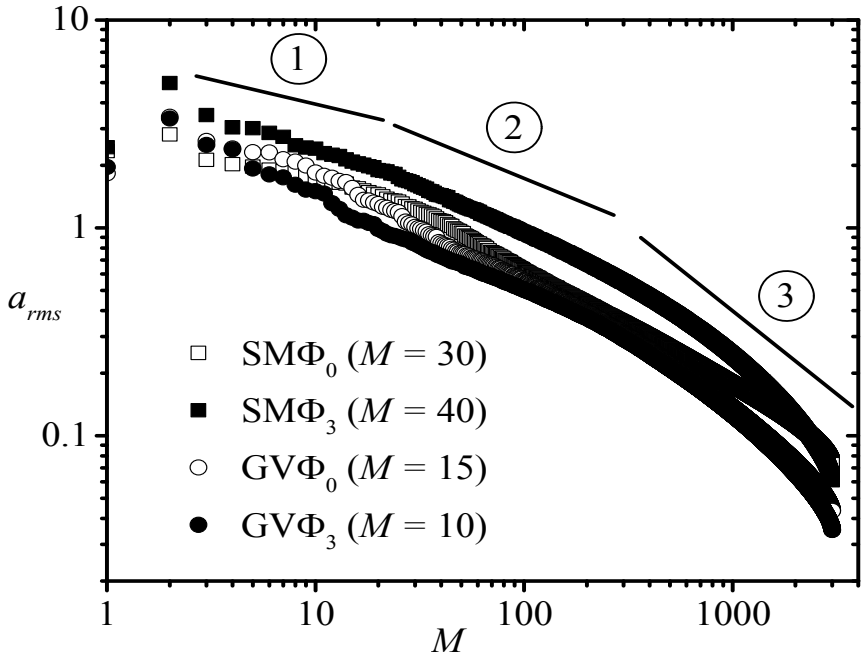

Figure 4.24: Spectra of the root-mean-square temporal coefficients from the POD of the total velocity field.

Figure 4.24 shows the spectra of temporal coefficients for the four test cases. As shown, the curves can be divided into three separate regions of increasing slope, indicating similarity with the energy spectral density distributions reported in previous wall-bounded flows. It was found that using the range of values of M extending from $M = 1$ to the end of region (1) reproduces the mean velocity profiles fairly well. These values of M are enclosed in parenthesis in the figure. Profiles of the reconstructed streamwise mean velocity are presented in figure 4.25. The original (concentration-coupled) mean velocity distributions are also included for reference. The POD reconstructed profiles are in excellent agreement with those calculated by the volume fraction-weighted averaging method for all the test cases. These results demonstrate the applicability of the POD as a tool for reconstructing the mean velocity field from a set of non-stationary data.

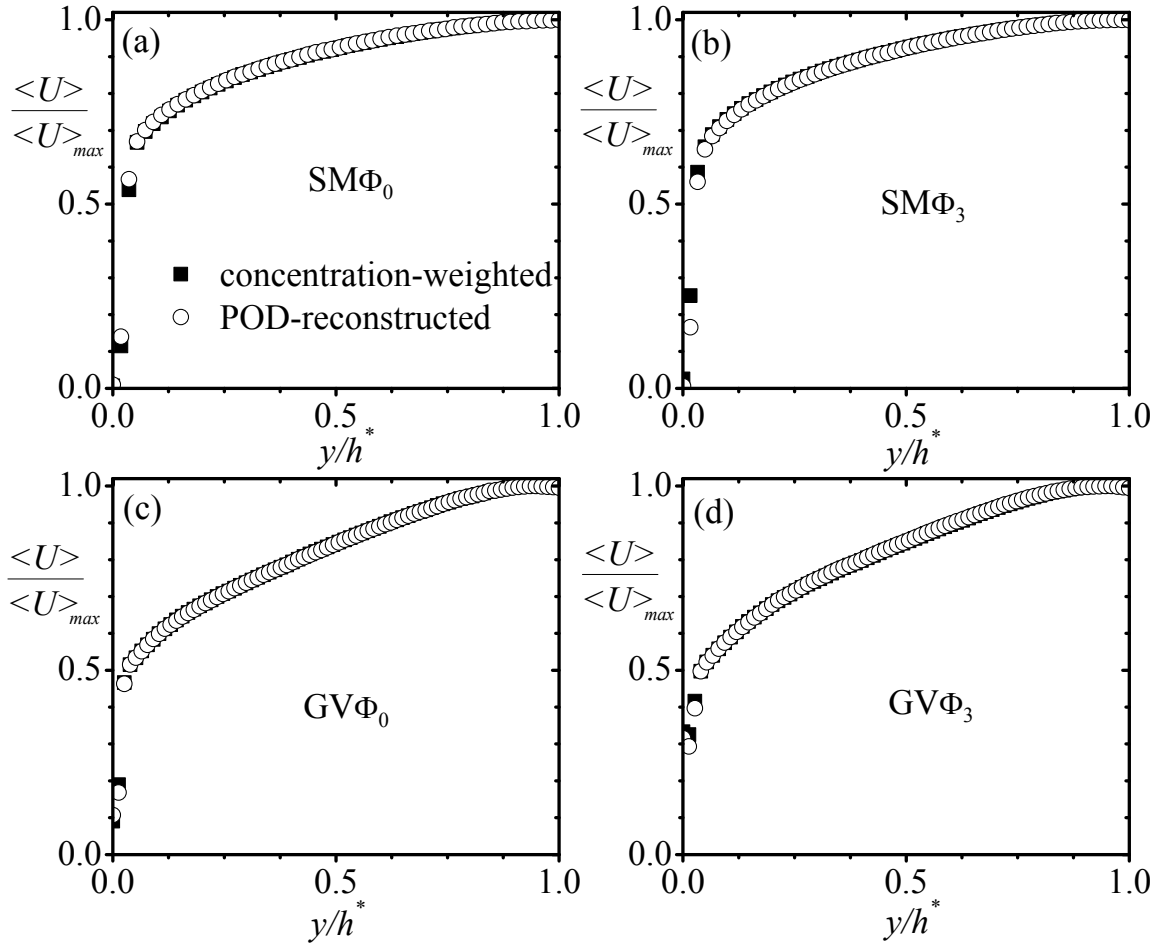

Figure 4.25: Profiles of the mean velocity reconstructed from the POD of the total velocity field.

4.6 Chapter Summary

In this Chapter, both instantaneous and statistical quantities were used to quantify the impact of particles and wall roughness on the flow characteristics and turbulence structure. Instantaneous structure visualization techniques such as variable interval time averaging (VITA) and wavelet decomposition were used to identify the instantaneous structures in the flow. Statistical results such as the mean velocity, turbulence intensities,

Reynolds shear stress and two-point correlations were calculated using volume fraction weighted averaging.

The VITA technique was used to highpass filter the flow, which was further decomposed by means of orthogonal wavelets in order to reveal the instantaneous structures. It was found that both sweeps (Q4) and ejection-like (Q2) motions were the most frequent structures over the unladen smooth wall. In the presence of particles, the flow was found to be predominated by ejections towards the outer layer. The same observation was made over the rough wall, but the ejections were more intense in the rough wall cases.

Time history records of the instantaneous particle count calculated for the smooth and rough walls showed an exponential decay in particle concentration that occurred more rapidly as the particle loading ratio was increased. For both the smooth and rough walls, the dimensionless mean concentration showed stratification across the flow with larger values near the wall than in the rest of the flow region. The profiles also demonstrated that for both surface conditions the peak concentration is increasing with increasing particle loading ratio. Differences between the smooth and rough wall profiles include a larger mean concentration of particles close to the rough wall but a smaller concentration in the core region compared to the smooth wall.

The volume fraction weighted averaging procedure produced particle concentration-velocity correlation terms whose values were found to be negligibly small, allowing the statistics from the unladen flows and particle-laden flows to be directly compared. Because of the low particle Stokes number, the solid mean velocity, turbulence intensities and Reynolds shear stress measured for the smooth wall were found

to be in good agreement with those measured for the unladen flow. On the contrary, the presence of roughness led to significant differences between the solid phase and unladen fluid distributions in the wall region as observed in previous studies.

Particle effects on the fluid mean velocity and streamwise turbulence intensity were negligible over both the smooth and rough walls, but the gravitational settling of particles and the concentration stratification suppressed the wall-normal turbulence intensity values over the smooth wall. This effect was absent over the rough wall. The Reynolds shear stress was also found to be independent of particle loading for the smooth wall, but the peak values were enhanced in the presence of the rough wall.

The distributions of the Reynolds shear stress correlation coefficient show enhancements in the presence of both particles and wall roughness, providing a sneak peek of the tendency of the particles and wall roughness to enhance the two-point correlations.

A quadrant decomposition of the fluid Reynolds shear stress revealed that both ejections and sweeps were the more important motions contributing to the fluid Reynolds shear stress, with relative magnitudes that were more significantly enhanced over the rough wall compared to the smooth wall.

Distributions of the mean and root-mean-square swirling strength showed turbulence augmentation in the inner parts of the rough wall boundary layer, but this effect was nullified in the presence of particles. In the outer layer, the swirling strength distributions did not exhibit any dependency on particle loading and the wall roughness condition. Decomposition of the swirling strength into its constituent parts (prograde and retrograde swirling strength) revealed that prograde swirling strength occurred more

predominantly near the channel wall, while retrograde swirling strength were found more predominantly in the core region.

To quantify the influence of particles and wall roughness on the average size and inclination of the turbulence structures, the two-point auto-correlations of the velocity fluctuations, R_{uu} and R_{vv}, were calculated at various wall-normal locations. Particles and roughness were found to substantially increase the streamwise and wall-normal extents of the two-point correlation contours compared to the unladen smooth wall. The effects were found to be more dramatic in the wall-normal auto-correlation function than the streamwise auto-correlation function. Accompanying these enhancements in structure extents was a more gradual decay of the structure inclination angle in the presence of the particles.

Further analysis based on two-point correlations between the fluid velocity fluctuations and swirling strength, $R_{\lambda u}$ and $R_{\lambda v}$, showed that there is a strong correlation between the spatial scales and prograde vortices in the flow.

A conditional average of the flow fields obtained by linear stochastic estimation given the occurrence of a prograde vortex, indicated that the average structure is an inclined shear layer for both the smooth and rough walls. The shear layers were found to possess similar inclination angles as the two-point correlations, demonstrating their connectivity with the two-point correlations.

Finally, the snapshot POD method was used to analyze the smooth and rough wall flows. The spectral results showed that the decomposition converged more rapidly for the particle-laden and rough wall flows than the unladen smooth wall flow. Application of the POD to the instantaneous velocity fields provided an alternative approach that

allowed the mean flow to be reconstructed from the first few modes of the decomposition.

CHAPTER 5

CONCLUSIONS AND RECOMMENDATIONS

5.1 Summary and Conclusions

The main goal of this investigation was to characterize experimentally the impact of small solid particles on the flow characteristics and structure of low Reynolds number turbulent channel flows over smooth and rough surfaces. In nearly all previous investigations of near-wall particle-laden turbulent flows, only smooth surfaces were considered and particles were added to the flow at a relatively constant loading ratio. In the present work, the particle loading ratio was varied by allowing particles to settle out of the flow without replenishment. A particle image velocimetry (PIV) technique was used to perform measurements of the velocities of the carrier fluid (water) and the solid particles in the streamwise – wall-normal plane of a horizontal rectangular channel. The particle-laden experiments were performed for three bulk volumetric loadings of approximately 2.0×10^{-4}, 4.0×10^{-4} and 8.0×10^{-4}, all three of which were chosen to allow a sufficient seeding density for the PIV. Particles response to turbulence and their influence on the carrier flow were investigated statistically using a volume fraction-weighted averaging method that incorporated the particle concentration decline in the calculation of the statistical quantities.

The results indicate that the solid phase is more responsive to changes in the loading ratio over the rough wall than the smooth wall. For the smooth wall, the particles mean velocity, turbulence intensities and Reynolds shear stress closely matched those of the unladen flow and the results were found to be nearly independent of particle loading

ratio. This agreement is considered as an artifact of the relatively small values of the Stokes number. Over the rough wall, substantial differences were observed between the particles and fluid velocity statistics, which include a more dramatic reduction in the streamwise mean velocity and augmentation of the turbulence intensities and Reynolds shear stress with increasing loading ratio. Even though the Stokes number is comparatively lower over the rough wall, the higher concentration of particles near the rough wall caused an increase in the frequency of particle-wall collisions that, as shown in previous studies, do not only influence the solid mean velocity profile, but also significantly increase the velocity fluctuations. The strongest enhancement was noticed in the solid Reynolds shear stress distributions. The effect on the Reynolds shear stress can be attributed to a superposition of the respective increases in the streamwise and wall-normal particle velocity fluctuations and an enhanced correlation between them.

The fluid mean velocity, streamwise turbulent intensity and Reynolds shear stress were unaffected by particles over the smooth wall. Stratification of the particle concentration field due to the gravitational settling of particles towards the bottom wall produced a damping effect on the wall-normal motions. This resulted in a concomitant attenuation of the wall-normal turbulence intensity over the smooth wall. Although the presence of roughness led to a reduction in the fluid mean velocity, and dramatically enhanced the turbulence intensities and Reynolds shear stress, only the Reynolds shear stress showed a sensitivity to changes in loading ratio. This was confirmed by a quadrant decomposition of the laden fluid Reynolds shear stress that revealed substantial enhancements in the ejections (Q2 motions) and sweeps (Q4 motions) over the rough wall as the loading ratio increased. Statistical distributions of the swirling strength

revealed that the intensity of swirl within the vortex cores was increased by the roughness perturbation but dampened by particles close to the wall. The vortex cores were identified to be predominantly prograde vortices, which may be heads of hairpin vortices advecting through the measurement plane.

Two-point correlations between the velocity fluctuations and between the velocity fluctuations and swirling strength were larger and more elongated in the presence of particles and the wall roughness when compared to the unladen smooth wall flow. The enlarged structures may be attached eddies extending much further into the outer flow due to the particles and wall roughness. This would imply that in these cases, the particles and the wall roughness acted to improve the communication between the outer and inner layers. Thus, wall-layer models that assume that the outer flow is detached from the near wall flow must consider these structural changes in the presence of roughness and particles to accurately capture the flow physics. Enlargement of the near-wall structures in the presence of small particles and wall roughness may be explained when one considers the larger-scale eddies as the signature patterns of coherently aligned vortex cores in the flow. The effect of settling particles and wall roughness, both of which were visualized to induce significant backflow in the fluid, would be to increase the spatial extents of the structures by increasing the vortex spacing.

A linear stochastic estimation of the conditional average of the velocity fields revealed that the larger scale eddies are shear layers inclined at approximately 10º to the wall. A proper orthogonal decomposition of the smooth and rough wall velocities demonstrated that these structures capture more of the fluid turbulent kinetic energy in the presence of particles and wall roughness in comparison to unladen smooth wall flow.

5.2 Recommendations

The present study has provided the first baseline measurements of the flow statistics in particle-laden smooth and rough wall turbulent flows subjected to a varying concentration. The results should prove useful in the development and calibration of two-fluid turbulence models. One recommendation for future research would be to modify the experimental apparatus to allow continuous injection and reloading of the particulate phase in order to maintain a constant particle concentration in the flow. This would expand the utility of the database to include the more common steady state statistical results for direct comparison with previous DNS and experiments.

The strongest impact of particles and wall roughness was noticed in the turbulence structure. Although the planar PIV used in the study was able to provide both the instantaneous and statistical information necessary to infer turbulence structures, a three-dimensional PIV that captures all three velocity components could provide a more complete description of the impact of the imposed perturbations on the turbulence structure. The observation, for instance, that the predominantly occurring prograde vortex cores were heads of hairpin vortices would require both instantaneous visualizations and statistical correlations in the spanwise (x-z) plane for verification. The 3D measurements would also help in the assessment of all terms in the dissipation and the extra dissipation terms of the TKE transport equation. Knowledge of these dissipation terms as well as the other budget terms in the tke transport equation can be used to provide more insight into effects of particles on the turbulence structure.

Finally, a particle tracking velocimetry (PTV) method may be used for the determination and tracking of the velocities of individual particles instead of the PIV

method of calculating the cross-correlation among a cloud of particles. When large particles are involved, individual particle tracking may be the only viable alternative, since in these cases, the seeding density may be so small as to lead to errors in the PIV correlation.

APPENDIX A

FLOW QUALIFICATION

Preliminary single-phase experiments were conducted over the smooth wall and gravel roughness at a maximum streamwise mean velocity of $\overline{U}_{max} \approx 0.5$ m/s. Statistics were calculated at various streamwise and spanwise locations, and the results were used to investigate the streamwise development and two-dimensionality of the flow. In general, a turbulent channel flow is described as fully developed when it exhibits constant statistical moments in the streamwise direction. Research has shown that this effect occurs much earlier over a rough surface than a smooth surface and more quickly at higher Reynolds numbers over a given surface. When the spanwise variations in the flow statistics are minimal, the flow can be considered two-dimensional.

A.1 Flow Development

Although issues of flow development has been studied widely in the past, there is still no general consensus on the exact value of the minimum distance required for the flow to be considered as fully developed. Various values have been suggested over the years for turbulent channel flows and ZPG turbulent boundary layers. Comte-Bello (1965) and Johansson & Alfredsson (1982), for instance, suggested the value of $x/h \approx 120$ for smooth channel flow, while Abell (1974) suggested $x/D \approx 80$ for smooth pipes, where D is the pipe diameter. Herring and Norbury (1967) reported $x/\delta \approx 20$, for smooth boundary layers, where δ is the boundary layer thickness. For rough wall turbulent boundary layers, Antonia and Luxton (1971) suggested a minimum streamwise roughness fetch of $x/\delta \approx$ 15 - 20 for the flow to attain self-similarity.

In the present work, the smooth wall flow at $\overline{U}_{max} \approx 0.5$ m/s, which is the case expected to be most affected by flow under-development was used as the test case to check for the flow development. The measurements were conducted at the streamwise distances of $x/h \approx 44$, 61, and 76 from the inlet of the channel. Statistical distributions of the streamwise mean velocity and turbulence characteristics were measured and compared. At the mid-span, the variations in the absolute values of the maximum streamwise mean velocity, streamwise and wall-normal turbulence intensities and the Reynolds shear stress are respectively within 1.7%, 2.9%, 3.2% and 3.5%. The variations in the Reynolds shear stress correlation coefficient, $\rho_{-uv} = -\overline{u'v'}/\left(\overline{u'^2}\,\overline{v'^2}\right)^{0.5}$ and Townsend structure parameter $a_1 = -\overline{u'v'}/\left(2q^2\right)$ were found to be within 3%. Figure A.1 shows the profiles of the mean velocity and the turbulence statistics considered. The mean velocity, and turbulence intensities are normalized by $\overline{U}_{max}$, while the Reynolds shear stress values are normalized by $\overline{U}_{max}^2$. The profiles show very good agreement among the three streamwise locations, which is the first indication of self-similarity in the dimensionless statistics. The correlation coefficient peaks at values of approximately 0.42 ± 0.1, which compare well with values of 0.45 ± 0.05 reported in previous studies (e.g., Klebanoff 1954; Lu and Willmarth 1973). For y/h^* within $0.1 \leq y/h^* \leq 0.5$, the structure parameter is approximately 0.12 ± 0.01, which also agrees well with Townsend's (1976) value of $a_1 \approx 0.13$.

Distributions of the skewness and flatness factors of the fluctuating velocities are also sometimes used to check flow development. The skewness and flatness factors, $S_\alpha = \overline{\alpha^3}/\left(\overline{\alpha^2}\right)^{3/2}$ and $F_\alpha = \overline{\alpha^4}/\left(\overline{\alpha^2}\right)^2$, respectively, where α represents u or v are shown in

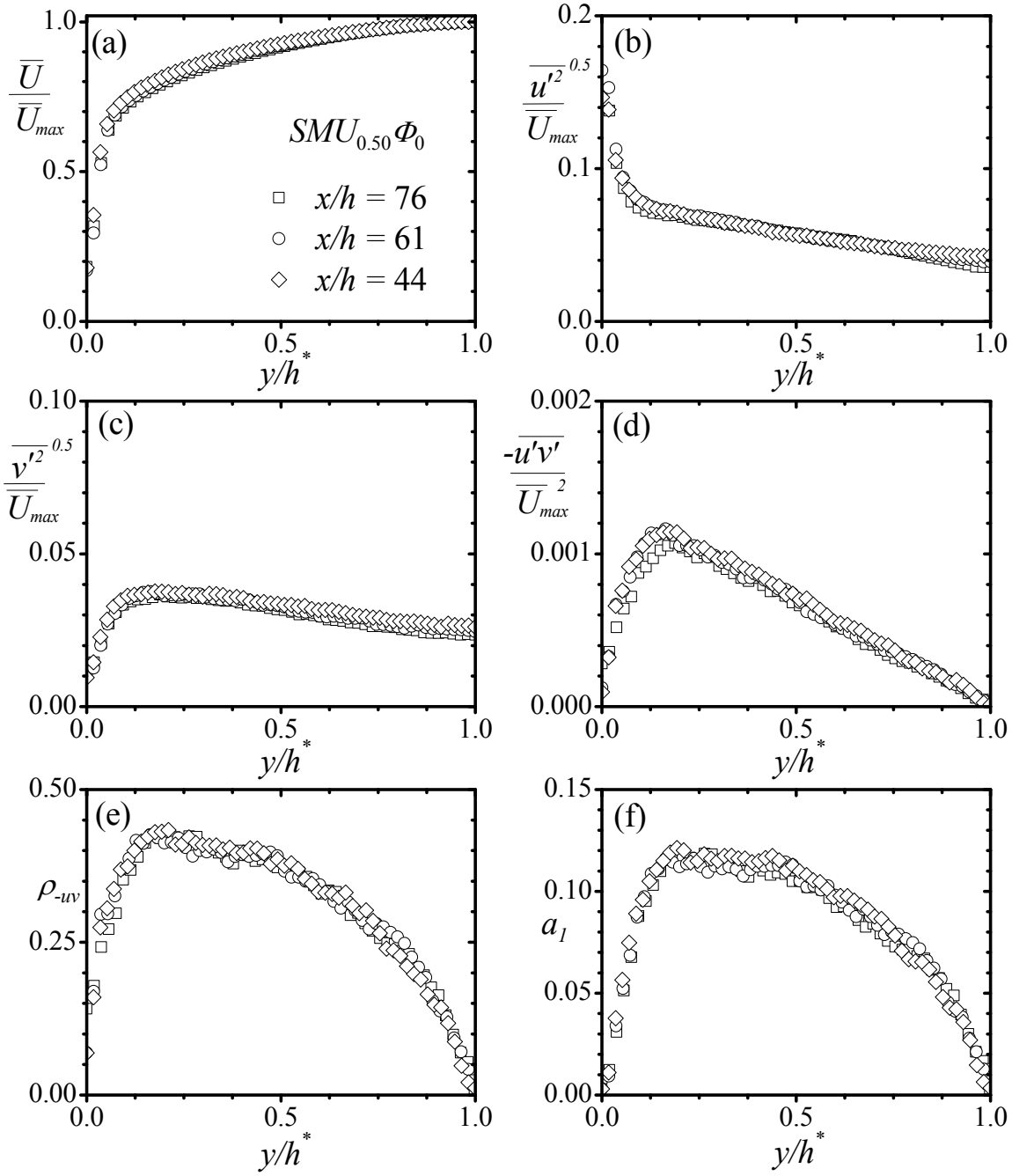

Figure A.1: Distributions of the streamwise mean velocity and selected turbulence statistics at different streamwise locations. (a) mean velocity, (b) streamwise turbulence intensity, (c) wall-normal turbulence intensity, (d) Reynolds shear stress, (e) Reynolds shear stress correlation coefficient, and (f) Townsend structure parameter.

figure A.2 for the smooth surface. It has been found in previous studies (e.g., Compte-Bello 1965; Johansson & Alfredsson 1982) that when a channel flow is not fully

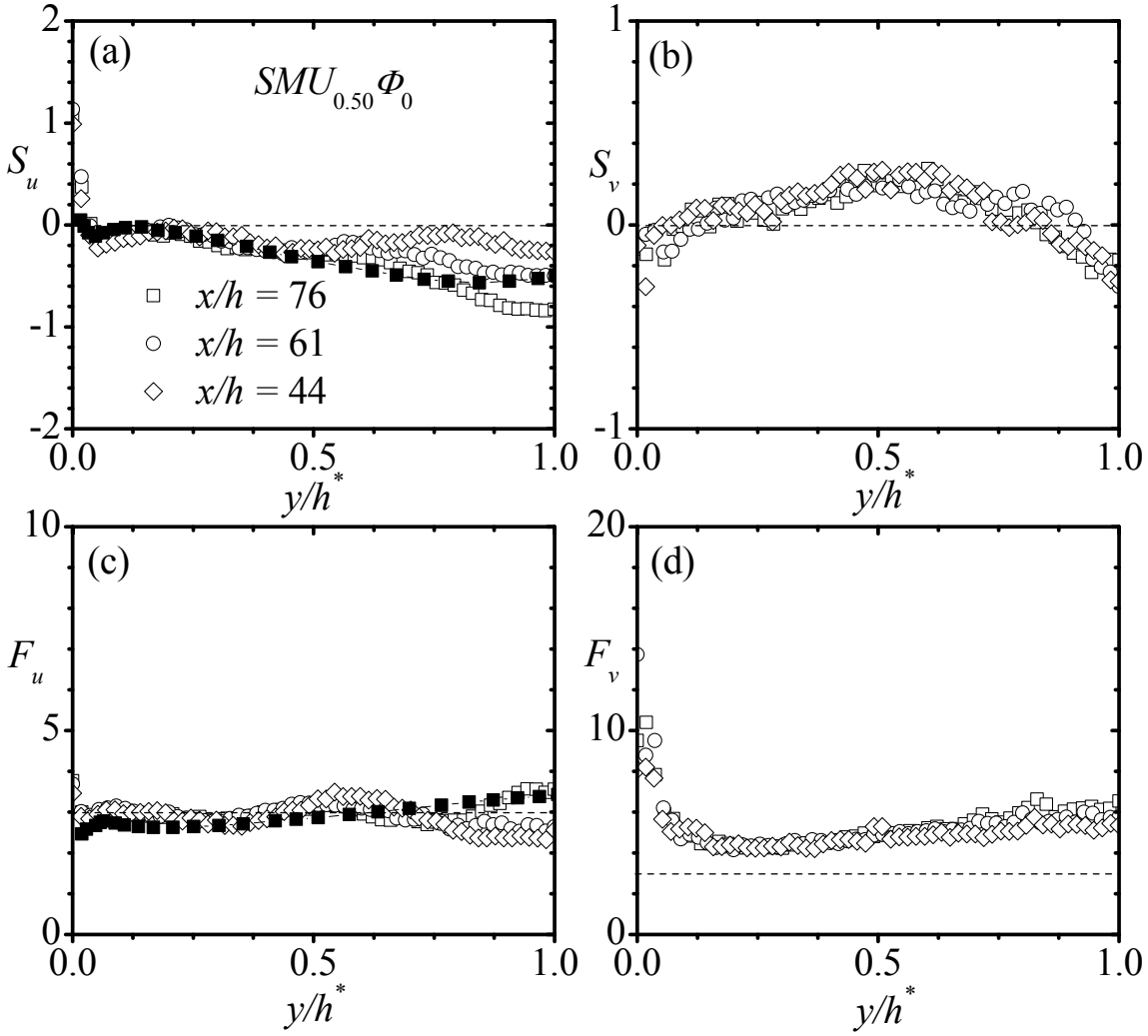

Figure A.2: Skewness and flatness factor distributions for the smooth surface. Solid square in (a) and (c) correspond to profiles obtained from Johansson and Alfredsson (1982).

developed, the centreline flow will be characterized by a large negative value of the streamwise fluctuating velocity skewness factor and a large positive value of the corresponding flatness factor. The Gaussian values are $S = 0$ and $F = 3$ and are valid for homogeneous isotropic turbulence. While the present measured S_u and F_u values (Figures A.2a and A.2c) are quite similar over most of the flow region, variations are noticed in the core region as the downstream distance increases. The profiles for the most

downstream location compare well with those of Johansson and Alfredsson (1982) except near the core of the channel. However, the present centreline values of $S_u \approx -0.8$ and $F_u \approx 3.54$ are not significantly different from centreline values of $S_u \approx -0.6 \pm 3$ % and $F_u \approx 3.51 \pm 0.8$ % previously documented. The values of the skewness and flatness factors of the wall-normal fluctuating velocity (figures A.2b and A.2d) are independent of streamwise location.

A.2 Flow Two-Dimensionality

Due to the smaller value of the channel aspect ratio ($AR \approx 5$) compared to the usually recommended value of $AR = 7$ (Dean 1978) for a two-dimensional channel flow, it is necessary to investigate the presence of possible flow three-dimensionality in the test sections. Mean flow three-dimensionality can arise from one or a combination of three factors including the presence of a strong spanwise mean shear, spanwise mean pressure gradient, or when the mean flow is subjected to a more rapid change than the turbulence statistics could adjust to (as in non-stationary or transient flows). Three-dimensional flow in a rectangular duct is characterized by the presence of secondary motions in a plane perpendicular to the streamwise direction. These secondary motions whose characteristic magnitudes may be no larger than 2 % - 3 % of the maximum streamwise mean velocity for both smooth and rough-wall flows can introduce modifications in the mean and turbulence statistics. These modifications have been found to include a bulging of the streamwise mean velocity contours towards the corners of the channel (Brundrett and Baines 1964; Gessner 1973; Fujita et al. 1989), a decrease in the magnitude of the Reynolds shear stress and misalignment between the Reynolds shear stress and the

velocity gradient angles (Bradshaw and Pontikos 1985; Moin et al. 1990), and a distortion in the symmetry and alignment of the vortical structures (Coleman et al. 1996; Le et al. 1999). The reduction in the magnitude of the Reynolds shear stress has been found to result in a decrease in the Townsend structure parameter to values even as low as a_1 = 0.05 (e.g., Anderson and Eaton 1989). On the other hand, three-dimensional channel experiments have been reported in the literature that show either higher values of the Reynolds shear stress compared to a two-dimensional channel flow (e.g., Kiesow and Plesniak 2003) or similar values (e.g., van Hout 2011).

To examine the two-dimensionality of the smooth and rough wall flows, profiles were measured at the three cross-span locations $z/b \approx 0.0$, 0.13 and 0.25 for the smooth wall and gravel roughness at $\overline{U}_{\max} \approx 0.5$ m/s. The mean velocity and turbulence statistics over the smooth wall are presented in figure A.3. These results demonstrate that the wall-normal variation of the smooth wall mean and turbulent statistics is independent of spanwise location. Corresponding skewness and flatness factor distributions S_u, S_v and F_u, F_v are depicted in figure A.4. Apart from F_u which shows slight discrepancies near the centre of the channel (albeit within measurement uncertainty), the skewness and flatness factors show no three-dimensionality effects. Figure A.5 shows the plots of $\overline{U}/\overline{U}_{\max}$, $\left(\overline{u'^2}\right)^{0.5}/\overline{U}_{\max}$, $\left(\overline{v'^2}\right)^{0.5}/\overline{U}_{\max}$, $-\overline{u'v'}/\overline{U}_{\max}^{\,2}$, ρ_{-uv} and a_1 at the three cross-pan locations over the gravel roughness. The mean velocity and the streamwise turbulence intensity show no systematic deviations with changes in the spanwise location. For the wall-normal turbulence intensity, there is agreement among the values in the near-wall region. In the outer layer, variations are found to within 14 %. The Reynolds shear stress, $-\overline{u'v'}/\overline{U}_{\max}^{\,2}$, distributions show that the signal takes on larger peak values as the sidewall is

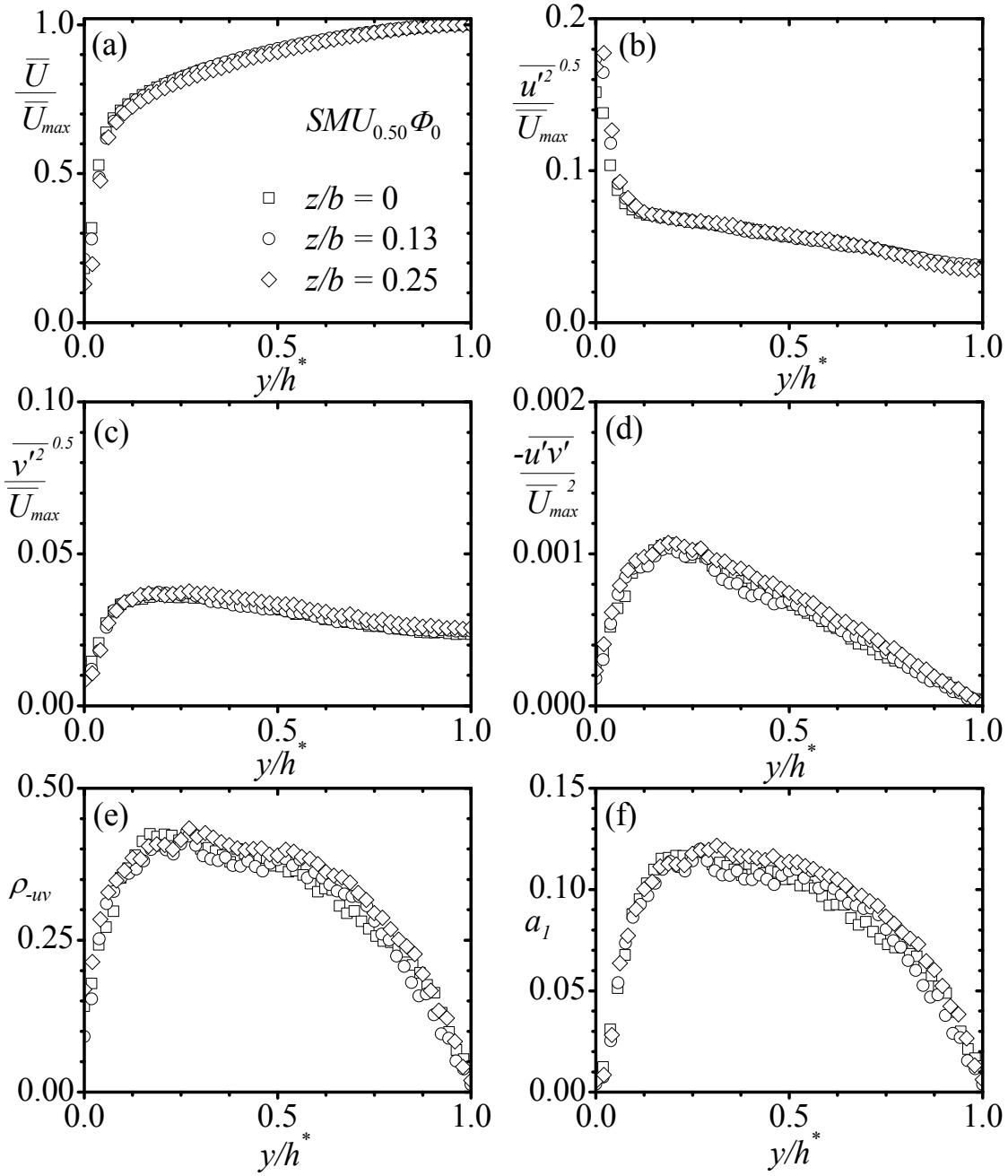

Figure A.3: Comparison of profiles at different spanwise locations to check flow two-dimensionality over the smooth surface.

approached and there are deviations of up to about 33% for $0.35 < y/h^* < 0.8$. These discrepancies may be considered an artifact of the flow inhomogeneity introduced by the roughness elements. In spite of the differences observed in the rough-wall turbulence

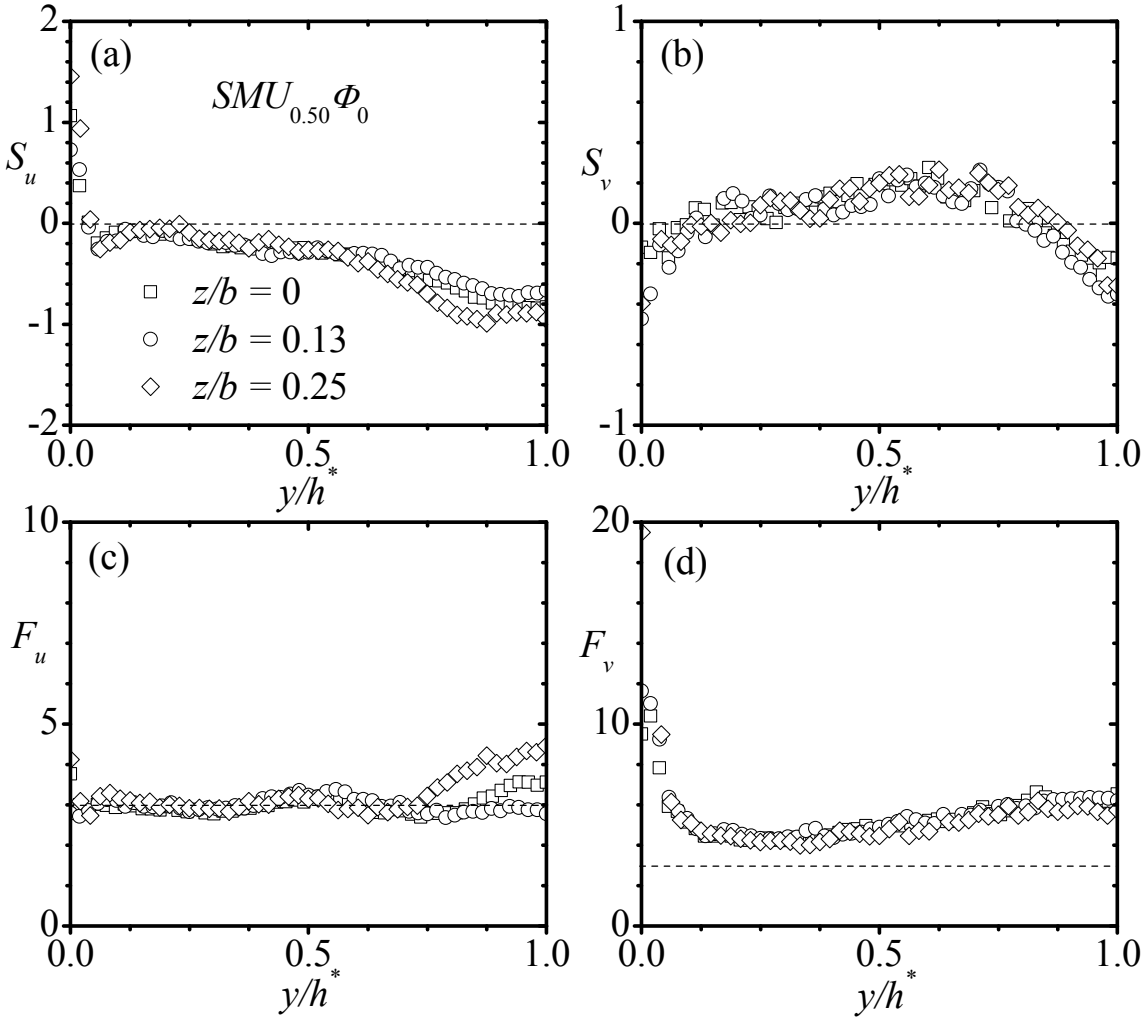

Figure A.4: Comparison of skewness and flatness factor profiles at different spanwise locations to check flow two-dimensionality over the smooth surface.

intensities and Reynolds shear stress, the correlation coefficient and structure parameter (figures A.5e and A.5f) show no significant variation with spanwise location, and the rough wall structure parameter recovers to the value of $a_1 \approx 0.13$ for y/h^* within $0.35 < y/h^* < 0.8$.

The above spanwise measurements, together with the relatively constant values of the statistical moments in the streamwise direction suggest that the baseline single-phase flow in this study is acceptably two-dimensional and fully developed.

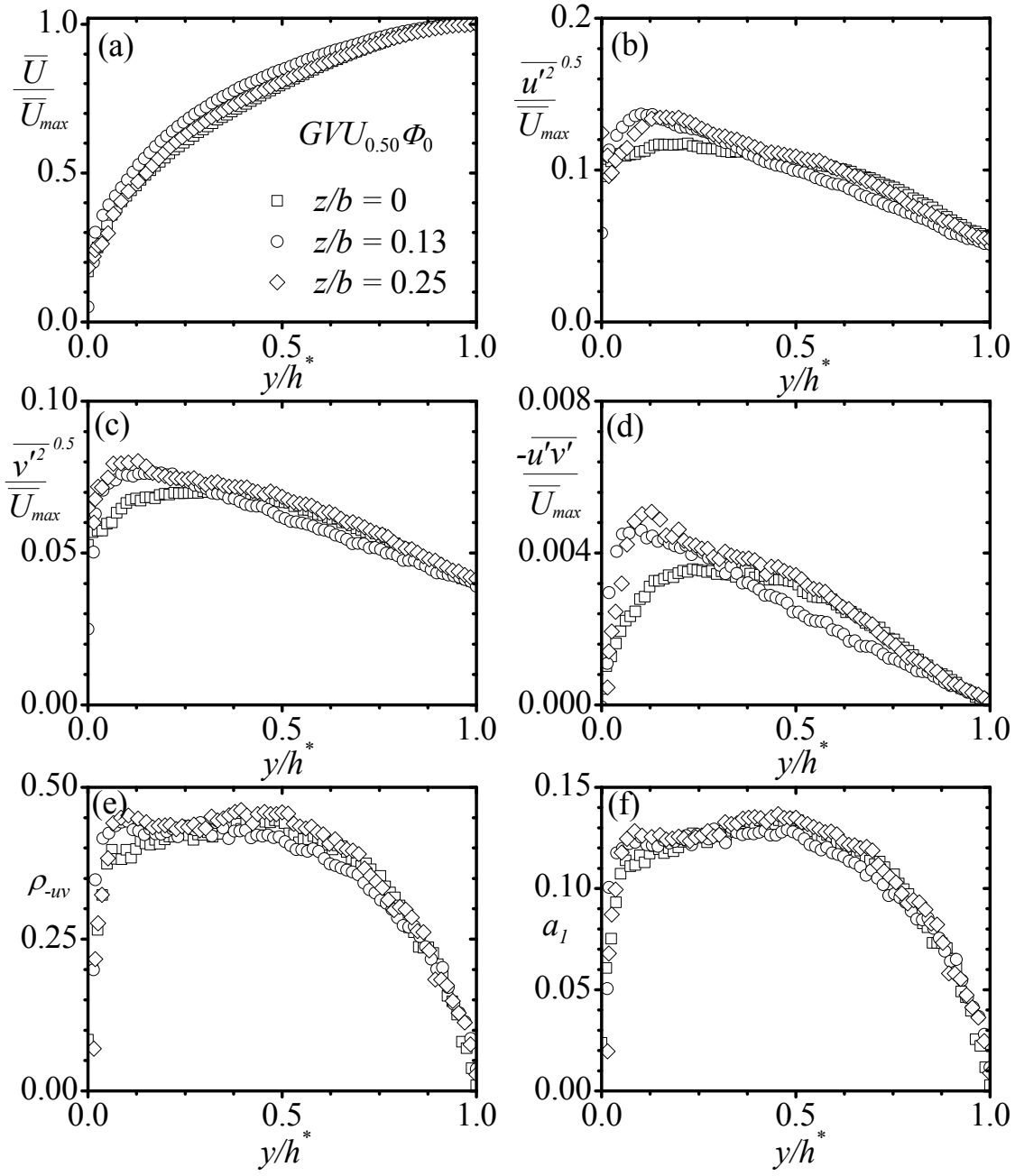

Figure A.5: Comparison of profiles at different spanwise locations to check flow two-dimensionality over the gravel surface.

APPENDIX B

RESULTS OF THE GLASS BEAD EXPERIMENTS

Because of the non-simultaneous measurement of the glass particles and carrier fluid velocities, due to the single camera arrangement, the concentration weighted averaging scheme is not applicable. In order to calculate the particulate phase and carrier fluid mean flow and turbulence characteristics, the Reynolds averaging method was used. The effects of roughness and particles on the flow are evaluated by examining profiles of the mean velocity, turbulence intensities and Reynolds shear stress. Quadrant decomposition is used to deepen insight into the response of the turbulence structure to the presence of roughness and particles. It should be recalled that the matched friction Reynolds number of $Re_\tau \approx 700$ for the smooth wall and sand grain roughness required a maximum streamwise mean velocity of $\overline{U}_{\max} \approx 0.75$ m/s over the smooth wall. Thus, in order to avoid confusion with the PMMA smooth wall conditions (at $U_{max} \approx 1.00$ m/s), all smooth wall conditions in the glass beads measurements are designated as $SMU_{0.75}\Phi_i$.

B.1 Particle Concentration Profiles

Figure B.1 shows the variation of the total particle count with time over the smooth wall and sand grain roughness. The plots follow an exponential decay profile in which it is noted that the rate of decay occurs more rapidly with increasing particle loading ratio, but less rapidly as the surface condition changes from smooth to rough. Least square exponential decay laws were fitted to the particle count values over the smooth and rough walls as shown in figures B.1e and B.1f, respectively, to quantify the rates of decay. For the lower loading ratio, $\Phi_1 = 2.0 \times 10^{-4}$, the decay law $y = y_1 + y_2 e^{at}$ was found to

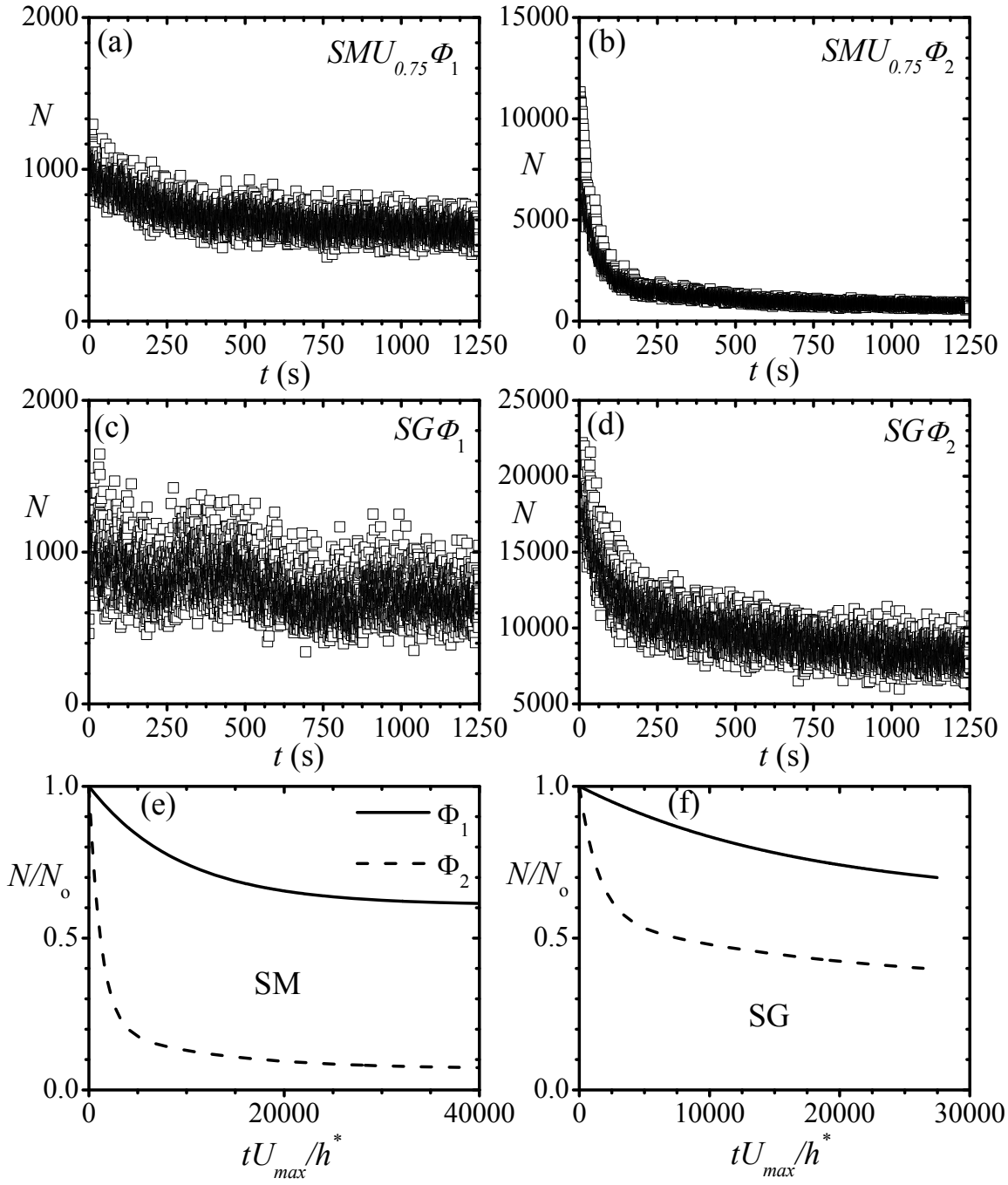

Figure B.1: Distributions of the total particle count over the smooth wall and sand grain roughness.

represent the curves very well. However, unlike the PMMA, it was found that the above expression does not fit the curves very well for the higher loading ratio, $\Phi_2 = 7.0 \times 10^{-4}$.

Table B.1: Values of least square curve fitting parameters for the exponential decay law $y = y_1 + y_2 e^{at}$.

Parameter	$SMU_{0.75}\Phi_1$	$SG\Phi_1$
a	-3.9×10^{-3}	-1.3×10^{-3}
y_1	609.988	1192.462
y_2	392.655	722.170
R^2-value	0.6609	0.2253

Table B.2: Values of least square curve fitting parameters for the exponential decay law $y = y_o + b_1 e^{[-(t-t_0)/a_1]} + b_2 e^{[-(t-t_0)/a_2]}$.

Parameter	$SMU_{0.75}\Phi_2$	$SG\Phi_2$
a_1	352.607	907.079
a_2	37.801	66.816
b_1	1516.354	9198.552
b_2	7276.481	11787.945
t_o	4.958	27.111
y_o	723.252	13877.377
R^2-value	0.9761	0.8348

This is because the exponential decline of the glass particles at higher loadings occurs very rapidly initially over a small time window before leveling off to a relatively steady level. The fitted curves for the higher loading ratio correspond to the exponential decay law $y = y_o + b_1 e^{[-(t-t_0)/a_1]} + b_2 e^{[-(t-t_0)/a_2]}$. The values of the curve fitting parameters over the smooth and rough walls are summarized in Tables B.1 and B.2, respectively, for Φ_1 and Φ_2

Figure B.2 shows the mean concentration profiles over the smooth wall and sand grain roughness. In both the smooth and rough wall case, the mean concentration is

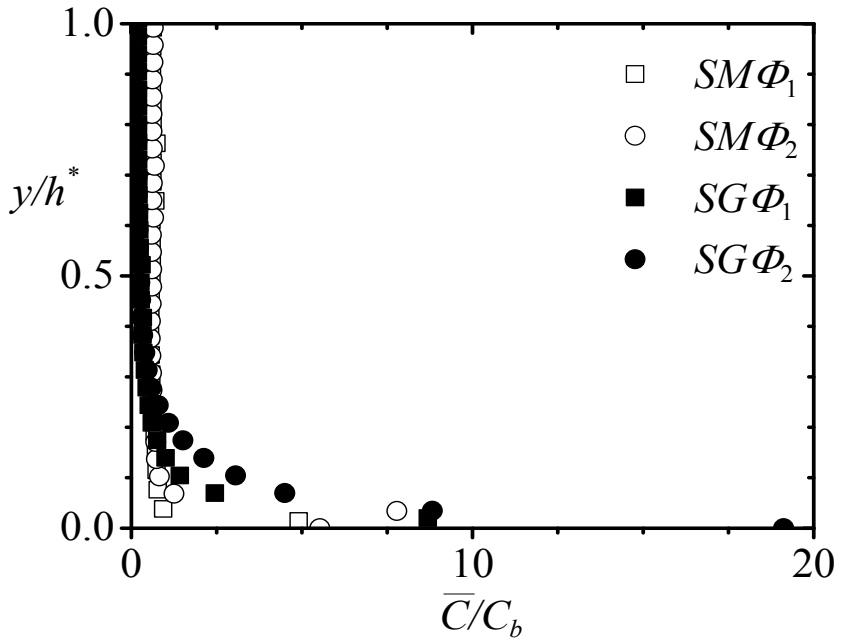

Figure B.2: Profiles of the particle mean concentration over the smooth wall and sand grain roughness.

higher in the wall region than the rest of the flow region with peak values at the wall. Over the smooth wall, the peak value of the mean concentration is increased by about 25% as the loading ratio is increased while over the rough wall it was enhanced by about 100%. For the rest of the flow region, the concentration profile remains relatively uniform and at a value approaching the bulk or depth averaged value.

B.2 Profiles of the Mean Velocity, Turbulence Intensities and Reynolds Shear Stress

Figure B.3 shows a comparison of the glass mean velocity, turbulence intensities and Reynolds shear stress profiles to corresponding profiles of the particle-free flow. The mean velocity plots (figure B.3a) show that the glass particles move faster than the fluid over a substantial portion of the flow over the smooth and rough walls. Differences are

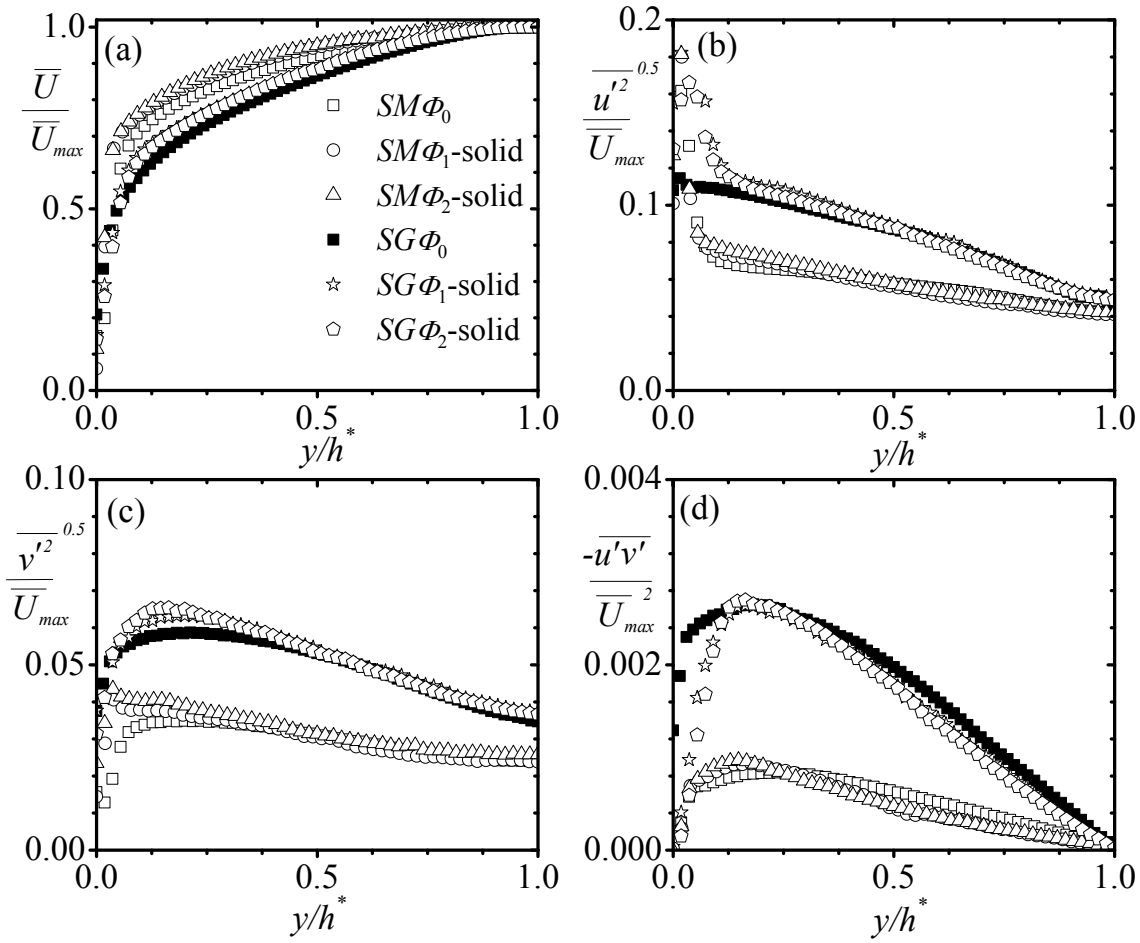

Figure B.3: Profiles of the solid mean velocity, turbulence intensities and Reynolds shear stress.

also observed among the turbulence intensity profiles in the form of relatively larger peak values in the solids case compared to the fluid for both the smooth and rough walls. In the case of the Reynolds shear stress, the profiles indicate higher peak values for the solid phase but lower values in the outer layer for the smooth wall flow. Over the rough wall, although the fluid and solid Reynolds shear stress exhibit nearly similar peak values, elsewhere within the flow region, the solid phase values are relatively lower, with the largest deviations occurring as the wall is approached. The generally lower values of the solid Reynolds shear stress irrespective of the higher turbulence intensities can be

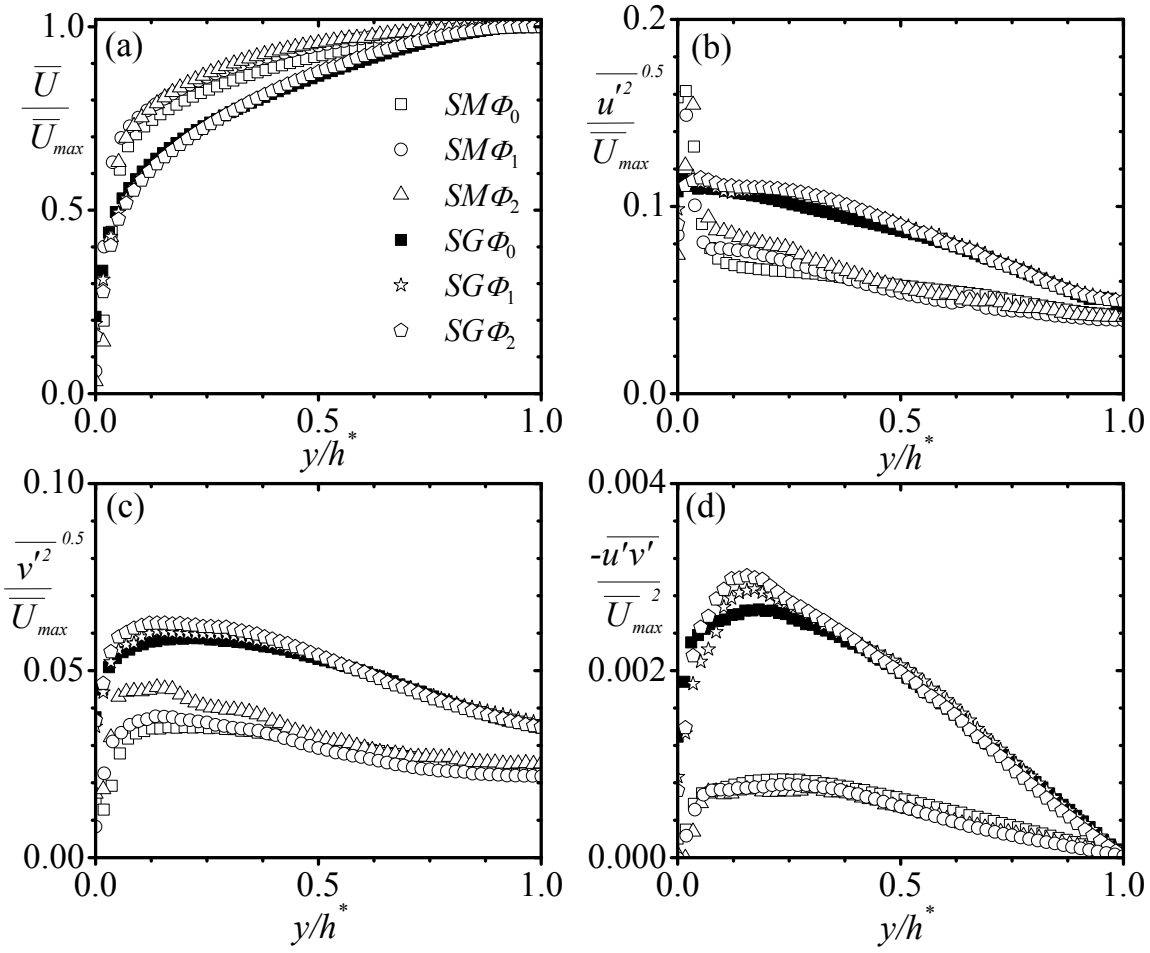

Figure B.4: Profiles of the fluid mean velocity, turbulence intensities and Reynolds shear stress.

attributed to a reduced correlation between the velocity fluctuations. This effect appears to be more pronounced over the rough wall than the smooth wall.

Figure B.4 examines the effects of the glass particles on the carrier fluid mean velocity, turbulence intensities and Reynolds shear stress over the smooth wall and sand grain roughness. Over the smooth wall, the mean velocity is slightly increased for the particle-laden smooth wall flow in comparison to the unladen smooth wall flow. This may be attributed to particles travelling faster than the fluid, thereby, dragging the flow along with them. This effect is however overcome by the presence of the rough wall,

leading to collapse of the profiles. The streamwise turbulence intensity profiles (figure B.4b) show enhancement by particles within the range $0.05 < y/h^* < 0.28$ over the smooth wall, and the effect is increasing with increasing loading ratio. Over the rough wall, enhancements of about 11% are observed within the range $0.25 < y/h^* < 0.5$, but no further increase is observed with increasing loading ratio. Comparing the smooth and rough wall distributions, it can be seen that the presence of roughness led to a suppression of the peak streamwise turbulence intensity compared to the smooth wall values. Away from the wall, the intensity levels are enhanced by the roughness perturbation. The wall-normal turbulence intensity (figure B.4c) is enhanced by particles near the smooth wall and the effect is more rapid as the loading ratio increases. This reflects results from previous experiments with glass beads (e.g., Best et al. 1997; Righetti and Romano 2004) that show significant enhancements in the wall-normal turbulence intensity by the glass particles. As with the streamwise turbulence intensity, there is a tendency for roughness to reduce the effect of particles on the wall-normal turbulence intensity. For a given loading condition, the wall-normal turbulence intensity level is significantly enhanced over the entire flow region. A more dramatic effect of the roughness is observed in the Reynolds shear stress distributions (figure B.4d), and there is an additional increase with particles as the loading ratio is increased. Over the smooth wall, particles do not produce any significant modifications in the Reynolds shear stress irrespective of the approximately four-fold increase in the loading ratio.

B.3 Quadrant Decomposition of the Fluid Reynolds Shear Stress

A quadrant decomposition based on the Lu and Willmarth (1973) hyperbolic hole method

was used to sort the fluid Reynolds shear stress into the various quadrants of the u-v plane. To examine the effects of the choice of hole size H on the measured contributions, the fractional contributions to the mean Reynolds shear stress and the fraction of the time spent in a hole, T_H, were calculated at various wall-normal locations. Figure B.5 shows profiles of the fractional contributions and the hyperbolic hole time fraction for the unladen smooth and rough wall flows. The profiles show that the fractional contributions and the hole residency time are all smooth functions of hole size. Qualitatively, the profiles exhibit the same trend of highest fractional contributions at $H = 0$ and a monotonic decrease with increasing hole size. At the same time, the fraction of the time spent in a hole increases rapidly from 0 at $H = 0$ to a maximum value at $H \approx 2$ and remains constant for $H > 2$. Close to the smooth wall (figure B.5a), the fractional contribution remains about the same for sweeps and ejections for all values of H. Away from the smooth wall (figures B.5c and B.5e), ejections become increasingly stronger than sweeps and in the outer layer the fractional contributions of ejections remain substantial over the entire range of H. Near the rough wall (figure B.5b), the fractional contribution of sweeps are comparatively larger than that of ejections, and the differences remain significant for values of H up to about 7. The larger values of sweeps compared to ejections is a commonly observed characteristic for rough wall channel and boundary layer flows, and is attributed to the shift in origin over the rough wall. Away from the rough wall (figures B.5d and B.5f), there is a wall-normal location where there is cross-over in the relative importance of sweeps and ejections so that in the outer layer sweeps are outstripped by the ejections for $H < 7$. The smooth and rough wall distributions suggest that for increasing values of H, a larger fraction of the time is spent in the hole

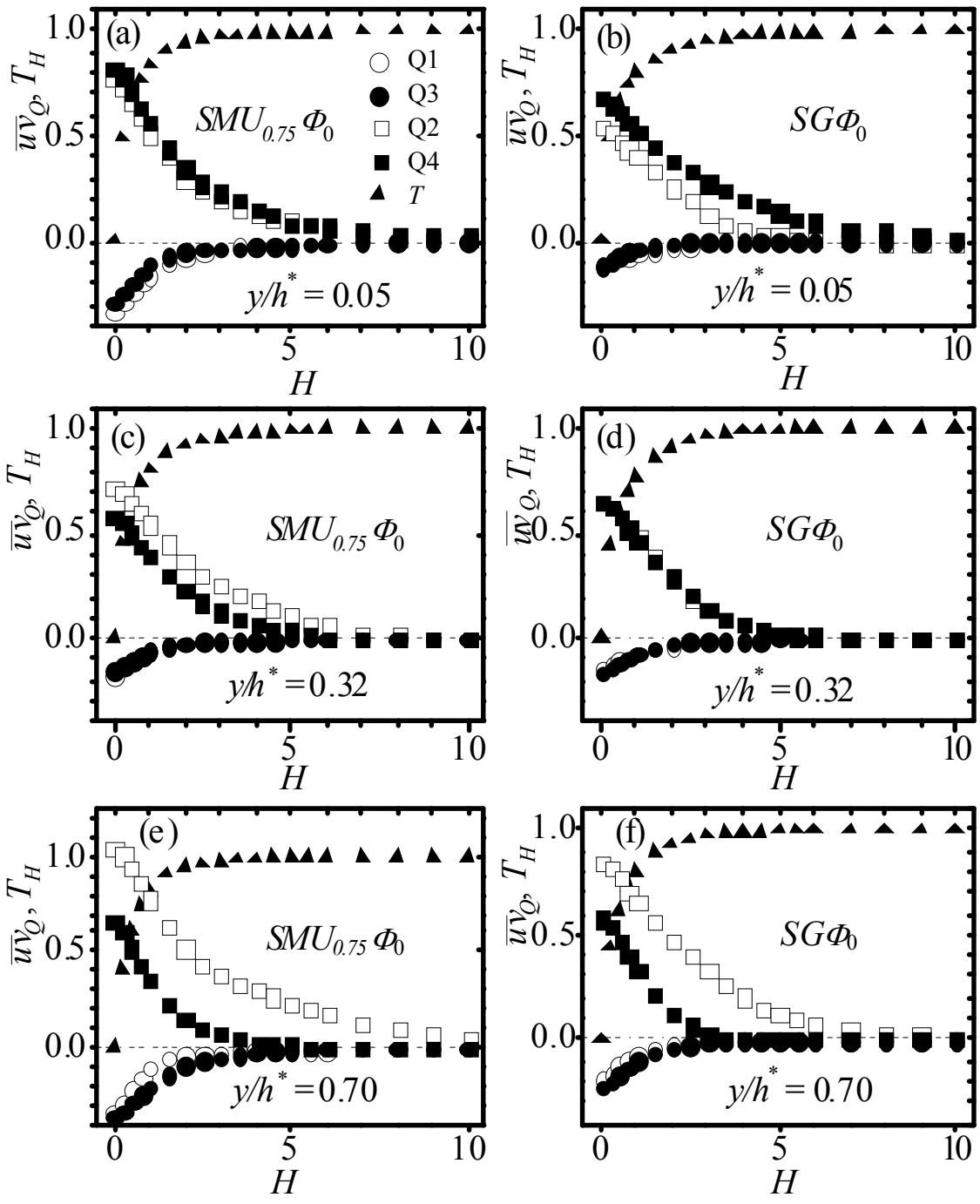

Figure B.5: Effects of choice of hyperbolic hole size on the fractional contributions.

region, and that in the outer layer ejections are the major contributors to the mean Reynolds shear stress. The plots also indicate that when differences occur between

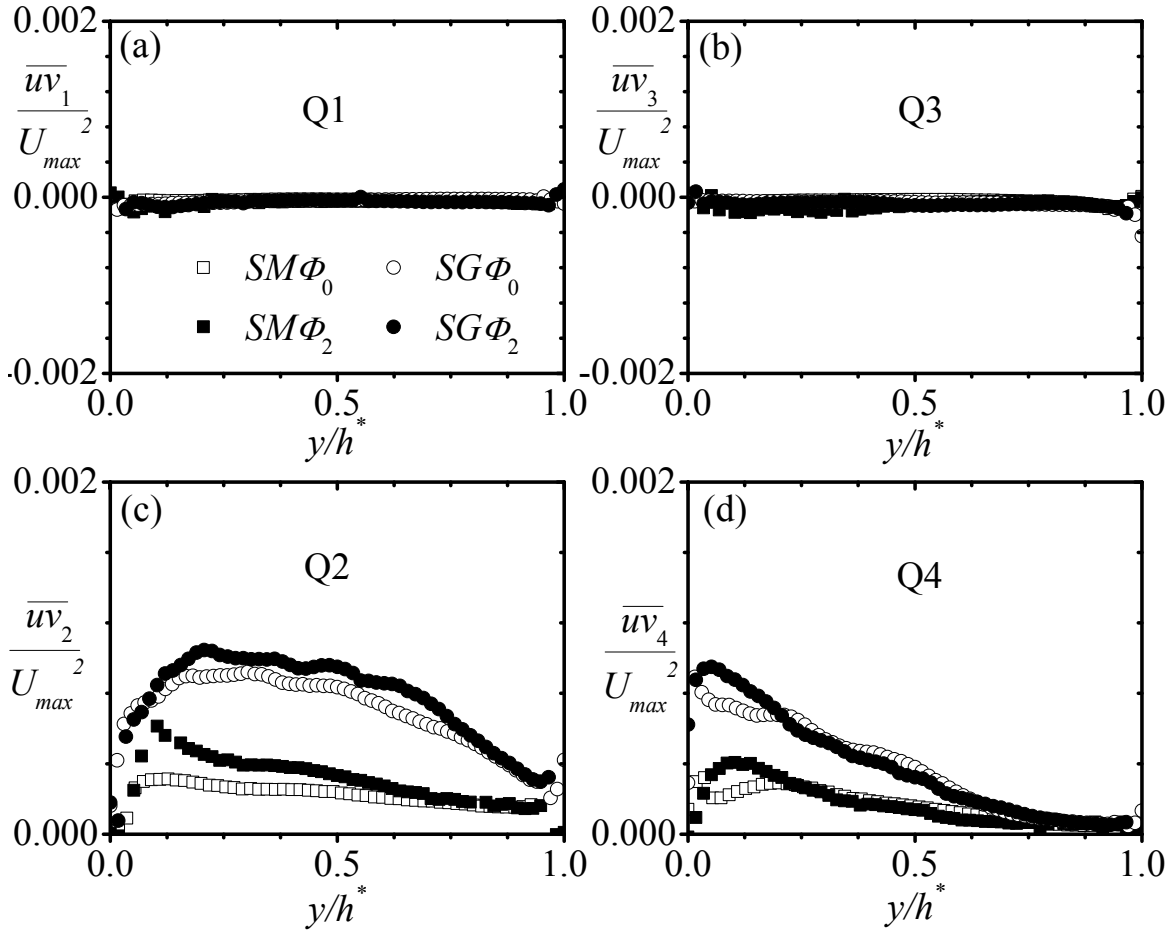

Figure B.6: Quadrant decomposition of the fluid Reynolds shear stress.

ejections and sweeps, these differences remain approximately constant for $H \leq 4.5$.

To examine the impact of particles and wall roughness on the wall-normal distributions of the quadrant contributions, a suitable hole size has to be selected. Here, in order to include only stronger events in the quadrant decomposition the hole size was set to value $H = 2$, which corresponds to instantaneous Reynolds shear stress values larger than about 5 times the mean Reynolds shear stress. The quadrant decomposition results normalized by the outer velocity scale U_{max}^2 are presented in figure B.6. The contributions from the unladen flow are in good agreement with those reported over

previous smooth and rough wall channel flows (e.g., Krogstad et al. 2005). Figures B.6a and B.6b show that the outward and inward interaction terms are relatively unimportant over the smooth and rough walls. Particles and roughness effects on the ejections (Q2) and sweeps (Q4), which are the more dominant contributors to the Reynolds shear stress are shown in figures B.6c and B.6d, respectively. The ejection and sweeps are substantially enhanced by the wall roughness compared to the smooth wall, but the effect on ejections extends much farther into the outer layer than observed for sweeps. Over the smooth and rough walls, the presence of particles led to enhancements in the Reynolds shear stress producing motions, although the effect on ejections is more pervasive than on sweeps.

APPENDIX C

EXPERIMENTAL UNCERTAINTY ANALYSIS

This appendix documents the procedure employed for estimating the uncertainties in the measured variables. The AIAA methodology derived by Coleman and Steele (1995) was used. The procedure is outlined as follows. For a given measurement system, if a measured variable, R, can be expressed as a function of independent variables, X_1, X_2, X_3, ..., X_n, the total uncertainty E_R in R can be quantified as

$$E_R^2 = B_R^2 + P_R^2 \tag{C.1}$$

where B_R and P_R are the total systematic and random errors in R caused by uncertainties in the determination of the X_i's. The combined systematic and random errors in the independent variables are found by expanding B_R and P_R in a Taylor series. Dropping higher order terms in the expansion would result in expressions of the form

$$B_R^{\,2} = \sum_{i=1}^{n} \theta_i^{\,2} B_i^{\,2} + 2\sum_{i=1}^{n-1}\sum_{k=i+1}^{n} \theta_i \theta_k B_{ik}^{\,2} \tag{C.2}$$

and

$$P_R^{\,2} = \sum_{i=1}^{n} \theta_i^{\,2} P_i^{2} + 2\sum_{i=1}^{n-1}\sum_{k=i+1}^{n} \theta_i \theta_k P_{ik}^{\,2} \tag{C.3}$$

where $\theta_i = \partial R/\partial X_i$ are called sensitivity coefficients, B_i and P_i are the systematic and random uncertainty limits in X_i, and B_{ik} and P_{ik} are the correlated systematic and random uncertainty limits in X_i and X_k. Combining equations (C.2) and (C.3) yields the equation

$$E_R^{\,2} = \sum_{i=1}^{n} \theta_i^{\,2} B_i^{\,2} + 2\sum_{i=1}^{n-1}\sum_{k=i+1}^{n} \theta_i \theta_k B_{ik}^{\,2} + \sum_{i=1}^{n} \theta_i^{\,2} P_i^{\,2} + 2\sum_{i=1}^{n-1}\sum_{k=i+1}^{n} \theta_i \theta_k P_{ik}^{\,2} \tag{C.4}$$

which is called the error propagation equation for variable R. Expressions for B_i, B_{ik}, P_i, and P_{ik} are of the form $B_i = tb_i$, $B_{ik} = t^2 b_{ik}$, $P_i = tS_i$, $P_{ik} = tS_{ik}$, where b_i, b_{ik}, S_i, and S_{ik} are

estimates of the systematic and random uncertainty limits. The factor t is derived from a Student t distribution. For a large number of observations ($M \geq 10$), $t = 2$ at the 95% confidence level.

In the present analysis, the systematic uncertainty limits were obtained from the manufacturer's specifications supplied with the PIV system. The random uncertainty limits of the measured variables were calculated using the alternate approach suggested by Stern et al. (1999). In the alternate approach, assuming correlated random uncertainties are negligible, rather than compounding the elemental random uncertainty limits as in Eq. (C.3), P_R can be obtained from repeatability tests on R. If S_R is the standard deviation of M samples of R, then P_R is given by

$$P_R = \frac{tS_R}{\sqrt{M}} \tag{C.5}$$

where $t = 2$ for a sample size $M \geq 10$ at the 95% confidence level. The standard deviation is calculated from

$$S_R = \left[\sum_{k=1}^{M} \frac{\left(R_k - \overline{R}\right)^2}{M-1} \right]^{1/2} \tag{C.6}$$

where $\overline{R}$ is the mean value of the M samples of R given by

$$\overline{R} = \frac{1}{M} \sum_{k=1}^{M} R_k \tag{C.7}$$

C.1 Uncertainty in the Mean Velocity

In the present measurements, the systematic error in the mean velocity is considered to be of the same order as the error in the instantaneous velocities. In PIV, the instantaneous

velocity at a point is the average fluid velocity over an interrogation area and is given by

$$U_i = \frac{\Delta s}{M \Delta t} \tag{C.8}$$

where i = 1 and 2, Δt is the time between laser pulses, Δs is the particle displacement from the correlation algorithm, and M is the camera magnification. Using Eq. (C.2) and assuming no correlated systematic uncertainty limits in the independent variables, the systematic uncertainty limit in U_i is given by

$$B_{U_i}{}^2 = \theta_{\Delta s}{}^2 B_{\Delta s}{}^2 + \theta_{\Delta t}{}^2 B_{\Delta t}{}^2 + \theta_M{}^2 B_M{}^2 \tag{C.9}$$

The sensitivity coefficients are given by

$$\theta_{\Delta s} = \frac{\partial U_i}{\partial \Delta s} = \frac{1}{M \Delta t},\ \theta_M = \frac{-\Delta s}{M^2 \Delta t} \text{ and } \theta_{\Delta t} = \frac{-\Delta s}{M \Delta t^2} \tag{C.10}$$

The uncertainty estimate in the mean velocities U and V is illustrated for *T*est $SM\Phi_0$ as a representative case. The procedure is summarized in Table C.1 along with the manufacturer's specifications for the systematic uncertainty limits in Δs, Δt and M. Also shown are the mean values of the streamwise and wall-normal velocities at $y/h^* = 0.05$. The calculations were based on a magnification of M = 40.9 pixels/mm (≈ 0.304), where the camera pixel pitch is d_{pitch} = 7.4μm.

Table C.1: Systematic uncertainty limits of the streamwise mean velocity close to the smooth wall ($y/h^* = 0.04$).

Variable	Magnitude	B_X	θ_X (*SI units*)	$B_X\theta_X$ (*SI units*)	$(B_X\theta_X)^2$ (*SI units*)
Δs_u (pix)	5.36E+00	1.27E-02	8.92E+03	8.38E-04	7.02E-07
M (pix/mm)	4.09E+01	2.00E-01	-1.15E+00	-1.70E-02	2.90E-04
Δt (s)	3.70E-04	1.00E-07	-9.50E+02	-9.5E-05	9.03E-09
U (m/s)	3.54E-01	-	-	-	-

$$B_{U_i}{}^2 = \sum (B_{X_i}\theta_{X_i})^2 = \text{2.91E-04}$$

B_{U_i} = 1.70E-02

% Systematic uncertainty limit = 1.70E-02/3.54E-01 = 4.8 %.

To compute the random uncertainty limit, a total of 7000 instantaneous images were captured, and divided into 10 sets of 700 images per set. The mean velocity, $U(x, y)$ was calculated for each set to yield 10 different values of U for each grid location. The values of U at $y/h^* = 0.05$ were extracted, and averaged to give a mean value of 0.354 m/s with a standard deviation of 2.24 % in accordance with equations (C.7) and (C.6). From equation (C.5), this yields a random uncertainty limit of approximately 1.4 %.

Using equation (C.1) the total experimental uncertainty in the streamwise mean velocity is

$$E_R = \sqrt{4.8^2 + 1.4^2} = 5.0\%$$

BIBLIOGRAPHY

Abell, C.J., 1974, "Scaling Laws for Pipe Flow Turbulence," Ph. D. Thesis, University of Melbourne.

Abbott, J.E. and Francis, J.R.D., 1977, "Saltation and Suspension Trajectories of Solid Grains in a Water Stream," Philosophical Transactions of the Royal Society A, **284**, pp. 225 – 254.

Adrian, R.J., 1977, "On the Role of Conditional Averages in Turbulence Theory," In: Turbulence in Liquids, Princeton Science Press.

Adrian, R.J., Christensen, K.T., and Liu, Z.-C., 2000b, "Analysis and Interpretation of Instantaneous Turbulent Velocity Fields," Experiments in Fluids, **29**, pp. 275 – 290.

Adrian, R.J., Chung, M.K., Hassan, Y., Nithianandan, C.K., and Tung, A.T.-C, 1989, "Approximation of Turbulent Conditional Averages by Stochastic Estimation," Physics of Fluids A, **1**(6), pp. 992 – 998.

Adrian, R. J., Meinhart, C. D., and Tomkins, C. D., 2000a, "Vortex Organization in the Outer Region of the Turbulent Boundary Layer," Journal of Fluid Mechanics, **422**, pp. 1– 54.

Adrian, R.J., 1991, "Particle-Imaging Techniques for Experimental Fluid Mechanics," Annual Review of Fluid Mechanics, **23**, pp. 261 – 304.

Ahmed, A.M. and Elghobashi, S., 2000, "On the Mechanisms of Modifying the Structure of Turbulent Homogeneous Shear Flows by Dispersed Particles," Physics of Fluids, **12**, pp. 2906 – 2930.

Alfonsi, G., 2006, "Coherent Structures of Turbulence: Methods of Eduction and Results," Applied Mechanics Reviews, **59**, pp. 307 – 323.

Alletto, M. and Breuer, M., 2013, "Prediction of Turbulent Particle-Laden Flow in Horizontal Smooth and Rough Pipes Inducing Secondary Flow," International Journal of Multiphase Flow, **55**, pp. 80 – 98.

Anderson, S. and Eaton, J., 1989, "Reynolds Stress Development in Pressure-Driven, Three-Dimensional, Turbulent Boundary Layers," Journal of Fluid Mechanics, **202**, pp. 263 – 294.

Antonia, R.A. and Luxton, R.E., 1971, "The Response of a Turbulent Boundary Layer to a Step Change in Surface Roughness. Pt. 1. Smooth to Rough," Journal of Fluid Mechanics, **48**(4), pp. 721 – 762.

Armenio, V. and Fiorotto, V., 2001, "The Importance of the Forces Acting on Particles in Turbulent Flows," Physics of Fluids, **13**(8), pp. 2437 – 2440.

Basset, A.B., 1888, "*A Treatise on Hydrodynamics*," Cambridge.

Benson, M., Tanaka, T. and Eaton, J.K., 2005, "Effects of Wall Roughness on Particle Velocities in a Turbulent Channel Flow," Transactions of the ASME, **127**, pp. 250 – 256.

Berkooz, G., Holmes, P. and Lumley, J.L., 1993, "The Proper Orthogonal Decomposition in the Analysis of Turbulent Flows," Annual Review of Fluid Mechanics, **25**, pp. 539 – 575.

Best, J., Bennet, S., Bridge, J. and Leeder, M., 1997, "Turbulence Modulation and Particle Velocities over Flat Sand Beds at Low Transport Rates," Journal of Hydraulic Engineering, **123**(12), pp. 1118 – 1129.

Blackwelder, R.F. and Eckelmann, H., 1979, "Streamwise Vortices Associated with the Bursting Phenomenon," Journal of Fluid Mechanics, **94**, pp. 577 – 594.

Blackwelder, R.F. and Kaplan, R.E., 1976, "On the Wall Structure of the Turbulent Boundary Layer," Journal of Fluid Mechanics, **76**, pp. 89 – 112.

Bogard, D.G. and Tiederman, W.G., 1986, "Burst Detection with Single-Point Velocity Measurements," Journal of Fluid Mechanics, **162**, pp. 389 – 413.

Borowsky, J.F. and Wei, T., 2011, "Two-Phase Interactions through Turbulent Events as Described by Fluid-Particle Correlations," Chemical Engineering Science, **66**, pp. 128 – 134.

Boyer, C., Duquenne, A.-M., and Wild, G., 2002, "Measuring Techniques in Gas-Liquid and Gas-Liquid-Solid Reactors," Chemical Engineering Science, **57**, pp. 3185 – 3215.

Bradshaw, P., 1971, "*An Introduction to Turbulence and its Measurement*," Pergamon Press, Oxford.

Bradshaw, P. and Pontikos, N.S., 1985, "Measurements in the Turbulent Boundary Layer on an Infinite Swept Wing," Journal of Fluid Mechanics, **159**, pp. 105 – 130.

Brandt, L. and de Lange, H. C., 2008, "Streak Interactions and Breakdown in Boundary Layer Flows," Physics of Fluids, **20**, 024107.

Breuer, M., Alletto, M., and Langfeldt, F., 2012, "Sandgrain Roughness Model for Rough Walls within Eulerian-Lagrangian Predictions of Turbulent Flows," International Journal of Multiphase Flows, **43**, pp. 157 – 175.

Brooke, J.W., Kontomaris, K., Hanratty, T.J., and McLaughlin, J.B., 1992, "Turbulent Deposition and Trapping of Aerosols at a Wall," Physics of Fluids A, **4**, 825 – 834.

Brown, G.L. and Thomas, A.S.W., 1977, "Large Structure in a Turbulent Boundary Layer," Physics of Fluids, **20**(10), pp. S243 – S252.

Brundrett, E. and Baines, W.D., "The Production and Diffusion of Vorticity in Duct Flow," Journal of Fluid Mechanics, **19**, pp. 375 – 394.

Cantwell, B.J., 1981, "Organized Motion in Turbulent Flow," Annual Review of Fluid Mechanics, **13**, pp. 457 – 515.

Cardwell, N.D., Vlachos, P.P., and Thole, K.A., 2011, "A Multi-Parametric Particle-Pairing Algorithm for Particle Tracking in Single and Multiphase Flows," Measurement Science and Technology, **22**, pp. 1 – 17.

Chen, M.Z. and Bradshaw, P., 1988, "Studies of Burst-Detection Schemes by Use of Direct Simulation Data for Fully Turbulent Channel Flow," Imperial College Report.

Chong, M.S., Perry, A.E., and Cantwell, B.J., 1990, "A General Classification of Three-Dimensional Flow Fields," Physics of Fluids A, **2**(5), pp. 765 – 777

Christensen, K.T. and Adrian, R.J., 2001, "Statistical Evidence of Hairpin Vortex Packets in Wall Turbulence," Journal of Fluid Mechanics, **431**, pp. 433 – 443.

Cleaver, J.W. and Yates, B., 1975, "A Sub Layer Model for the Deposition of Particles from a Turbulent Flow," Chemical Engineering Sciences, **30**, pp. 983 – 992.

Clift, R., Grace, J.R. and Webber, M.E., 1978, "*Bubbles, Drops, and Particles*," Academic Press, New York.

Coleman, G.N., Kim, J., and Le, A.-T., 1996, "A Numerical Study of Three-Dimensional Wall-Bounded Flows," International Journal of Heat and Fluid Flow, **17**, pp. 333 – 342.

Coleman, H.W. and Steele, W.G., 1995, "Engineering Applications of Experimental Uncertainty Analysis," AIAA Journal, **33**(10), pp. 1888 – 1896.

Comte-Bellot, 1965, "Ecoulement Turbulent entre deux Parois Paralleles," Publications Scientifiques et Techniques du Ministere de l'Air No. 419.

Corino, E.R. and Brodkey, R.S., 1969, "A Visual Investigation of the Wall Region in Turbulent Flow," Journal of Fluid Mechanics, **37**, pp. 1 – 30.

Crowe, C.T., Troutt, T.R., and Chung, J.N., 1996, "Numerical Models for Two-Phase Turbulent Flows," Annual Review of Fluid Mechanics, **28**, pp. 11– 43.

Daubechies, I., 1988, "Orthonormal Bases of Compactly Supported Wavelets," Communications in Pure and Applied Mathematics, **41**(7), pp. 909 – 996.

Dean, R.B., 1978, "Reynolds Number Dependence of Skin Friction and other Bulk Flow Variables in Two-Dimensional Rectangular Duct Flow," Transactions of the ASME I, Journal of Fluids Engineering, **100**, pp. 215 – 223.

Deen, N.G., Willems, P., van Sint Annaland, M., Kuipers, J.A.M, Lammertink, R.G.H, Kemperman, A.J.B., Wessling, M., and van der Meer W.G.J., 2010. "On Image Pre-Processing for PIV of Single- and Two-Phase Flows over Reflecting Objects," Experiments in Fluids,

del Álamo, J.C., Jiménez, J., Zandonade, P., and Moser, R. D., 2006, "Self-Similar Vortex Clusters in the Logarithmic Region," Journal of Fluid Mechanics, **561**, pp. 329 – 358.

Dritselis, C.D., 2009, "LES of Particle-Laden Turbulent Channel Flow with Transverse Roughness Elements on One Wall," Numerical Analysis and Applied Mathematics, **2**, pp. 677 – 680.

Dritselis, C.D. and Vlachos, N.S., 2011, "Numerical Investigation of Momentum Exchange between Particles and Coherent Structures in Low Re Turbulent Channel Flow," Physics of Fluids, **23**, 025103.

Druault, P. and Chaillou, C., 2007, "Use of Proper Orthogonal Decomposition for Reconstructing the 3D In-Cylinder Mean-Flow Field from PIV Data," C.R. Mecanique, **335**, pp. 42 – 47.

Durst, F., Fischer, M., Jovanovic, J., and Kikura, H., 1998, "Methods to Set Up and Investigate Low Reynolds Number, Fully Developed Turbulent Plane Channel Flows," Journal of Fluids Engineering., **120**(3), pp. 496 – 503.

Elghobashi, S. and Truesdell, G.C., 1992, "Direct Simulation of Particle Dispersion in a Decaying Isotropic Turbulence," Journal of Fluid Mechanics, **242**, pp. 655 – 700.

Elghobashi, S., 1994, "On Predicting Particle-Laden Turbulent Flows," Applied Scientific Research, **52**, pp. 309 – 329.

El-Shobokshy, M.S., 1983, "Experimental Measurements of Aerosol Deposition to Smooth and Rough Surfaces," Atmospheric Environment, **17**, pp. 639 – 644.

Falco, R.E., 1977, "Coherent Motions in the Outer Region of Turbulent Boundary Layers," Physics of Fluids, **20**, pp. 124 – 132.

Farge, M., 1992, "Wavelet Transforms and their Applications to Turbulence," Annual Review of Fluid Mechanics, **24**, pp. 395 – 457.

Favre, A., 1965, "Equations des Gaz Turbulents Compressibles: Formes Generales," Journal of Mechanics, **4**, pp. 361 – 390.

Ferry, J. and Balachandar, S., 2001, "A Fast Eulerian Method for Disperse Two-Phase Flow," International Journal of Multiphase Flow, **27**, pp. 1199 – 1226.

Fessler, J.R. and Eaton, J.K., 1999, "Turbulence Modification by Particles in a Backward-Facing Step Flow," Journal of Fluid Mechanics, **394**, pp. 97 – 117.

Fessler, J.R., Kulick, J.D., and Eaton, J.K., 1994, "Preferential Concentration of Heavy Particles in a Turbulent Channel Flow," Physics of Fluids, **6**(11), pp. 3742 – 3749.

Forliti, D.J., Strykowski, P.J. and Debatin, K., 2000, "Bias and Precision Errors of Digital Particle Image Velocimetry," Experiments in Fluids, **28**, pp. 436 – 447.

Fujita, H., Yokosawa, H., and Hirota, M., 1989, "Secondary Flow to the Second Kind in Rectangular Ducts with One Rough Wall," Experimental Thermal and Fluid Science, **2**, pp. 72 – 80.

Gessner, F.B., 1973, "The Origin of Secondary Flow in Turbulent Flow along a Corner," Journal of Fluid Mechanics, **58**(1), pp. 1 – 25.

Gore, R.A. and Crowe, C.T., 1989, "Effect of Particle Size on Modulating Turbulence Intensity," International Journal of Multiphase Flow, **15**, pp. 279 – 285.

Grass, A.J., 1971, "Structural Features of Turbulent Flow over Smooth and Rough Boundaries," Journal of Fluid Mechanics, **50**, 233 – 255.

Hagiwara, Y., Murata, T., Tanaka, M., and Fukawa, T., 2002, "Turbulence Modification by the Clusters of Settling Particles in Turbulent Water Flow in a Horizontal Duct," Powder Technology, **125**, pp. 158 – 167.

Head, M.R. and Bandyopadhyay, P., 1981, "New Aspects of Turbulent Boundary Layer Structure," Journal of Fluid Mechanics, **107**, pp. 297 – 338.

Herring, H.J. and Norbury, J.F., 1967, "Some Experiments on Equilibrium Boundary Layers in Favourable Pressure Gradients," Journal of Fluid Mechanics, **27**, pp. 541 – 549.

Hetsroni, G., 1989, "Particle-Turbulence Interaction," International Journal of Multiphase Flow, **15**, pp. 735 – 746.

Hinze, J.O., 1972, "Turbulent Fluid and Particle Interaction," In: Proceedings of the International Symposium on Two-Phase Systems, Edited by Hetsroni, G., Sideman, S., and Hartnett, J.P., pp. 433 – 453.

Hong, J., Katz, J., and Schultz, M.P., 2011, "Near-Wall Turbulence Statistics and Flow Structures over Three-Dimensional Roughness in Turbulent Channel Flow," Journal of Fluid Mechanics, **667**, pp. 1 – 37.

Hussain, A.K.M.F., 1983, "Coherent Structures - Reality and Myth," Physics of Fluids, **26**(10), pp. 2816 – 2850.

Hutchins, N., Hambleton, W.T. and Marusic, I., 2005, "Inclined Cross-Stream Stereo Particle Image Velocimetry Measurements in Turbulent Boundary Layers," Journal of Fluid Mechanics, **541**, pp. 21 – 54.

Jeong, J., Hussain, F. Schoppa, W., and Kim, J., 1997, "Coherent Structures near the Wall in a Turbulent Channel Flow," Journal of Fluid Mechanics, **332**, pp. 185 – 214.

Jiménez, J., 1998, "The Largest Scales of Turbulence," In: CTR Annual Research Briefs, edited by Moin, P., pp. 137 – 154.

Jiménez, J., 2004, "Turbulent Flows over Rough Walls," Annual Review of Fluid Mechanics, **36**, pp. 173 – 196.

Johansson, A.V. and Alfredsson, P.H., 1982, "On the Structure of Turbulent Channel Flow," Journal of Fluid Mechanics, **122**, pp. 295 – 314.

Johansson, A.V., Alfredsson, P.H., and Kim, J., 1991, "Evolution and Dynamics of Shear-layer Structures in Near-Wall Turbulence," Journal of Fluid Mechanics, **224**, pp. 579 – 599.

Kaftori, D., Hetsroni, G., and Banerjee, S., 1995a, "Particle Behaviour in the Turbulent Boundary Layer. I. Motion, Deposition, and Entrainment," Physics of Fluids, **7**(5), pp. 1095 – 1106.

Kaftori, D., Hetsroni, G., and Banerjee, S., 1995b, "Particle Behaviour in the Turbulent Boundary Layer. II. Velocity and Distribution Profiles," Physics of Fluids, **7**(5), pp. 1107 – 1121.

Kaftori, D., Hetsroni, G., and Banerjee, S., 1998, "Effects of Particles on Wall Turbulence," International Journal of Multiphase Flow, **24**(3), pp. 359 – 386.

Kenning, V.M. and Crowe, C.T., 1997, "On the Effect of Particles on Carrier Phase Turbulence in Gas-Particle Flows," International Journal of Multiphase Flow, **23**, pp. 403 – 408.

Khalitov, D.A. and Longmire, E.K., 2002, "Simultaneous Two-Phase PIV by Two-Parameter Phase Discrimination," Experiments in Fluids, **32**, pp. 252 – 268.

Kidanemariam, A.G., Chan-Braun, C., Doychev, C., and Uhlmann, M., 2013, "Direct Numerical Simulation of Horizontal Open Channel Flow with Finite Size, Heavy Particles at Low Solid Volume Fraction," New Journal of Physics, **15**, 025031.

Kiesow, R.O. and Plesniak, M., 2003, "Near-Wall Physics of a Shear-Driven Three-Dimensional Turbulent Boundary Layer with Varying Crossflow," Journal of Fluid Mechanics, **484**, pp. 1 – 39.

Kiger, K.T. and Pan, C., 2002, "Suspension and Turbulence Modification Effects of Solid Particulates on a Horizontal Turbulent Channel Flow," Journal of Turbulence, **3**, pp. 1 – 21.

Kim, K.C., 1987, "Evolution of a Vortical Structure Associated with the Bursting Event in a Channel Flow," In: Turbulent Shear Flows **5**, Springer-Verlag, New York, pp. 221 – 227.

Kim, K.C. and Adrian, R.J., 1999, "Very Large-Scale Motion in the Outer Layer," Physics of Fluids, **11**(2), pp. 417 – 422.

Klebanoff, P.S., 1954, "Characteristics of Turbulence in a Boundary Layer with Zero Pressure Gradient," NACA Technical Note, No. 3178.

Klewicki, J.C., 1997, "Self-sustaining Traits of Near-Wall Motions Underlying Boundary Layer Stress Transport," In: Self-sustaining Mechanisms of Wall Turbulence (ed. R. L. Panton), **15**, pp. 135 – 166.

Klewicki, J.C. and Hirschi, C.R., 2004, "Flow Field Properties Local to Near-Wall Shear Layers in a Low Reynolds Number Turbulent Boundary Layer," Physics of Fluids **16**, pp. 4163 – 4176.

Kline, S.J., Reynolds, W.C., Schraub, F.A., and Runstadler, P.W., 1967, "The Structure of Turbulent Boundary Layers," Journal of Fluid Mechanics, **30**, pp. 741 – 773.

Kostas, J., Soria, J, and Chong, M.S., 2005, "A Comparison between Snapshot POD Analysis of PIV Velocity and Vorticity Data," Experiments in Fluids, **38**, pp. 146 - 160.

Krogstad, P.-Å., Andersson, H.I., Bakken, O.M., and Ashrafian, A., 2005, "An Experimental and Numerical Study of Channel Flow with Rough Walls," Journal of Fluid Mechanics, **530**, pp. 327 – 352.

Krogstad, P.-Å., Antonia, R.A. and Browne, L.W.B., 1992, "Comparison between Rough-and Smooth-Wall Turbulent Boundary Layers," Journal of Fluid Mechanics, **245**, pp. 599 – 617.

Kulick, J.D., Fessler, J.R., and Eaton, J.K., 1994, "Particle Response and Turbulence Modification in Fully Developed Channel Flow," Journal of Fluid Mechanics, **277**, pp.

109 – 134.

Kussin, J. and Sommerfeld, M., 2002, "Experimental Studies on Particle Behaviour and Turbulence Modification in Horizontal Channel Flow with Different Wall Roughness," Experiments in Fluids, **33**, pp. 143 – 159.

Lai, A.C.K., Byrne, M. and Goddard, A.J.H., 2001, "Aerosol Deposition in Turbulent Channel Flow on a Regular Array of Three-Dimensional Roughness Elements," Aerosol Science, **32**, pp. 121 – 137.

Laín, S. and Sommerfeld, M., 2008, "Euler/Lagrange Computations of Pneumatic Conveying in a Horizontal Channel with Different Wall Roughness," Powder Technology, 184, pp. 76 – 88.

Le, A.-T., Coleman, G.N., and Kim, J., 1999, "Near-Wall Turbulence Structures in Three-Dimensional Boundary Layers," Proceedings of the First International Symposium on Turbulence and Shear Flow Phenomenon, Santa Barbara, CA, U.S.A., pp. 151 – 156.

Lecuona, A., Sosa, P.A., Rodriguez, P.A., and Zequeira, R.I., 2000, "Volumetric Characterization of Dispersed Two-Phase Flows by Digital Image Analysis," Measurement Science and Technology, **11**, pp. 1152 – 1161.

Lee, C., Wu, C.H., and Hoopes, J.A., 2009, "Simultaneous Particle Size and Concentration Measurements Using a Back-Lighted Particle Imaging System," Flow Measurement and Instrumentation, **20**, pp. 189 – 199.

Li, A. and Ahmadi, G., 1993, "Computer Simulation of Deposition of Aerosols in a Turbulent Channel Flow with Rough Walls," Aerosol Science and Technology, **18**, pp. 11 – 24.

Liu, Z., Landreth, C., Adrian, R., and Hanratty, T., 1991, "High Resolution Measurement of Turbulent Structure in a Channel with Particle Image Velocimetry," Experiments in Fluids, **10**, pp. 301 – 312.

Lu, S. S. and Willmarth, W. W., 1973, "Measurements of the Structure of the Reynolds Stress in a Turbulent Boundary Layer," Journal of Fluid Mechanics, **60**, pp. 481 – 512.

Lumley, J.L., 1967, "The Structure of Inhomogeneous Turbulence," In: Atmospheric Turbulence and Wave Propagation, ed. Yaglom, A.M., Tatarski, V.I., pp. 166 – 178.

Mallat, S., 1989, "A Theory for Multi-Resolution Signal Decomposition: The Wavelet Representation," IEEE Transactions on Pattern Analysis and Machine Intelligence, **11** (7), pp. 674 – 693.

Marchioli, C. and Soldati, A., 2007, "Reynolds Number Scaling of Particle Preferential Concentration in Turbulent Channel Flow," In: Advances in Turbulence XI, Springer

Proceedings in Physics, **117**, pp. 298 – 300.

Maxey, M.R. and Riley, J.J., 1983, "Equation of Motion for a Small Rigid Sphere in a Non-uniform Flow," Physics of Fluids, **26**(4), pp. 883 – 889.

Millikan, C.B., 1938, "A Critical Discussion of Turbulent Flows in Channels and Circular Tubes," Proceedings of the Fifth International Congress on Applied Mechanics, Editors: Den Hartog, J.P. and Peters, H., Wiley, New York.

Mito, Y. and Hanratty, T.J., 2005, "A Stochastic Description of Wall Sources in a Turbulent Field. Part 3: Effect of Gravitational Settling on the Concentration Profiles," International Journal of Multiphase Flow, **31**, pp. 155 – 178.

Moin, P., Shih, T.-H., Driver, D. and Mansour, M.N., 1990, "Direct Numerical Simulation of a Three-Dimensional Turbulent Boundary Layer," Physics of Fluids A, **2**, pp. 1846 – 1853.

Morrison, J.F., Tsai, H.M., and Bradshaw, P., 1989, "Conditional-Sampling Schemes for Turbulent Flow, Based on the Variable-Interval Time Averaging (VITA) Algorithm," Experiments in Fluids, **7**, pp. 173 – 189.

Muste, M., Yu, K., Fujita, I., and Ettema, R., 2009, "Two-Phase Flow Insights into Open-Channel Flows with Suspended Particles of Different Densities," Environmental Fluid Mechanics, **9**, pp. 161 – 186.

Na, Y., Hanratty, T.J., and Liu, Z.-C., 2001, "The Use of DNS to Define Stress Producing Events for Turbulent Flow over a Smooth Wall," Flow, Turbulence and Combustion, **66**, pp. 495 – 512.

Nakagawa, S. and Hanratty, T.J., 2001, "Particle Image Velocimetry Measurements of Flow over a Wavy Wall," Physics of Fluids, **13**(11), pp. 3504 – 3507.

Nikuradse, J., 1933, "Laws of Flow in Rough Pipes," NACA TM 1292.

Nino, Y. and Garcia, M.H., 1996, "Experiments on Particle-Turbulence Interactions in the Near-Wall Region of an Open Channel Flow: Implications for Sediment Transport," Journal of Fluid Mechanics, **326**, pp. 285 – 319.

Noguchi, K. and Nezu, I., 2009, "Particle-Turbulence Interaction and Local Particle Concentration in Sediment-Laden Open-Channel Flows," Journal of Hydraulic Research, **3**, pp. 54 – 68.

Ohmi, K. and Li, H.-Y., 2000, "Particle-Tracking Velocimetry with New Algorithms," Measurement Science and Technology, **11**, pp. 603 – 616.

Otsu, N., 1979, "A Threshold Selection Method from Gray-Level Histogram," IEEE Transactions on Systems, Man, and Cybernetics, **9**, pp. 62 – 66.

Pedinotti, S., Mariotti, G., and Banerjee, S., 1992, "Direct Numerical Simulation of Particle Behaviour in the Wall Region of Turbulent Flows in Horizontal Channels," International Journal of Multiphase Flow, **18**, pp. 927 – 941.

Perry, A.E. and Chong, M.S., 1982, "On the Mechanism of Wall Turbulence," Journal of Fluid Mechanics, **119**, pp. 173 – 217.

Perry, A.E. and Marušić, I., 1995, "A Wall-Wake Model for the Turbulence Structure of Boundary Layers. Part 1. Extension of the Attached Eddy Hypothesis," Journal of Fluid Mechanics, **298**, pp. 361 – 388.

Piirto, M., Ihalainen, H., Eloranta, H., and Saarenrinne, P., 2001, "2D Spectral and Turbulence Length Scale Estimation with PIV," Journal of Visualization, **4**, pp. 39 – 48.

Piomelli, U., Ferziger, J., Moin, P., and Kim, J., 1989, "New Approximate Boundary Conditions for Large Eddy Simulations of Wall Bounded Flows," Physics of Fluids A, **1**, pp. 1061 – 1068.

Pope, S.B., 2000, "*Turbulent Flows*," Cambridge University Press.

Prandtl, L., 1932, "Zur Turbulenten Strömung in Roren und langs Plätten," Ergeb Aerod Versuch Gottingen, **4**, pp.18 – 29.

Prasad, A.K., Adrian, R.J., Landreth, C.C., and Offutt, P.W., 1992, "Effect of Resolution on the Speed and Accuracy of Particle Image Velocimetry Interrogation," Experiments in Fluids, **13**, pp. 105 – 116.

Raffel, M., Willert, C.E., and Kompenhaus, J., 1998, "*Particle Image Velocimetry*: *A Practical Guide*," Springer Verlag.

Rashidi, M., Hetsroni, G., and Banerjee, S., 1990, "Particle-Turbulence Interaction in a Boundary-Layer," International Journal of Multiphase Flow, **16**, pp. 935 – 949.

Reichert, R.S., Hatay, F.F., Biringen, S., and Huser, A., 1994, "Proper Orthogonal Decomposition Applied to Turbulent Flow in a Square Duct," Physics of Fluids, **6**(9), pp. 3086 – 3092.

Righetti, M. and Romano, G.P., 2004, "Particle-Fluid Interactions in a Plane Near-Wall Turbulent Flow," Journal of Fluid Mechanics, **505**, pp. 93 – 121.

Robinson, S. K., 1991, "Coherent Motion in the Turbulent Boundary Layer," Annual Review of Fluid Mechanics, **23**, pp. 601 – 639.

Rogers, C.B. and Eaton, J.K., 1990, "The Behaviour of Solid Particles in a Vertical Turbulent Boundary Layer in Air," International Journal of Multiphase Flows, **16**, pp. 819 – 834.

Ruppert-Felsot, J., Farge, M., and Petitjeans, P., 2009, "Wavelet Tools to Study Intermittency: Application to Vortex Bursting," Journal of Fluid Mechanics, **636**, 427 – 453.

Saffar-Avval, M., Basirat Tabrizi, H., Mansoori, Z. and Ramezani, P., 2007, "Gas-Solid Turbulent Flow and Heat Transfer with Collision Effect in a Vertical Pipe," International Journal of Thermal Sciences, **46**, pp. 67 – 75.

Schlichting, H., 1979, "*Boundary-Layer Theory*," 7th Edition, McGraw-Hill, New York.

Schoppa, W. and Hussain, F., 2000, "Coherent Structure Dynamics in Near-Wall Turbulence," Fluid Dynamics Research, **26**, pp. 119 – 139.

Schoppa, W. and Hussain, F. 2002, "Coherent Structure Generation in Near-Wall Turbulence," Journal of Fluid Mechanics, **453**, pp. 57 – 108.

Sen, M., Bhaganagar, K., and Juttijudata, V., 2007, "Application of Proper Orthogonal Decomposition to Investigate a Turbulent Boundary Layer in a Channel with Rough Walls," Journal of Turbulence, **8**(41), pp. 1 – 21.

Shao, X., Wu, T., and Yu, Z., 2012, "Fully Resolved Numerical Simulation of Particle-Laden Turbulent Flow in a Horizontal Channel at a Low Reynolds Number," Journal of Fluid Mechanics, **693**, pp. 319 – 344.

Shotorban, B. and Balachandar, S., 2006, "Particle Concentration in Homogeneous Shear Turbulence Simulated via Lagrangian and Equilibrium Eulerian Approaches," Physics of Fluids, **18**, 065105.

Sirovich, L., 1987, "Turbulence and the Dynamics of Coherent Structures. Part 1: Coherent Structures," Quarterly of Applied Mathematics, **45**, pp. 561 – 571.

Sirovich, L., 1991, "Analysis of Turbulent Flows by Means of the Empirical Eigenfunctions," Fluid Dynamics Research, **8**, pp. 85 – 100.

Sommerfeld, M. and Huber, N., 1999, "Experimental Analysis and Modelling of Particle-Wall Collisions," International Journal of Multiphase Flow, **25**, pp. 1457 – 1489.

Sommerfeld, M., 1995, "The Importance of Inter-Particle Collisions in Horizontal Gas-Solid Channel Flows," In: Stock, D.E., et al. (Eds.), Gas-Particle Flows. In: ASME Fluids Engineering Conference, Hiltons Head, USA, FED-Vol. **228**, ASME, pp. 335 – 345.

Sommerfeld, M., 2003, "Analysis of Collision Effects for Turbulent Gas-Particle Flow in a Horizontal Channel: Part 1. Particle Transport," International Journal of Multiphase Flow, **29**, pp. 675 – 699.

Smith, C.R., Walker, J.D.A, Haidari, A.H. and Sobrun, U., 1991, "On the Dynamics of Near-Wall Turbulence," Philosophical Transactions of the Royal Society of London A, **336**, pp. 131 – 175.

Squires, K.D. and Eaton, J.K., 1990, "Particle Response and Turbulence Modification in Isotropic Turbulence," Physics of Fluids A, **2**(7), pp. 1191 – 1203.

Stanislas, M., Perret, L., and Foucaut, J.-M., 2008, "Vortical Structures in the Turbulent Boundary Layer: A Possible Route to a Universal Representation," Journal of Fluid Mechanics, **602**, pp. 327 – 382.

Stern, F., Muste, M., Beninati, M.-L., and Eichinger, W.E., 1999, "Summary of Experimental Uncertainty Assessment Methodology with Example," IIHR Technical Report No. 406, Iowa Institute if Hydraulic Research, College of Engineering, The University of Iowa.

Stokes, G.G., 1851, "On the Effect of Internal Friction of Fluids on the Motion of a Pendulum," Transactions of the Cambridge Philosophical Society, **8**, pp. 8 – 16.

Sumer, B.M. and Deigaard, R., 1981, "Particle Motions near the Bottom in Turbulent Flow in an Open Channel. Part 2," Journal of Fluid Mechanics, **109**, pp. 311 – 337.

Tachie, M.F., Bergstrom, D.J., and Balachandar, R., 2000, "Rough-Wall Turbulent Boundary Layers in Shallow Open Channel Flow," Journal of Fluids Engineering, **122**, pp. 533 – 541.

Tanaka, T. and Tsuji, Y., 1991, "Numerical Simulation of Gas-Solid Two-Phase Flow in a Vertical Pipe: On the Effect of Inter-Particle Collision," In: Gas-Solid Flows, FED ASME, **121**, pp. 123 – 128.

Tay, G.F.K., 2009, "Rough-Wall Turbulent Flows in Adverse and Favourable Pressure Gradients," M.Sc. Thesis, University of Manitoba, Winnipeg.

Tay, G.F.K., Kuhn, D.C.S., and Tachie, M.F., 2015, "Effects of Sedimenting Particles on the Turbulence Structure in a Horizontal Channel Flow," Physics of Fluids, **27**, 025106.

Tay, G.F.K., Kuhn, D.C.S., and Tachie, M.F., 2013, "Surface Roughness Effects on the Turbulence Statistics in a Low Reynolds Number Channel," Journal of Turbulence, **14** (1), pp. 121 – 146.

Tchen, C.M., 1947, "Mean Value and Correlation Problems Connected with the Motion of Small Particles Suspended in a Turbulent Fluid," Ph.D. Thesis, Delft, Martinus, Nijhoff, The Hague.

Theodorsen, T., 1952, "Mechanism of Turbulence," In: Proceedings of the Second Midwestern Conference of Fluid Mechanics, Ohio State University, pp. 1 – 18.

Torobin, L.B. and Gauvin, W.H., 1959, "Fundamental Aspects of Solids-Gas Flow," Canadian Journal of Chemical Engineering, **37**, pp. 129 – 141.

Toth, B., Anthoine, J., and Riethmuller, M.L., 2009, "Two-Phase PIV Method Using Two Excitation and Two Emission Spectra," Experiments in Fluids, **47**, pp. 475 – 487.

Towers, D.P., Towers, C.E., Buckberry, C.H., and Reeves, M., 1999, "A Colour PIV System Employing Fluorescent Particles for Two-Phase Flow Measurements," Measurement Science and Technology, **10**, pp. 824 – 830.

Townsend, A.A., 1976, "*The Structure of Turbulent Shear Flow*," Second Edition, Cambridge University Press.

Tsuji, Y. and Morikawa, Y., 1982, "LDV Measurements of an Air-Solid Two-Phase Flow in a Horizontal Pipe," Journal of Fluid Mechanics, **120**, pp. 385 – 409.

Tsuji, Y., Morikawa, Y., Tanaka, T., Nakatsukasa, N. and Nakatani, M., 1987, "Numerical Simulation of Gas-Solid Two-Phase Flow in a Two-Dimensional Horizontal Channel," International Journal of Multiphase Flow, **13**, pp. 671 – 684.

van Hout, R., 2011, "Time-Resolved PIV Measurements of the Interaction of Polystyrene Beads with Near-Wall-Coherent Structures in a Turbulent Channel Flow," International Journal of Multiphase Flow, **37**, pp. 346 – 357.

Volino, R. J., Schultz, M. P. and Flack, K. A., 2007, "Turbulence Structure in Rough- and Smooth-Wall Boundary Layers," Journal of Fluid Mechanics, **592**, pp. 263 – 293.

Volino, R. J., Schultz, M. P., and Flack, K. A., 2009, "Turbulence Structure in a Boundary Layer with Two-Dimensional Roughness," Journal of Fluid Mechanics, **635**, pp. 75 – 101.

Vreman, A.W., 2007, "Turbulence Characteristics of Particle-Laden Pipe Flow," Journal of Fluid Mechanics, **584**, pp. 235 – 279.

Wallace, J.M., Eckelmann, H. and Brodkey, R.S., 1972, "The Wall Region in Turbulent Flow," Journal of Fluid Mechanics, **54**, pp. 39 – 48.

Westerweel, J., 1997, "Fundamentals of Digital Particle Image Velocimetry," Measurement Science and Technology, **8**, pp. 1379 – 1392.

Wu, Y., Wang, H., Liu, Z., and Li, J., 2006, "Experimental Investigation on Turbulence Modification in a Horizontal Channel Flow at Relatively Low Mass Loading," Acta Mechanica Sinica, **22**, pp. 99 – 108.

Wu, Y. and Christensen, K. T., 2006, "Population Trends of Spanwise Vortices in Wall Turbulence," Journal of Fluid Mechanics, **568**, pp. 55 – 76.

Wu, Y. and Christensen, K.T., 2010, "Spatial Structure of a Turbulent Boundary Layer with Irregular Surface Roughness," Journal of Fluid Mechanics, **655**, pp. 380 – 418.

Yamamoto, Y. and Okawa, T., 2010, "Numerical Study of Particle Concentration Effect on Deposition Characteristics in Turbulent Pipe Flows," Journal of Nuclear Science and Technology, **47**(10), pp. 945 – 952.

Yamamoto, Y., Potthoff, M., Tanaka, T., Kajishima, T. and Tsuji, Y., 2001, "Large Eddy Simulation of Turbulent Gas-Particle Flow in a Vertical Channel: Effect of Considering Inter-Particle Collisions," Journal of Fluid Mechanics, **442**, pp. 303 – 334.

Yang, T.S. and Shy, S.S., 2005, "Two-Way Interaction between Solid Particles and Homogeneous Air Turbulence: Particle Settling Rate and Turbulence Modification Measurements," Journal of Fluid Mechanics, **526**, pp. 171 – 216.

Yuan, Z. and Michaelides, E.E., 1992, "Turbulence Modulation in Particulate Flows," International Journal of Multiphase Flow, **18**, pp. 779 – 785.

Zhang, J. and Hu, J., 2008, "Image Segmentation Based on 2D Otsu Method with Histogram Analysis," International Conference on Computer Science and Software Engineering, pp. 105 – 108.

Zhou, J., Adrian, R.J., Balachandar, S., and Kendall, T.M., 1999, "Mechanisms for Generating Coherent Packets of Hairpin Vortices in Channel Flow," Journal of Fluid Mechanics, **387**, pp. 353 – 396.